2021

# Seismic performance evaluation of reinforced concrete bridge piers considering postearthquake capacity degradation

Todorov, Borislav

# SEISMIC PERFORMANCE EVALUATION OF REINFORCED CONCRETE BRIDGE PIERS CONSIDERING POST-EARTHQUAKE CAPACITY DEGRADATION

by

**Borislav Todorov**

A thesis
submitted to the Faculty of Graduate Studies
in partial fulfilment of the requirements for the
Degree of Master of Science
in

Civil Engineering

Supervisor

**Dr. Muntasir Billah**

Assistant Professor – Dept. of Civil Engineering

Lakehead University
Thunder Bay, Ontario
May 2021

## Author's Declaration Page

I hereby declare that I am the sole author of this thesis. This is a true copy of the thesis, including any required final revisions, as accepted by my examiners. I understand that my thesis may be made electronically available to the public.

# Abstract

Bridges play a key role in the transportation sector while serving as lifelines for the economy and safety of communities. The need for resilient bridges is especially important following natural disasters, where they serve as evacuation, aid, and supply routes to an affected area. Much of the earthquake engineering community is interested in improving the resiliency of bridges, and many contributions to the field have been made in the past decades, where a shift towards performance-based design (PBD) practices is underway. While the Canadian Highway Bridge Design Code (CHBDC) has implemented PBD as a requirement for the seismic design of lifeline and major route bridges, the nature of PBD techniques translate to a design process that is not universally compatible for all scenarios and hazards. Therefore, there is great benefit to be realised in the development of PBD guidelines for mainshock-aftershock seismic sequences for scenarios in which the chance to assess and repair a bridge is not possible following a recent mainshock. This research analytically explored a parameterized set of 20 reinforced concrete bridge piers which share several geometrical and material properties with typical bridge bents that support many Canadian bridges. Of those piers, half are designed using current PBD guidelines provided in the 2019 edition of the CHBDC, whereas the remaining half are designed with insufficient transverse reinforcement commonly found in the bridges designed pre-2000. To support this study, a nonlinear fiber-based modelling approach with a proposed material strength degradation scheme is developed using the OpenSEES finite element analysis software. A multiple conditional mean spectra (CMS) approach is used to select a suite of 50 mainshock-aftershock ground motion records for the selected site in Vancouver, British Columbia, which consist of crustal, inslab, and interface earthquakes that commonly occur in areas near the Cascadia Subduction zone. Nonlinear time history analysis is performed for mainshock-only and mainshock-aftershock excitations, and static pushover analysis is also performed in lateral and axial directions for the intact columns, as well as in their respective post-MS and post-AS damaged states. Using the resulting data, a framework for post-earthquake seismic capacity estimation of the bridge piers is developed using machine learning regression methods, where several candidate models are tuned using an exhaustive grid search algorithm approach and k-fold crossvalidation. The tuned models are fitted and evaluated against a test set of data to determine a single best performing model using a multiple scorer performance index as the metric. The resulting performance index suggests that the decision tree model is the most suitable regressor for capacity estimation due to this model exhibiting the

highest accuracy as well as lowest residual error. Moreover, this study also assessed the fragility of the bridge piers subjected to mainshock-only and mainshock-aftershock earthquakes. Probabilistic seismic demand models (PSDMs) are derived for the columns designed using current PBD guidelines (PBD-compliant) to evaluate whether the current PBD criteria is sufficient for resisting aftershock effects. Additional PSDMs are generated for the columns with inadequate transverse reinforcement (PBD-deficient) to assess aftershock vulnerability of older bridges. The developed fragility curves indicate an increased fragility of all bridge piers for all damage levels. The findings indicate that adequate aftershock performance is achieved for bridge piers designed to current (2019) CHBDC extensive damage level criteria. Furthermore, it is suggested that minimal damage performance criteria need to be developed for aftershock effects, and the repairable damage level be reintroduced for major route bridges.

# Acknowledgements

I extend my deepest gratitude and appreciation to my graduate supervisor Dr. Muntasir Billah, for without his continued support and belief in me, this project would not have come to fruition. Dr. Billah's mentorship has been exemplary and his professionalism, expertise, and patience are first class; he has helped immensely in shaping my career and inspires me to hold myself to the highest of standards. Dr. Billah is always quick to offer his support, knowledge, and development opportunities, and knows how to push me within my abilities to achieve my goals which has enriched my graduate experience.

I would like to thank my thesis examiners, Dr. Ahmed Elshaer and Dr. Jamie Padgett for their valuable insight and suggestions, your input helped improve this research and is much appreciated.

My thanks go out to the OpenSees community, and specifically Dr. Shuai Li, Dr. Michael Scott, and Dr. Mostafa Badroddin who have provided me with much needed answers and ideas during the development of my models. Thank you to Hanlin Dong for his SmartAnalyze script, it proved to be very useful when I was facing problems with model convergence. Additional special thanks go out to Vahid Aghaei doost, for taking time out of your day for the several meetings with me to discuss and debug our Opensees model, I really appreciate your unique and thorough approach to modeling which you brought to the table.

To the friends made during my undergraduate and graduate studies at Lakehead University as well as my roommates, especially Kyle, Kariem, Zayan, Leah, and Ellen, I am appreciative and thankful for our friendships, the meals we shared, and the conversations we've had. You have brightened my days, and have helped make the long Thunder Bay winters a little warmer.

Lastly, I am extremely thankful for my best friend and younger brother, Leo for his encouragement and support for me throughout this journey.

# Table of Contents

# List of Tables

# List of Figures

# Nomenclature

### Symbols

| | |
|---|---|
| $A_s$ | Gross steel cross-sectional area (mm$^2$) |
| $f_l'$ | Effective lateral pressure in circular columns |
| $A_g$ | Gross cross-sectional area (mm$^2$) |
| $A_{ps}$ | Gross prestressing steel cross-sectional area (mm$^2$) |
| $E_c$ | Elastic modulus of concrete (MPa) |
| $E_s$ | Elastic modulus of steel (MPa or GPa) |
| $L_p$ | Plastic hinge length of reinforced concrete columns (mm) |
| $P/f_c'A_g$ | Axial load ratio (%) |
| $P_f$ | Axial Load (kN) |
| $S_a$ | Spectral acceleration (g) |
| $S_d$ | Spectral displacement (mm) |
| $d_b$ | Longitudinal bar diameter (mm) |
| $f_c'$ | Concrete compressive strength (MPa) |
| $f_{c0}'$ | Concrete cylinder compressive strength (MPa) |
| $f_l$ | Pressure by the transverse reinforcement which confines the core concrete |
| $f_{pu}$ | Yield strength of prestressing steel (MPa) |
| $f_t$ | Concrete tensile strength (MPa) |
| $f_y$ | Yield strength of steel (MPa) |
| $f_{yh}$ | Yield strain of transverse steel (MPa) |
| $k_e$ | Confinement effectiveness coefficient |
| $x_n$ | Nondimensional parameter for beginning of compression straight line descent |
| $x_p$ | Nondimensional parameter for beginning of tension straight line descent |
| $\Phi_c$ | Concrete resistance factor |
| $\varepsilon_{bb}$ | Tensile strain corresponding to bar buckling |
| $\varepsilon_c$ | Material strain of concrete |
| $\varepsilon_{cu}$ | Ultimate compressive strain of concrete |
| $\varepsilon_s$ | Material strain of longitudinal steel reinforcement |

| | |
|---|---|
| $\varepsilon_{su}$ | Ultimate tensile strain of steel |
| $\varepsilon_t$ | Concrete strain at maximum tensile strength |
| $\rho_s$ | Volumetric transverse steel reinforcement ratio (%) |
| $L$ | Length of RC column (mm) |
| $T$ | Fundamental period (sec.) |
| $k$ | Stiffness (N/mm) |
| $m$ | Mass (tons) |
| $r$ | Nondimensional straight line descent parameter |

**Abbreviations**

| | |
|---|---|
| AdaBoost | Adaptive boosting |
| AI | *In the context of seismic engineering*: Arias intensity |
| AI | *In the context of machine learning*: Artificial intelligence |
| ANN | Artificial neural network |
| APSHA | Aftershock probabilistic seismic hazard analysis |
| AS | Aftershock |
| ATC | Applied technology council |
| BCE | Beam-column element |
| BWH | beamWithHinges |
| CART | Classification and regression trees |
| CatBoost | Categorical boosting |
| CAV | Cumulative absolute velocity |
| CFRP | Carbon fiber reinforced polymer |
| CHBDC | Canadian highway bridge design code |
| CMS | Conditional mean spectra |
| CSA | Canadian standards association |
| DI | Damage index |
| DS | Damage state |
| DT | Decision trees |
| EDP | Engineering demand parameter |
| FRP | Fibre reinforced polymer |

| | |
|---|---|
| GSA | Grid search algorithm |
| IDA | Incremental dynamic analysis |
| IM | Intensity measure |
| KNN | K-nearest neighbours |
| LightGBM | Light gradient boosting |
| LR | Linear regression |
| LS | Limit state |
| LSTM | Long short-term memory |
| MARS | Multivariate adaptive regression splines |
| MD | Maximum drift |
| MDOF | Multiple degrees of freedom |
| ML | Machine learning |
| MLP | Multi-layer perceptron |
| MS | Mainshock |
| MS-AS | Mainshock-aftershock |
| MS-SM | Spectrally matched mainshock back-to-back record |
| $M_w$ | Moment magnitude |
| NLTHA | Nonlinear time history analysis |
| PA-DI | Park and Ang damage index |
| PBD | Performance-based design |
| PBEE | Performance based earthquake engineering |
| PBPD | Performance-based plastic design |
| PBSD | Performance-based seismic design |
| PGA | Peak ground acceleration |
| PGV | Peak ground velocity |
| PH | Plastic hinge |
| PRSM | Polynomial response surface models |
| PSDM | Probabilistic seismic demand model |
| PSHA | Probabilistic seismic hazard analysis |
| RBF | Radial basis function |
| RBFN | Radial basis function networks |

| | |
|---|---|
| RC | Reinforced concrete |
| ReLU | Rectified linear unit |
| RF | Random forests |
| RMSE | Root mean squared error |
| RR | Ridge regression |
| RSS | Residual sum of squares |
| SDOF | Single degree of freedom |
| SMA | Shape memory alloy |
| SMAPE | Symmetrical mean absolute percentage error |
| SMRF | Steel moment resisting frame |
| SPO | Static pushover |
| SVMR | Support vector machines for regression |
| tanh | Hyperbolic tangent |
| UHS | Uniform hazard spectrum |
| XGBoost | Extreme gradient boosting |

# Chapter 1    Introduction

## 1.1    Background

Bridges are an essential component to transportation infrastructure in many communities throughout the world which fundamentally serve multiple industries. While the uninterrupted service bridges provide is often overlooked, their importance during earthquake events where the safety of the public is threatened and the mobility of emergency responders and potential evacuation routes can become bottlenecked is paramount. Much of the earthquake engineering community is interested in improving the resiliency of bridges, and many contributions to the field have been made in the past few decades, where a shift towards performance-based design (PBD) practices is underway. In Canada, the 2014 edition of the Canadian highway bridge design code (CHBDC) (National Research Council of Canada 2014) adopted PBD for seismic design of lifeline and major route bridges where some performance levels and performance criteria have been defined.

## 1.2    Problem Statement

The sophistication of performance based seismic design (PBSD) continues to improve and holds an expanding stake in maximizing service life of bridges in the engineering community. Recent advances in PBSD focus on improved post-earthquake functionality of structures and accurate prediction of seismic performance over a wide range of earthquake scenarios. Performance based design of bridges has the potential to be applied in many unique hazards or circumstances, but performance criteria must be established beforehand. The ability to predict different damage states of a bridge pier following an earthquake can be useful in restoring service or prescribing appropriate remediation. Furthermore, most of the design guidelines are moving towards performance-based design. Recently, AASHTO has proposed *Guidelines for Performance-Based Seismic Bridge Design* (Murphy et al. 2020). Although the CHBDC first introduced PBD in the 2014 edition, it has made some significant changes in the 2019 edition (National Research Council of Canada 2019). While the CHBDC does acknowledge a need for consideration of aftershock effects, there is little guidance provided to practicing engineers. Furthermore, despite the fact that the CHBDC stipulates that the aftershock capacity of damaged bridges must be assessed based on the predicted mainshock damage, no performance limits or guidelines for assessing the post-aftershock performance are described. Therefore, there is great benefit to be realised in the

development of PBD guidelines for mainshock-aftershock seismic sequences for scenarios in which the chance to assess and repair a bridge is not possible following a recent mainshock.

## 1.3   Seismic performance of reinforced concrete bridges

Bridge piers are one of the most critical components in the bridge system that dictate the overall performance of bridges during seismic events. In reinforced concrete bridges, much of the energy imparted to the bridge structure by ground acceleration is dissipated by the deterioration of the bridge pier columns, where concrete cracking and spalling, plastic hinge formation, and reinforcement yielding and buckling mechanisms dissipate energy. Current seismic design guidelines which are implemented in North America allow all but the highest importance lifeline bridges to undergo large inelastic deformations so long as load carrying capacity is maintained and collapse does not occur. The Canadian Highway Bridge Design Code (CSA S6-19) has implemented performance-based design (PBD) as a requirement for seismic design of more important or irregular bridges. Bridges designed to PBD guidelines must demonstrate that they meet explicitly outlined performance criteria such as damage limits and service levels. This means explicit performance objectives are defined and have to be demonstrated, in contrast to traditional codes where performance objectives are implicit. For performance-based seismic design and assessment of bridges, it is critical to predict different damage states or performance levels under different ground motions (Marsh et al. 2013). Damage experienced by a bridge pier during an earthquake is a function of ductility, deformation, energy dissipation, as well as strength and stiffness degradation. In CSA S6-19, the damage-level criteria are defined as quantitative limits on concrete and reinforcement strains as well as qualitative limits on displacements or damage to bridge components as depicted in Figure 1.1.
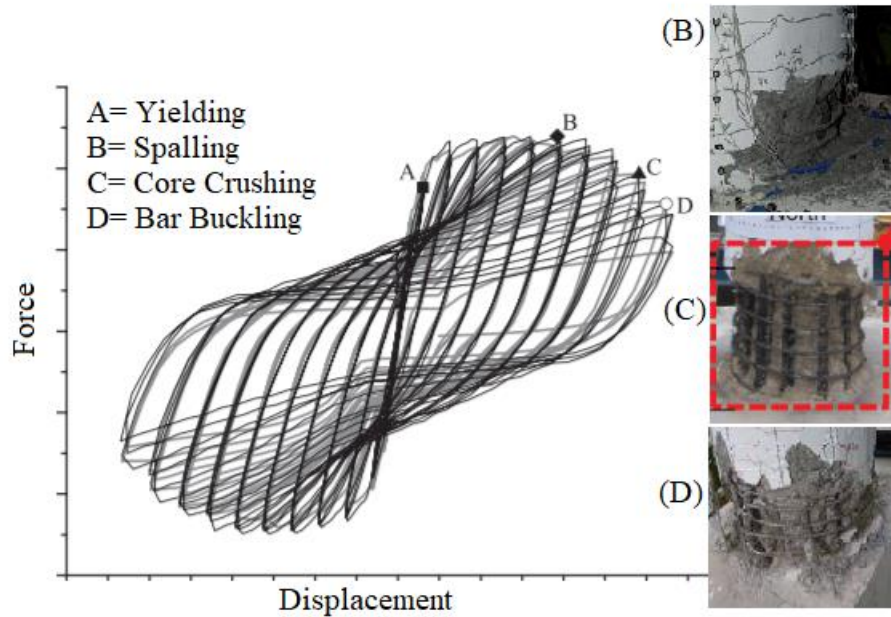
Figure 1.1 Typical definition of bridge pier performance limit states under seismic load

## 1.4 Machine Learning Regression

Machine learning (ML) tools have generated significant research interest in the past few decades, and have recently gained a foothold in seismic and structural engineering applications due to their deep learning capabilities which are able to provide accurate regression models mapped to complex functions. Moreover, ML Models are able to generate predictive models which outperform many statistical and research-intensive efforts, or reasonably generalize other computationally intensive analytical methods in a small fraction of the computational expense. The majority of research which has utilized machine learning operates under the subset of supervised machine learning, where models are trained and are constantly evaluated for their accuracy and performance among a variety of metrics. Supervised learning is further divided into regression and classification models, which use input data to generate continuous or discrete output predictions, respectively. The growing computational efficiency of modern computers and the large body of support from computer science interest in ML has allowed for the ability for researchers to rapidly develop ML models for a variety of applications.

## 1.5    Research Objective

The analytical research study detailed in this thesis has been carried out to investigate the behaviour of reinforced concrete bridge columns subjected to a suite of fifty as-recorded mainshock-aftershock groundmotion records. To provide a wider scope of data, ten ductile column configurations designed based on current PBD requirements outlined in CHBDC as well as an additional ten brittle columns, representing existing bridge piers designed without any PBD considerations, were examined. Ground motion records were separated into mainshock-only and aftershock-only components to be able to evaluate post-mainshock damage levels and to compare the additional damage incurred in the subsequent aftershocks. To quantify column capacities, quasi-static analyses in the lateral and axial directions were performed. The results of the numerical analyses were used to generate fragility functions to observe the increased vulnerability due to aftershocks, and to assemble a machine learning model to efficiently predict existing bridge column capacities. An overarching goal of this research is to study and assess the seismic performance of concrete bridge piers in order to aid in the development of performance limits for bridge piers under sequential seismic events. A summary of specific research objectives this study accomplishes are listed below:

1. Design an initial set of reinforced concrete bridge columns according to existing PBD guidelines found in the current edition of the CHBDC 2019;
2. Validate the performance of the finite element software framework using published experimental results, and establish a strain-based strength degradation scheme using strain limits based on literature;
3. Perform dynamic time history analysis of the column suite using real as-recorded mainshock-aftershock ground motion records to observe changes in key engineering demand parameters;
4. Observe effects of column performance and capacity degradation due to subsequent aftershocks;
5. Develop fragility curves for various damage levels considering aftershock effects;
6. Develop a data driven machine learning model for the prediction of axial and lateral capacity degradation in reinforced concrete bridge columns under mainshock-aftershock sequences.

## 1.6   Thesis Outline

This thesis is organized into six chapters which contain the following content:

- Chapter 2 summarizes existing research in the area of mainshock-aftershock design of bridges and structures, as well as recent studies involving machine learning methods in the field of seismic and structural engineering.
- Chapter 3 details the analytical methodology used in employing nonlinear and quasi-static finite element analysis to perform parametric studies of reinforced concrete bridge column models in both mainshock-only and post-mainshock configurations.
- Chapter 4 presents pertinent machine learning methodology used in this study and quantifies the performance of each hyperparameter tuned model when evaluating test set data. The results of the developed machine learning models are presented, and key parameters which govern the residual capacity estimation are identified and discussed.
- Chapter 5 evaluates the seismic demand of the developed bridge pier models through the use of probabilistic seismic demand models. Fragility functions for mainshock-only and mainshock-aftershock demand are developed and compared.
- Chapter 6 summarizes key research findings, draws conclusions, and outlines future research needs.

# Chapter 2    Literature Review

## 2.1    General

The sophistication of seismic design and engineering of resilient infrastructure is continuously being developed towards a holistic design protocol. The response to a changing climate and awareness of new hazards and interactions parallels the trends which shape other industries such as aviation, where significant disasters improve upon current practices, and bring awareness to flaws which remained unnoticed or were previously considered acceptable. In North America, earthquakes such as San Fernando (1971), Loma Prieta (1989), and Northridge (1994) are monumental to the seismic design profession and have shaped seismic engineering practices to ensure that the massive damage to structures, roadways, bridges, economy, as well as loss of life are mitigated.

In North America, the majority of seismic activity can be found along the west coast of the North American Plate, particularly along the Cascadia Subduction Zone which stretches several hundreds of kilometers from northern California to Vancouver, British Columbia; as well as throughout the coastal regions of land stretching north of British Columbia through to Alaska in which several additional faults are located. This geographical distribution shows resemblance to that of the research interest landscape in seismic design, and as such, California tends to be a centralized hub for seismic design initiatives in the United States. The previously mentioned San Fernando, Loma Prieta, and Northridge earthquakes all occurring in California, typically categorize infrastructure and bridge design into distinct "design eras" due to the vulnerabilities that the disasters exposed.

Provisions for seismic design of bridges in the US were first developed in 1940, where the bridge design codes specified 2% to 6% of the structure's dead weight be applied as a static maximum lateral seismic design force (Veletzos et al. 2008). In 1965 some of the first refinements to the seismic design process were introduced when CALTRANS (1999) adopted design equations which took into account amplification factors and the period of the structure, while the maximum lateral design force was also increased to 13% in some design cases. Design detailing during this pre-San Fernando period had very few considerations for reinforcement splicing and development, which typically resulted in structures with limited ductility. Due to these design practices, the older bridges were particularly vulnerable to damage even during moderate seismic events. The 1971 San Fernando Earthquake demonstrated the shortcomings of the seismic design of older bridges

and proved to be a catalyst for major changes in seismic design philosophy. Bridges still in the design phase in the short period following the earthquake were redesigned to be able to resist lateral loads scaled up by factors of 2.0 or 2.5. Consequently, the updated version of the CALTRANS Seismic Design Code released following the San Fernando Earthquake included factors such as fault proximity, site conditions, dynamic structural response, and ductile details for newly designed bridges. The new bridge seismic design code had pivoted to a design strategy which retained elasticity in the bridge superstructure, and targeted flexural failure in the columns (Moehle 1995). Despite the proposed changes and shift in design philosophy, the catastrophic damage caused during the 1989 Loma Prieta earthquake signaled that further refinement to the seismic design code was needed. CALTRANS enlisted the help of the Applied Technology Council (ATC) to perform extensive review and revision to the present design standards, criteria, specifications and practices. The ATC-32-1 report (Applied Technology Council 1996) was completed after the 1994 Northridge earthquake, marking the start of the post-Northridge design era, where all the recommended design provisions brought forth by the report were incorporated into the following edition of CALTRANS code. In Canada, the seismic design of bridges tends to trail behind the practices employed south of the border. Prior editions of the Canadian Highway Bridge Design Code take much guidance from the monumental research and development of the CALTRANS and AASHTO LRFD bridge design codes which have greatly matured since their inception.

This chapter provides a detailed review of recent literature pertaining to mainshock-aftershock design and retrofit of bridges as well as structures, machine learning applications in seismic engineering, and additional research pertaining to the increased vulnerability of structures subjected to aftershocks.

## 2.2   Significance of mainshock-aftershock consideration

For many communities, bridges are an essential component to their transportation infrastructure, where their continued service is expected to remain uninterrupted. Bridges located in regions which are seismically active are likely to experience multiple earthquake sequences during their service lives. All seismic activity presents a risk for the damage to a bridge or its components, where a subsequent repair or retrofit may be unlikely to restore the full capacity of the intact bridge. Moreover, mainshock-aftershock (MS-AS) events, present little to no time to mobilize repair to

the already damaged structure, which presents a compounding risk to the fragility of bridges. Typically, sequences which involve multiple dependent earthquakes are defined in terms of components of foreshocks, mainshock, and aftershocks based on their relative intensity. As a multiple earthquake sequence occurs, the current earthquake with the largest intensity is termed the mainshock, with the preceding excitations being denoted foreshocks, and the following labelled aftershocks, as depicted in Figure 2.1. The frequency of occurrence of aftershocks can be approximated empirically using Omori's law (1894), where the likelihood decreases exponentially with time. Additionally, Bath's law (1965) depicts the decrease in magnitude of the largest aftershock as compared to the mainshock. A typical MS-AS record is shown in Figure 2.2.
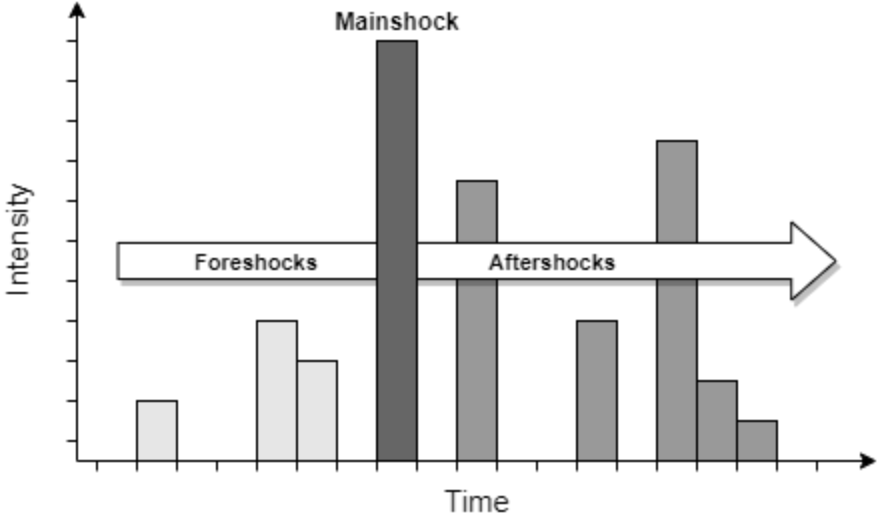


Figure 2.1 Intensity versus time of mainshock and aftershock sequences
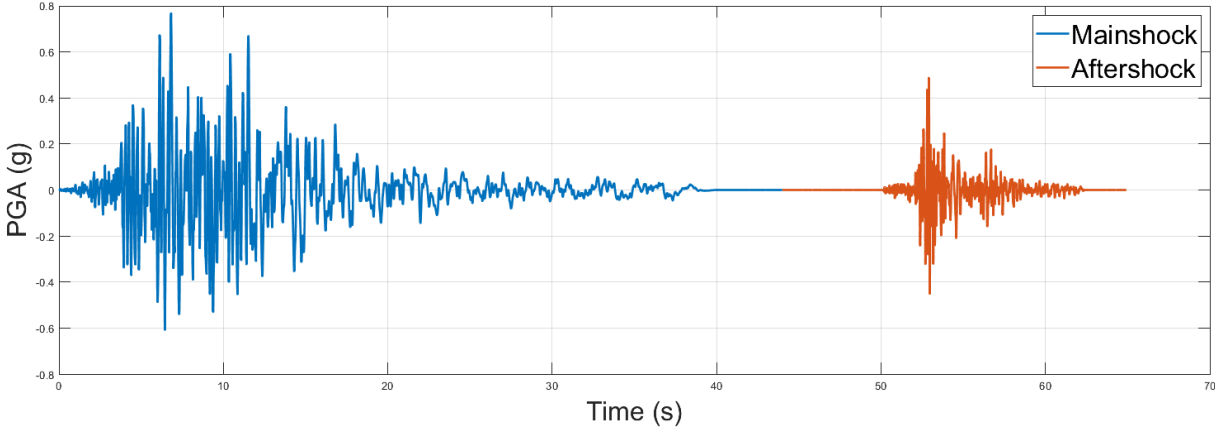


Figure 2.2 Typical time history of mainshock and aftershock sequence

8

2.2.1 Aftershock record selection

Past studies were cognizant of the potential for increased vulnerability that aftershocks pose, however were not able to apply real MS-AS records. Instead, a common technique of reiterating the original mainshock record was employed, termed back-to-back application of mainshocks. Luco et al. (2004) contributed some of the first analytical research for demonstrating the increased vulnerability of structures subjected to MS-AS sequences, where the residual capacity of a 3-storey steel moment resisting frame (SMRF) building was used as a case study. Artificial MS-AS records were constructed using the back-to-back scaled mainshock technique, where the resulting roof drift and residual roof drift IMs generated from the NLTHA were used to calibrate a static pushover for specifying a maximum aftershock intensity which may be withstood by the structure without collapse. Similarly, Li and Ellingwood (2007) proposed a probabilistic damage and condition assessment framework for aftershock vulnerability of two different SMRF buildings; wherein two cases of artificial MS-AS were developed by using back-to-back 'repeated' or 'randomized' methods which repeat the unscaled mainshock sequence or use another mainshock from the bin, respectively. The study concluded that the characteristics of the aftershocks have a large influence of the damage outcome of the moment frames studied therein. Repeated mainshocks for the back-to-back evaluation produced a divergence in the damage evaluation to the structure, as compared to the randomized aftershock assessment. The large variance in the methods highlighted the need for the appropriate use of mainshock-aftershock records, where the differences in ground motion characteristics are considered.

As part of a case study to investigate the effectiveness of back-to-back ground motion records, Goda (2015) utilised their previously designed wood-frame residential house models (Goda and Salami 2014) in order to study the effects of aftershock record selection for collapse vulnerability assessment. The model was subjected to a benchmark suite of 30 commonly used back-to-back mainshock records as well as a set of 90 real MS-AS records assembled using the K-NET/KiK-net database for earthquakes in Japan. The building response obtained from performing IDA when employing both sets of records presented compelling evidence against the use of back-to-back sequences, as the structural response was improperly captured and varied significantly. It was suggested that the use of real MS-AS records is desirable in capturing the motion characteristics

representative of the location specific seismic environment being considered. More recently, Shin and Kim (2017) explored the effects of frequency content of aftershock ground motions on reinforced concrete bridge pier responses. Using three column experimental results from literature, finite element models were modelled using OpenSees and validated based on the resulting force-displacement outputs from cyclic loading analysis. The seismic response under dynamic loading of the columns was explored to demonstrate the importance of properly selected ground motion sequences. Real MS-AS motion records, back-to-back scaled mainshock records, and spectrally matched mainshock motion to the aftershock motion (MS-SM) were chosen as the three test cases. The synthesized aftershock responses were compared to the real MS-AS sequence response, where it was concluded that back-to-back sequences overestimated maximum displacements of the columns. Furthermore, the results of the spectrally matched MS-SM aftershocks more closely resembled the real MS-AS response and are recommended in place of MS-MS synthesis.

2.2.2 Post-Mainshock bridge capacity assessment

The decision to re-open a bridge following a damaging earthquake is dependent upon the remaining capacity of the bridge to support self weight as well as traffic loads. Another level of complexity to factor into this decision is presented through the potential for further damage via aftershocks which may yet occur. Yeo and Cornell (2005) presented a decision analytic framework in which the life cycle loss models are employed considering pre- and post-mainshock scenarios. Franchin and Pinto (2009) proposed a criterion for the decision making process as to whether a bridge can remain open, or to limit traffic after a mainshock has occurred based on the survival probability of the post-MS bridge compared to the intact structure. Additionally, aftershock survival probability is also considered and decays with time, therefore a waiting period may be employed before a decision to allow traffic on a particular bridge is made. Moreover, Alessandri et al. (2013) developed a probabilistic method for aftershock risk assessment that combines in-situ site inspection and analytical assessment. Using Bayesian updating, the analytical model is compared to match actual conditions as observed from inspection and the model is updated accordingly. The developed risk assessment method was applied to a thirteen span RC highway viaduct, where the sensitivity of the framework to the Bayesian updating was highlighted, especially so when real damage observed by inspection did not match the analytical model prediction. Moreover, the risk assessment procedure was compared to the previous two proposed

methods and Alessandri et al. (2013) found that theirs lead to reasonably shorter re-opening times when subjected to low intensity MS-AS events.

Furthermore, Terzic and Stojadinović (2010) explored post-earthquake traffic capacity of modern bridges in California. Analytical and experimental methods were combined to evaluate the post-earthquake load capacity of an overpass bridge, where experimental studies into the behaviour of seismically induced damage and remaining column capacity of circular RC bridge columns were performed and used in calibrating the following analytical studies. A hybrid simulation technique was used to validate the proposed finite element models for the overpass bridge, and to calculate the post-earthquake load capacity. An extensive parametric study followed to investigate the effects of different ground motions and model parameters. It was discovered in the experimental study that a typical overpass bridge in California is capable of maintaining truck loading immediately after a very strong earthquake since although the damage in the plastic hinge region of the column specimen was pronounced, none of the specimen's reinforcing bars or spiral reinforcing fractured. The parametric study and analytical models further revealed that bridge parameters such as the abutment type, residual drift of the bridge, position of the truck on the bridge relative to the superstructure's centerline, and the ultimate strain in column reinforcing bars carried a significant influence on the post-earthquake truck load capacity that warrants further research. While not specifically investigating the effects of MS-AS sequences, Terzic and Stojadinović's study was the first experimental study of its kind in exploring post-earthquake bridge pier load capacity. The progression of studies into post-earthquake capacity of bridges contributes to the understanding of post-mainshock capacities for MS-AS multihazard interactions.

## 2.3   Existing research in mainshock-aftershock design of structures

On a macro level, research surrounding consideration of aftershock design for highway bridges mainly focuses on fragility assessment and retrofitting techniques. Fragility assessment is valuable to infrastructure design and risk quantification as it can more easily facilitate decision making of retrofit and design strategies for a particular hazard. Seismic vulnerability of highway bridges is frequently expressed using fragility curves, in which the conditional probability of sustaining a particular level of damage is related to an earthquake intensity measure.

2.3.1 Aftershock fragility assessment of structures

Dong and Frangopol (2015) explored a probabilistic approach for risk assessment under MS-AS ground motions, which combined bridge seismic vulnerability and economic repair loss considerations to serve for enabling rapid decision making. They considered resilience as a performance factor to quantify the recovery of bridges under MS only and MS-AS sequence (Figure 2.3). A Monte-Carlo simulation for mainshock-aftershock sequences was implemented in this study to account for the uncertainty in mainshock frequency, magnitude, and ground motion duration. Subsequently, a representative single degree of freedom (SDOF) bridge model was used to simulate mainshock only and mainshock-aftershock loading in order to collect demand parameters for the assembly of fragility curves for both responses. A comparison of the fragility curves for the established damage states in the study made for compelling evidence that aftershocks increase the vulnerability and diminished residual functionality of the bridge studied.
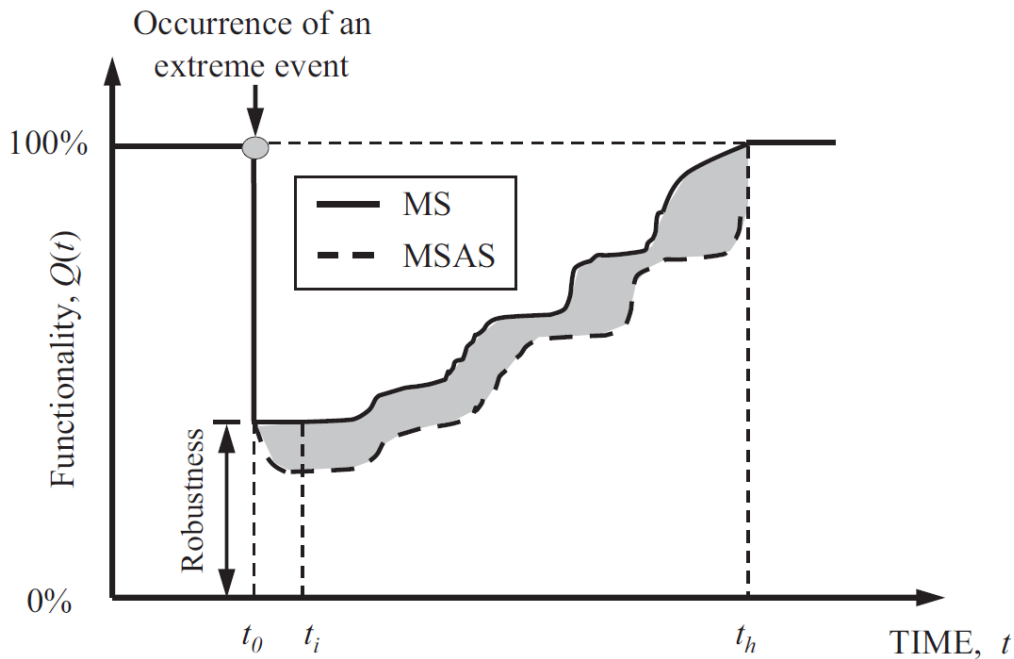


Figure 2.3 Conceptual illustration for the resilience and functionality of bridges under MS and MS-AS sequence (adapted from Dong and Frangopol 2015)

In a related study, Ghosh et al. (2015) developed a probabilistic damage accumulation and fragility framework for bridges subjected to multiple earthquake hazards, where a case-study single column, box girder highway bridge located in California was developed using OpenSEES to

demonstrate the probability of structural damage due to repeated seismic excitations. Two scenarios were explored in this study such as multiple mainshocks during the service life of the bridge, and multiple aftershocks following a single mainshock. Structural damage accumulation was forecasted through the use of the Park and Ang Damage Index (PA-DI) (Park and Ang 1985), where regression models were developed using time history analysis results to correlate damage as a function of earthquake intensity and damage history. The study demonstrates the increase of structural vulnerability of the studied bridge when exposed to either scenario, and the developed framework serves as a potential tool for rapid bridge repair strategies following such events, or for risk mitigation over the service life of such bridges by assisting in the retrofit or structural upgrade decision making process.

Xie et al. (2012) evaluated the aftershock seismic performance of a 2000-meter steel tower suspension bridge modelled in ABAQUS using elasto-plastic beam elements to consider accumulated seismic damage, and foundation springs to consider soil-structure interaction. Five MS-AS ground motions were selected for analysis, and seismic damage accumulation was captured using McCabe and Hall's low-cycle fatigue theory (1989). The authors concluded that seismic behaviour of the suspension tower behaved similarly to a framed structure under transverse excitation with damage vulnerability near junctions of the tower shafts and cross beams. Longitudinal excitations of the suspension bridge however placed tower vulnerability at its foundation and upper portion. Due to a long natural period of the bridge, and a low cumulative damage resulting from the aftershock, the study found that aftershock effects may be ignored for this long span suspension bridge, and instead seismic damage can be determined by superimposing the mainshock and aftershock excitations.

More recently, Omranian et al. (2018b) investigated the vulnerability of skewed highway bridges subjected to mainshock-aftershock sequences. Using analytical bridge models with skew parameters varying between 20° and 80°, MS-only and sequential MS-AS time history analysis under seven incidence angles was performed. Cloud-based fragility curves were developed for each incidence angle, with four different damage levels observed and compared to the mainshock fragility functions established by HAZUS (Hazus 2011). The resulting fragility curves developed in the study showed the significance of multiple incidence angle consideration for skewed bridges, and more importantly demonstrated that the fragility functions provided in HAZUS are

unconservative since the effects of aftershocks lead to increased fragility which is more profound in skewed bridges.

Additionally, Pang and Wu (2018) used a selection of 8 continuous multi-span RC bridges for component level fragility analysis subjected to 75 recorded MS-AS sequences. Initially, component-level fragility curves were developed based on pier and bearing responses obtained during dynamic analysis. Monte Carlo simulation was implemented using multi-variate normal distribution of the component responses to derive system level fragility curves at slight, moderate, extensive, and complete damage states. The resulting joint-PSDM's developed in the study support the need for the consideration of aftershock effects as bridge vulnerability is increased on both component and system levels, respectively.

Aftershock effects on the seismic design of structures, on the other hand, has received more research attention, and has seen very similar outcomes. Tesfamariam and Goda (2017) performed an aftershock seismic vulnerability evaluation of a high-rise reinforced concrete shear wall building located in Vancouver, British Columbia. A suite of 50 MS-only and 50 MS-AS ground motion records were selected, with an even distribution of crustal, inslab, and interface excitations chosen to properly represent the range of possible earthquakes present in western British Columbia. Nonlinear time history analysis was performed for the 15-storey gravity column structure, where the structural response to the unscaled ground motions was used to develop seismic demand prediction models as well as fragility curves. Tesfamariam and Goda explored drift-based and energy-based EDP's and made the distinction that drift based damage indices were not suitable for long duration earthquakes such as MS-AS sequences as they underestimated vulnerability. Furthermore, IMs such as spectral acceleration at the fundamental period ($S_a(T_1)$), Arias intensity (AI), cumulative absolute velocity (CAV), and significant duration of ground motion ($D_{5-95\%}$) were evaluated for efficiency and CAV was concluded to be most appropriate for the established Mehanny–Deierlein damage index. Last, the study made clear the impact of major aftershocks on the vulnerability of the case study building, where the influence of major aftershocks increased the damage index values by approximately 40% for a given probability level.

Abdollahzadeh et al. (2019a) modelled 4, 8, and 12-storey steel moment resisting frames using performance based plastic design (PBPD) as well as conventional elastic design. The buildings were subjected to 10 mainshock aftershock sequences from the PEER strong motion database to

14

explore the benefits of the plastic design method through demand parameters such as story drift, energy distribution and plastic hinge distribution. Response spectra corresponding to 10% and 2% probability of exceedance in 50 years were defined and used to determine ground motion scaling for two hazard levels. It was observed that the moment frames designed using PBPD exhibited improved aftershock performance by way of diminished story drift when compared to the conventionally designed frames. Moreover, the authors concluded that during hazard level 2 sequences, conventionally designed steel moment frames experienced undesirable performance during aftershock where additional members exhibited nonlinear behaviour.

Additionally, Abdollahzadeh et al. (2019b) studied several more three-bay SMRF buildings designed using PBPD. Once more, the selected MS-AS ground motion records were scaled based on response spectra corresponding to 10% and 2% probability of exceedance in 50 years. IDA was performed for each of the model configurations using MS-only and MS-AS sequences to obtain the corresponding ductility and ductility reduction factors, $\mu$ and $R\mu$. Furthermore, the energy modification factor $\gamma$ which is a function of the previous ductility factors was calculated for both earthquake scenarios, and used to generate a $\gamma_{MS+AS}$ / $\gamma_{MS}$ modification ratio for each of the SMRF structures. A curve was fitted to the resulting modification ratios corresponding to the design period of the frames, and a modified PBPD which considers aftershock capacity was formulated to redesign the SMRF for NLTHA. More importantly, the results of the NLTHA showed performance of the modified PBPD frames under hazard level 2 were favourable whereas the unmodified frames exhibited the formation of additional plastic hinges or even collapse.

Mangalathu et al. (2019b) explored the time dependent seismic risk of aftershocks in California bridges, with uncertainties in damage states following a specified mainshock. They proposed a methodology (Figure 2.4) to three different eras (pre-1971, 1971-1990, post-1990) of California highway bridges using a Markov risk assessment framework to account for the probabilistic transition of the bridge through different damage states and time dependent aftershock hazards. They defined the mainshock and mainshock–aftershock physical damage in bridges using a mutually exclusive and collectively exhaustive limit states. They found a direct relationship between the age of the bridge and increased aftershock vulnerability for the older bridges.
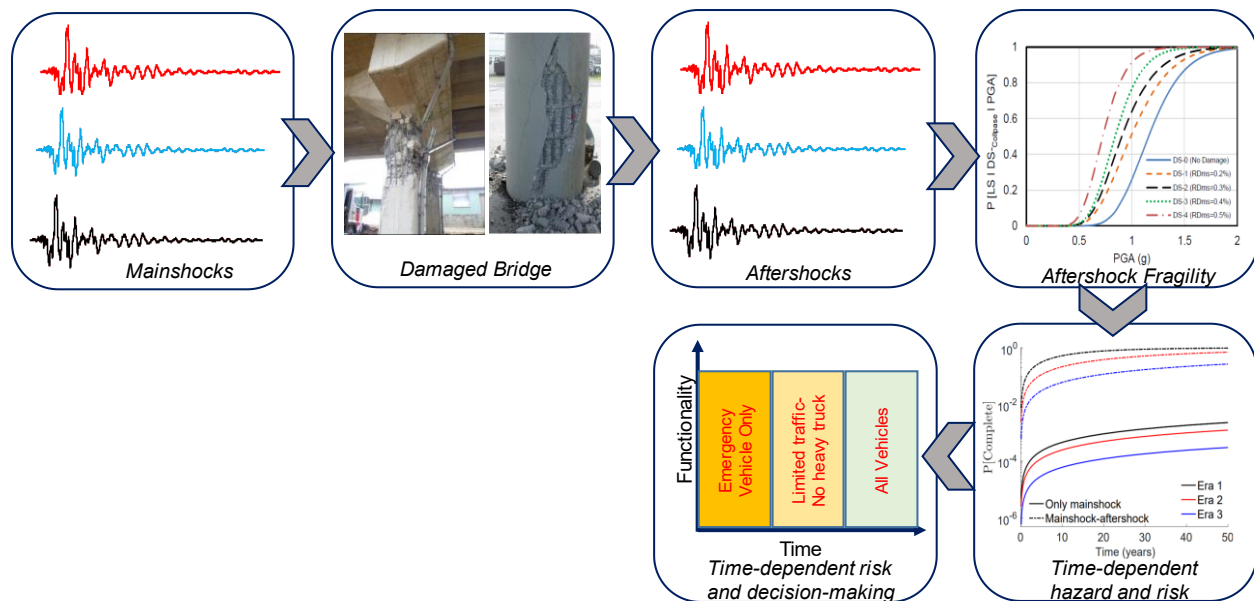
Figure 2.4: Aftershock vulnerability and time dependent risk assessment of bridges (adapted from Mangalathu et al. 2019)

Liang et al. (2020) investigated the time-varying seismic fragility of offshore bridges under MS-AS sequence. They considered time-dependent material properties of bridge components due to aging and deterioration and analyzed the bridge based on time-varying seismic action in the entire life cycle. They concluded that with increasing bridge material deterioration, the vulnerability increases under MS-AS sequential ground motions.

Todorov and Billah (2020) evaluated the seismic fragility of concrete bridge piers reinforced with two different types of Shape Memory Alloy (e.g. Ni-Ti and Fe-based) rebars under mainshock ground motions followed by aftershocks. The seismic fragility of the SMA-RC bridge piers was compared with conventional steel-reinforced concrete (Steel-RC) bridge piers. They found that the Steel-RC bridge pier is more susceptible to collapse when subjected to MS-AS sequence irrespective of damage induced by mainshock events as compared to the SMA-RC bridge pier.

## 2.3.2 Aftershock rehabilitation of structures

Research and development of novel construction materials and technologies for seismic risk mitigation and performance improvement techniques exist and are continually evolving. The use of materials such as jacket sleeves for retrofitting, Shape Memory Alloy (SMA), and composite reinforcement are reviewed, with some having already been implemented in construction

applications. There exists much overlap in material technologies for the general increase in a structure's seismic resiliency, the evolution of construction practices, and the retrofitting of bridges damaged by mainshock-only events; as such, the review of all construction advancements in bridge design would be unnecessarily exhaustive.

Fakharifar et al. (2015a; b) performed comprehensive analytical studies on the collapse vulnerability of substandard reinforced concrete bridge piers which have sustained damage through a mainshock ground motion. Post-Mainshock damaged bridge piers from a prototype two span single column bridge bent with lap-splice deficiency at the column-footing interface were rehabilitated with Fibre Reinforced Polymer (FRP), conventional thick steel, and hybrid repair jackets and were evaluated. Using Incremental Dynamic Analysis (IDA), Fakharifar et al. evaluated the efficacy of different repair jackets on the post-repair behaviour of the RC bridge subjected to aftershock sequences. It was found that the application of repair jackets on damaged bridge piers were less effective for cases of severe MS-moderate AS sequences compared to severe MS-severe AS scenario. However, repair jackets remained essential for severe MS-moderate AS sequence. The performance of conventional thick steel jackets was observed to have a higher fragility as compared to the hybrid and Carbon Fiber Reinforced Polymer (CFRP) jackets; however, steel jackets exhibited larger energy dissipation as compared to the CFRP.

Similarly, Omranian et al. (2018a) investigated the post-mainshock seismic fragility of a skewed RC bridge retrofitted with FRP. Using two analytical models with and without CFRP jacket retrofitting, and performing both mainshock only (MS-only) and Mainshock-Aftershock (MS-AS) ground motion analysis, fragility curves were developed based on four damage states. By comparing the fragility of the bridge with and without FRP it was revealed that FRP confinement improves the seismic performance of the structure and decreases the probability of failure in the studied skew bridge. Additionally, FRP confinement has a more significant effect on the seismic performance of the bridge particularly in the higher levels of damage state such as severe and complete.

Jeon et al. (2016) developed a framework (Figure 2.5) for aftershock fragility given an initial post-mainshock damage state. A repair element, *rcube* (Lee et al. 2009) was implemented in the Zeus-NL finite element software to verify the authors' model against post-repaired bridge column experimental results (Chai et al. 1991; Haroun et al. 2003; Ohtaki et al. 1997; Youm et al. 2006).

A case study bridge located in California that is not seismically designed was selected and three models were developed to assess the aftershock behaviour of this bridge without repairs, and two retrofitted models with steel and FRP jackets respectively. Under the proposed framework the as-built bridge is selected and limit states are defined. The bridge then undergoes N number of ground motions to achieve its initial post-mainshock damage state. In this report the options to leave the bridge unrepaired, or to repair with steel or FRP jackets are then considered. The bridge is then subjected to N number of aftershock ground motions that have been modified using scaling method, and fragility curves are finally developed for the model. Jeon et al. (2016) selected a suite of 30 pairs of ground motions in their research and concluded that both steel and FRP jackets are suitable choices in seismic rehabilitation. The bridge model using the steel jacket was shown to be less seismically vulnerable, however both jackets' effect on collapse probability varied within a small margin of 5%. Additionally, the influence of the initial damage states was shown to have a great variance on the bridge's response to successive earthquakes where the more significantly damaged columns experienced considerable inelastic action during the mainshock.
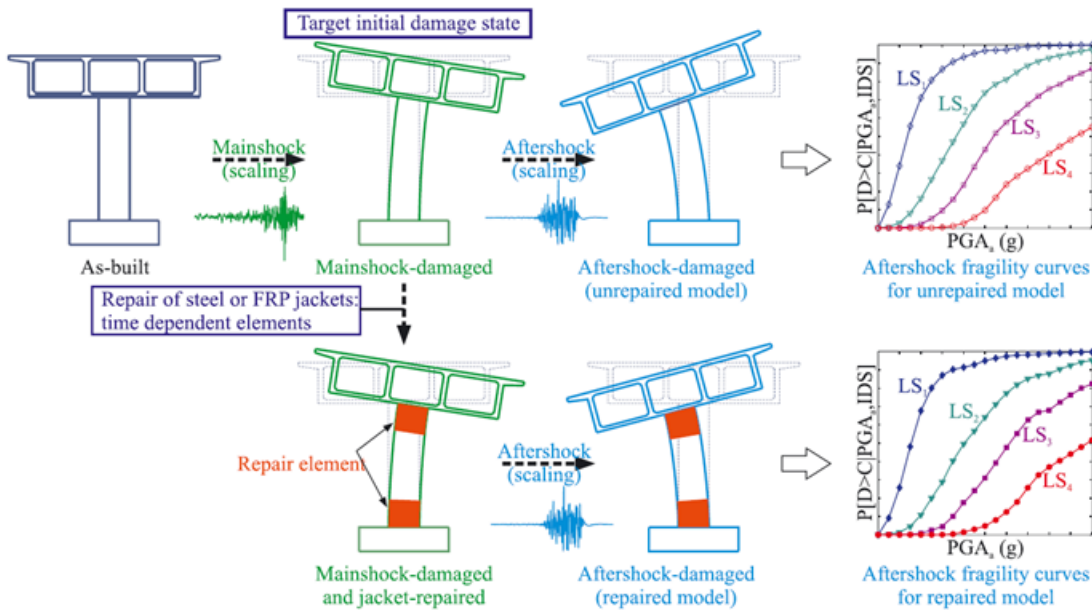


Figure 2.5 Framework for aftershock fragility assessment of unrepaired and repaired bridges (adapted from Jeon et al. 2016)

Jung and Andrawes (2018) performed analytical studies into the effects of retrofitted external Shape Memory Alloy confinement in the plastic hinge regions of multiple frame bridge piers. Four

18

levels of active SMA confinement ranging from 1.03 to 2.07 MPa were demonstrated to prevent concrete crushing under MS-AS sequences, with concrete strength loss being reduced under higher levels of confinement. Furthermore, the SMA confinement was also observed to reduce reinforcing bar fatigue damage, along with reduced residual hinge openings at bridge joints. By monitoring local and global damage states, the effects of the SMA retrofit were found to improve seismic performance of the flexure failure dominated model bridge.

## 2.4   Existing research in machine learning applications in seismic/structural engineering

Due to recent technological progress, Machine Learning (ML) has become a broadly powerful tool. Machine learning techniques are becoming attractive in the field of structural and earthquake engineering for their rapid prediction and classification of failure modes, among other applications. Researchers in the field of structural engineering have utilized machine learning techniques for several applications including failure mode classification, strength regression, and fragility curve regression.

Pang et al. (2014) utilized artificial neural network (ANN) regression to generate fragility curves of highway bridges, bypassing the computational power-intensive incremental dynamic analysis (IDA) required to generate them. Similarly, Mangalathu et al. (2018) applied ANN regression to generate bridge specific fragility curves, without the need to group bridge classes as seen in traditional regional risk assessment. In another study, Mangalathu and Jeon (2018) applied different machine learning techniques to classify failure modes and subsequently predict associated shear strength in beam-column joints. Using stepwise and LASSO regression techniques, Xie and DesRoches (2019) identified the influential parameters that affect the seismic demands of different bridge components. Luo and Paal (2018) proposed a novel machine learning model to predict RC column backbone curves in the form of the least squares support vector machine trained using an advanced grid search algorithm (GSA) to perform hyperparameter optimization. The proposed ML-BCV approach demonstrated superior accuracy and robustness when compared to traditional modeling approaches. In another study, Luo and Paal (2019) proposed an additional novel machine learning method for RC column drift capacity regression, where the least squares support vector machine is optimized using a hybrid coupled simulated annealing and grid search locally weighted global optimization scheme. Mangalathu and Burton (2019) further explored the limitations of machine learning by applying a long short-term memory

(LSTM) deep learning model for the classification of building damage severity and spatial distribution using a large dataset of ATC-20 textual damage descriptors. Xie et al. (2020) presented a comprehensive review on the application of different ML techniques in earthquake engineering focusing on seismic hazard analysis, damage identification, fragility assessment, and structural control. Using 40000 existing bridge dataset, Alipour et al. (2017) used different ML techniques such as decision trees and random forests to evaluate the load-capacity rating of existing highway bridges. Figueiredo et al. (2019) proposed a hybrid finite element–based machine-learning approach for damage detection in existing bridges. They concluded that the developed hybrid method resulted in an improved damage detection performance for large scale civil engineering structures.

In rapid failure mode identification of seismic force-resisting systems that parallel this research, Mangalathu and Jeon (2019) explored the efficiency of several different machine learning methods including ANN, naïve Bayes, random forests (RF), and quadratic discriminant analysis in classifying column failure modes. ANN predictions were compared with existing predictive models and were found to have greater accuracy, and the ability to distinguish between shear and flexure-shear failure modes. Furthermore, Mangalathu et al. (2020) explored the classification of failure modes in RC shear walls with the application of eight machine learning models including four boosting methods such as adaptive boosting (AdaBoost), extreme gradient boosting (XGBoost), light gradient boosting machine (LightGBM), and categorical boosting (CatBoost). They suggested Random Forest as the suitable ML technique for predicting the shear wall failure mode.

Other areas of civil engineering benefit from the computational savings that machine learning models can provide through metamodeling which bypasses intensive analysis that is normally used. Keshtegar and Nehdi (2020) utilized metamodeling via support vector regression (SVR) and feedforward backpropagated neural networks (FFBNN) to predict the maximum displacement of a carbon nanotube reinforced pipe subjected to seismic loading compared to dynamic analysis methods. Ghosh et al. (2013) used machine learning regression for multi-dimensional metamodeling of the seismic response of bridge components using techniques such as polynomial response surface models (PRSM), multivariate adaptive regression splines (MARS), radial basis function networks (RBFN), and support vector regression. Additionally, Shekhar and Ghosh

(2020) used metamodeling to establish a framework for the prediction of bridge life cycle cost by pairing fragility models with ground motion intensity and field measurable bridge parameters, resulting in a tool for decision makers to efficiently invest money in seismic upgrades for bridges. Similarly, Bandini et al. (2019) developed surrogate models using PRSMs for investigating the seismic vulnerability of a case study bridge in Quebec, where fragility surfaces were developed for bridge seismic vulnerability with varying amounts of transverse reinforcement ratios in the bridge pier columns. To illustrate the capabilities of data-driven machine learning studies, a graphical representation of how different ML techniques can be used for identifying the seismic performance limits of bridge piers are summarized in Figure 2.6.

## 2.5    Summary

It is evident that the combined hazard of aftershock sequences presents an increased vulnerability to both buildings and bridges alike. To the author's knowledge, no investigations into the adequacy of the Canadian Highway Bridge Design Code's seismic PBD have been performed to study the effects of aftershocks. As such, the merits of this study are justified in exploring the development of a mainshock-aftershock fragility assessment and capacity forecasting framework. Furthermore, the explicit capacity prediction of bridge piers following seismic events also presents the need for refinement, and machine learning techniques would enable a model to rapidly assess bridge condition, or to serve as a tool for the consideration of post-MS and post-AS capacity design.
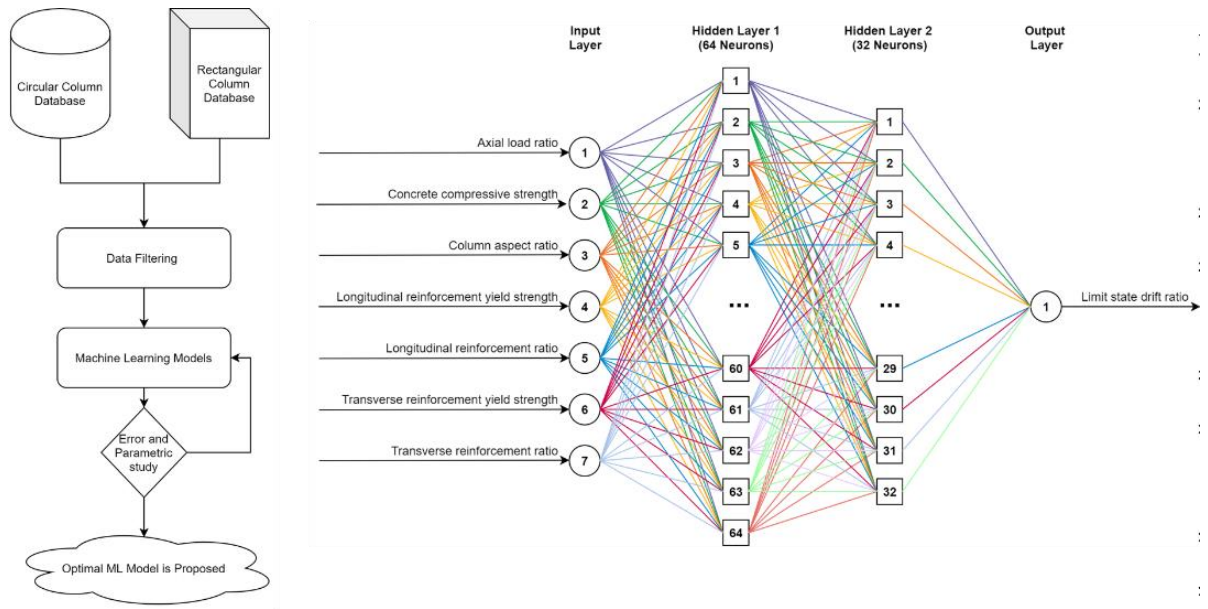
Figure 2.6 Machine learning implementations for bridge pier seismic performance identification

# Chapter 3    Analytical Modeling and Analysis of RC Bridge Pier under Mainshock-Aftershock Ground motions

## 3.1    General

The advances in the capabilities of finite element modelling have enabled researchers to capture complex nonlinear relationships of reinforced concrete structural systems with a reduced need for expensive and time-consuming experimental data. To establish a deeper understanding in structural damage and post-earthquake capacities, an array of bridge piers having different material properties, fundamental periods of vibration, and ductile detailing are considered in this study. The bridge piers are assumed to be part of a major route bridge located in Vancouver, British Columbia and have been designed following the performance-based seismic design requirements as outlined in the Canadian Highway Bridge Design Code. A fiber modelling approach which considers material and geometrical nonlinearity is realized through the finite element framework, OpenSEES (Mazzoni et al. 2006). The response of the columns is examined under monotonic and dynamic earthquake loading, where a strain-based degradation scheme is introduced. To investigate the seismic responses of the prototype bridge piers, 50 as-recorded earthquake excitations at 475- and 2475-year return periods which include aftershocks, are utilized to evaluate the likelihood of exceeding the seismic capacity of the bridge piers when subjected to aftershocks.

## 3.2    Design of prototype bridge piers

The performance of circular bridge pier prototypes representative of those commonly found in highway bridges throughout Canada have been detailed in the following sections. The bridge piers are assumed to be part of a multi-span major route bridge located in Vancouver, British Columbia and have been designed following the performance-based seismic design requirements as outlined in the 2019 edition of the CHBDC (CSA S6-19) (National Research Council of Canada 2019). A site-specific soil condition for the prototype bridge is chosen as soil class-D, which the CHBDC identifies as stiff soil having average shear wave velocity: $180 < \bar{V}_{s30} < 360$ m/s. The response spectra corresponding to different return periods in soil class-D is developed and shown in Figure 3.1.
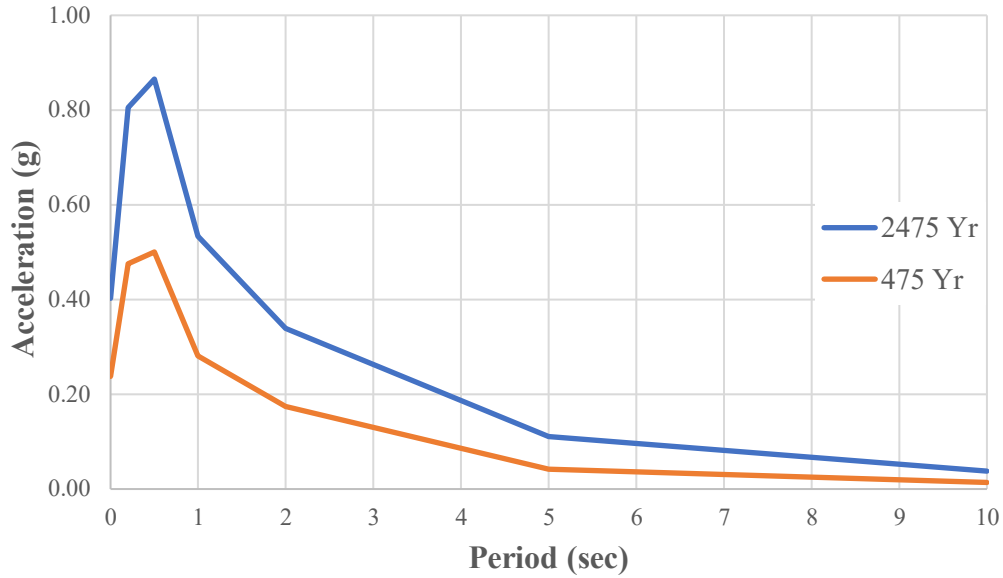
Figure 3.1 Response spectrum of bridge site location in Vancouver BC, soil class-D

Performance levels for three different categories of bridges, such as Lifeline, Major Route, and Other are defined in S6-19. Table 3.1 summarizes the performance levels defined by CHBDC as a combination of service and damage levels to be achieved under different intensities of ground motion corresponding to 475, 975, and 2475-year return periods. Since the bridge piers are part of a major route bridge, they must satisfy the performance requirements for the service and damage levels for 475- and 2475-year return period earthquakes.

Table 3.1 Performance levels for different bridge types (CSA-S6-19)

| Ground motion probability of exceedance per 50 years (return period) | Lifeline bridges | | Major route bridges | | Other bridges | |
|---|---|---|---|---|---|---|
| | Service | Damage | Service | Damage | Service | Damage |
| 10% (475 years) | — | — | *Immediate* | *Minimal* | *Service limited* | *Repairable* |
| 5% (975 years) | *Immediate* | *Minimal* | — | — | — | — |
| 2% (2475 years) | *Service limited* | *Repairable* | *Service disruption* | *Extensive* | *Life safety* | *Probable replacement* |

The performance levels defined by CHBDC relate to a set of performance criteria that describe acceptable damage levels which relate to the structure's usability following an earthquake. In the context of performance-based design, performance criteria are defined in terms of material strain (concrete and longitudinal reinforcement strain). Additional limits on displacement or damage to bridge components such as main structural members, connections, bearings, joints, restrainers, and foundations are also specified by the CHBDC; however, the focus of this study is the bridge pier only, whose performance criteria have been defined in Table 3.2, where the fiber section steel ($\varepsilon_s$) and concrete ($\varepsilon_c$) material strains are observed.

Table 3.2 Performance criteria for reinforced concrete bridges (CSA-S6-19)

| Damage Level | Material Observed | Performance Criteria |
|---|---|---|
| Minimal | concrete | $\varepsilon_c \leq 0.006$ |
| | reinforcing steel | $\varepsilon_s \leq 0.010$ |
| Repairable | reinforcing steel | $\varepsilon_s \leq 0.025$ |
| Extensive | concrete | Core concrete not permitted to exceed 80% of ultimate strain |
| | reinforcing steel | $\varepsilon_s \leq 0.050$ |
| Probable | concrete | Core crushing not permitted to occur |
| replacement | reinforcing steel | $\varepsilon_s \leq 0.075$ |

The column test matrix which makes up the analytical experiments of this research consists of 20 columns. The first 10 columns, denoted as C1 through C10 are designed using the current PBD requirements. In the preliminary design of these columns, diameter, aspect ratios, axial load ratios, and concrete compressive strength are defined to represent a large range of typical configurations. Reinforcing steel detailing is designed preliminarily in order to satisfy CHBDC clauses 4.7.5.2.5 and 8.8.5.8:

Minimum ratio of spiral reinforcement

*(CSA S6-19 Cl.4.7.5.2.5)*

$$\rho_s \geq 0.12 \frac{f_c{}'}{f_y} \left[ 0.5 + \frac{1.25 P_f}{\Phi_c f_c' A_g} \right]$$

(1)

Minimum longitudinal reinforcement

$$\frac{A_s f_y}{A_g f_c'} + \frac{A_{ps} f_{pu}}{A_g f_c'} \geq 0.135$$

*(CSA S6-19 Cl.8.8.5.8)*

(2)

Where $f_c'$ is the column concrete compressive strength, $f_y$ is the yield strength of the reinforcement, $P_f$ is the axial load, $\Phi_c$ is the concrete resistance factor, $A_g$ is the gross area of the column section, $A_s$ is the cumulative sectional area of longitudinal reinforcement, $A_{ps}$ is the cumulative sectional area of prestressed longitudinal reinforcement, and $f_{pu}$ is the yield strength of the prestressed longitudinal reinforcement.

Furthermore, an iterative design procedure is implemented where the steel detailing is the design variable. Inelastic static pushover analysis (SPO) is performed where steel and concrete material strains are collected, and the longitudinal reinforcement ratio are incrementally adjusted until the bridge pier meets the performance criteria for minimal and extensive damage levels. Using the defined axial load ratio to determine the pier's lumped mass, $m$, and moment–curvature analysis to determined effective stiffness of the bridge pier, $k$, the fundamental period of the bridge pier is calculated using the following equation:

$$T = 2\pi \sqrt{\frac{m}{k}}$$

(3)

Where the corresponding fundamental period is used to determine design spectral acceleration $S_a$ of the bridge pier using the response spectra in Figure 3.1. Two design spectral displacements are determined for each of the earthquake return periods (i.e., 475-year and 2475-year) using the following equation provided in Cl. 4.4.3.4 of the CHBDC:

$$S_d(T) = 250 * S_a(T) * T^2$$

(4)

The spectral displacement values correspond to the displacement limits of the bridge pier during SPO analysis, in which the performance criteria must not occur before the $S_d$ limits to satisfy design conditions. Figure 3.2 has illustrated the capacity curve for the first column which was designed in this study. The two shaded areas represent the minimal and extensive limits, and as can be seen in the figure, all performance limits occur at larger displacement values which demonstrates a PBD-compliant design.
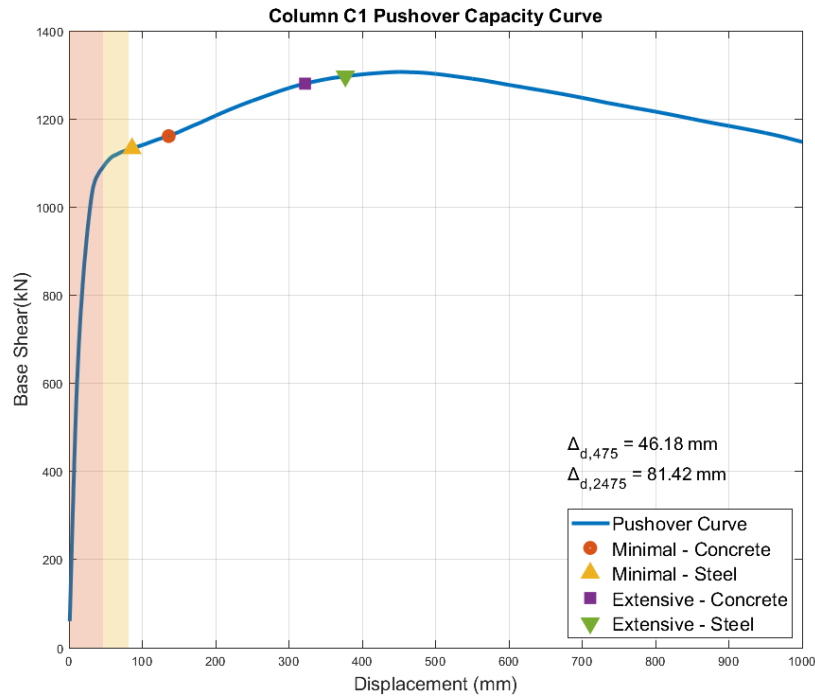
Figure 3.2 Column C1 static pushover capacity curve

The final designs for columns C1 – C10 have been summarized in Table 3.3. Final designs for columns C11 - C20 have been summarized in Table 3.4 and represent existing bridge piers with deficient transverse reinforcement such as the detailing found in Canadian bridges constructed before 2000. Although aging bridge piers would also have reduced longitudinal reinforcement and lower grade rebars, these parameters have been maintained to compare the effects of transverse reinforcement detailing only.

27

Table 3.3 Final design parameters for PBD-compliant bridge piers

| | C1 | C2 | C3 | C4 | C5 | C6 | C7 | C8 | C9 | C10 |
|---|---|---|---|---|---|---|---|---|---|---|
| **Diameter (mm)** | 1500 | 1500 | 1500 | 1500 | 1500 | 1500 | 1500 | 1500 | 1500 | 1500 |
| **Aspect Ratio** | 5 | 7 | 9 | 5 | 7 | 9 | 5 | 7 | 9 | 7 |
| **Axial Load Ratio (%)** | 10 | 10 | 10 | 10 | 10 | 10 | 10 | 10 | 10 | 12.5 |
| **$F_y$, Steel (MPa)** | 400 | 400 | 400 | 400 | 400 | 400 | 400 | 400 | 400 | 400 |
| **$f_c'$, Concrete (MPa)** | 35 | 35 | 35 | 45 | 45 | 45 | 55 | 55 | 55 | 45 |
| **Longitudinal Reinforcement (%)** | 1.188 | 1.188 | 1.188 | 1.584 | 1.584 | 1.584 | 1.901 | 1.901 | 1.901 | 1.584 |
| **Longitudinal Rebar** | 30M | 30M | 30M | 30M | 30M | 30M | 30M | 30M | 30M | 30M |
| **Spiral Spacing (mm)** | 65 | 65 | 65 | 50 | 50 | 50 | 65 | 65 | 65 | 50 |
| **Transverse Reinforcement (%)** | 0.825 | 0.825 | 0.825 | 1.072 | 1.072 | 1.072 | 1.225 | 1.225 | 1.225 | 1.072 |
| **Spiral size** | 15M | 15M | 15M | 15M | 15M | 15M | 20M | 20M | 20M | 15M |

Table 3.4 Final design parameters for PBD-deficient bridge piers

| | C11 | C12 | C13 | C14 | C15 | C16 | C17 | C18 | C19 | C20 |
|---|---|---|---|---|---|---|---|---|---|---|
| **Diameter (mm)** | 1500 | 1500 | 1500 | 1500 | 1500 | 1500 | 1500 | 1500 | 1500 | 1500 |
| **Aspect Ratio** | 5 | 7 | 9 | 5 | 7 | 9 | 5 | 7 | 9 | 7 |
| **Axial Load Ratio (%)** | 10 | 10 | 10 | 10 | 10 | 10 | 10 | 10 | 10 | 12.5 |
| **$F_y$, Steel (MPa)** | 400 | 400 | 400 | 400 | 400 | 400 | 400 | 400 | 400 | 400 |
| **$f_c'$, Concrete (MPa)** | 30 | 30 | 30 | 35 | 35 | 35 | 40 | 40 | 40 | 35 |
| **Longitudinal Reinforcement (%)** | 1.188 | 1.188 | 1.188 | 1.584 | 1.584 | 1.584 | 1.901 | 1.901 | 1.901 | 1.584 |
| **Longitudinal Rebar** | 30M | 30M | 30M | 30M | 30M | 30M | 30M | 30M | 30M | 30M |
| **Spiral Spacing (mm)** | 100 | 100 | 100 | 125 | 125 | 125 | 150 | 150 | 150 | 125 |
| **Transverse Reinforcement (%)** | 0.536 | 0.536 | 0.536 | 0.429 | 0.429 | 0.429 | 0.531 | 0.531 | 0.531 | 0.429 |
| **Spiral size** | 15M | 15M | 15M | 15M | 15M | 15M | 20M | 20M | 20M | 15M |

## 3.3 Analytical model development

The seismic performance of the studied bridge piers is realized through the use of a 2D fiber based finite element modelling approach using OpenSEES (Mazzoni et al. 2006). Figure 3.3 details the fiber section implementation strategy of the pier, in which cover concrete and core concrete are modelled separately, and each individual longitudinal rebar is modelled as a single fiber.
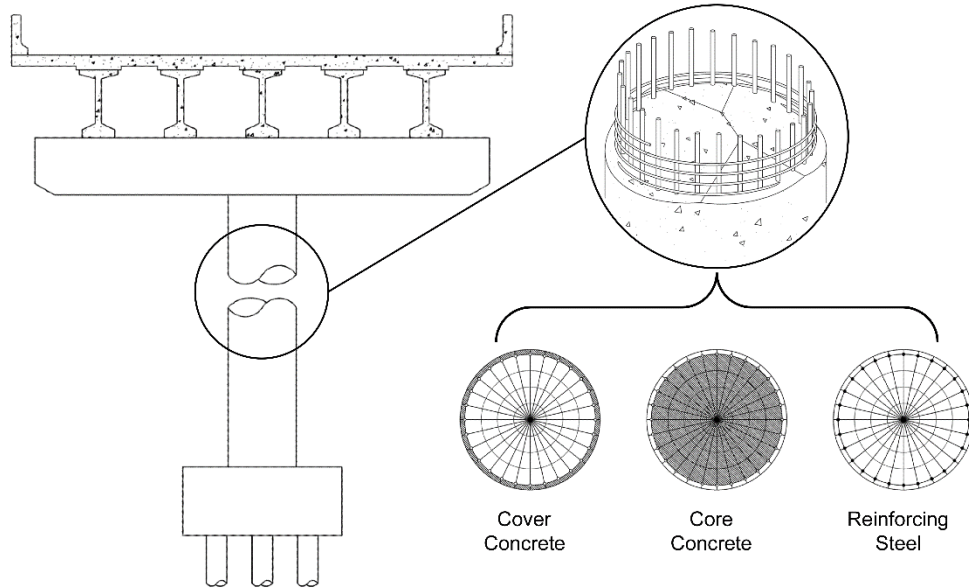
Figure 3.3 Typical single column bridge pier section and fiber discretization

Transverse reinforcement is not typically modeled explicitly in fiber-based modelling strategies. As such, confinement effects brought about by the transverse reinforcement are calculated and implemented in the core concrete material properties through confinement factors. The confined concrete formulae developed by Mander et al. (1988) are adopted herein, where the effective lateral pressure in circular columns is given in the form of:

$$f_l' = f_l k_e \tag{5}$$

Where $f_l$ is the pressure exerted by the transverse reinforcement which confines the core concrete, and $k_e$ is the confinement effectiveness coefficient. Many additional formulas which capture the confinement effects are provided in the aforementioned model (Mander et al. 1988), however, for brevity are omitted.

3.3.1 Material and section properties

Nonlinear uniaxial materials which constitute the aforementioned core, confined concrete, and reinforcing steel are applied using existing material models found in the OpenSEES material library. Reinforced concrete behavior is modeled using the 'concrete07' material model, which is based on an implementation of the original Chang and Mander concrete model (1994) with simplified unloading and reloading branches. The hysteretic rules for the concrete model have been developed based on statistical regression of previous cyclic compression experiments performed by a number of researchers. Figure 3.4 shows the material stress strain response to cyclic loading for confined concrete, concrete07 with nominal compressive strength, $f_c$' = 35 MPa. Unconfined concrete material properties for establishing the material model are calculated using the suggested values which are recommended in the OpenSEES user manual with the following equations:

$$E_c = 8200 * (f'_{c0})^{3/8} \tag{6}$$

$$f_t = 0.62 * \sqrt{f'_{c0}} \tag{7}$$

$$\varepsilon_t = \frac{2 * f_t}{E_c} \tag{8}$$

$$x_p = 2 \tag{9}$$

$$x_n = 2.3 \tag{10}$$

$$r = \frac{f'_{c0}}{5.2} - 1.9 \tag{11}$$

Where $E_c$ is the initial elastic modulus, $f_{c0}$ is the cylinder compressive strength of concrete, $f_t$ is the concrete tensile strength, $\varepsilon_t$ is the concrete strain at maximum tensile strength, $x_p$ and $x_n$ are non-dimensional terms which define the strain at which straight line descent begins in tension and compression, and $r$ is the parameter which controls the nonlinear descending branch. Similarly, confined concrete parameters are determined using the Mander et al. (1988) model, and modulus and tension properties are again calculated using equations (6),(7), and (8).
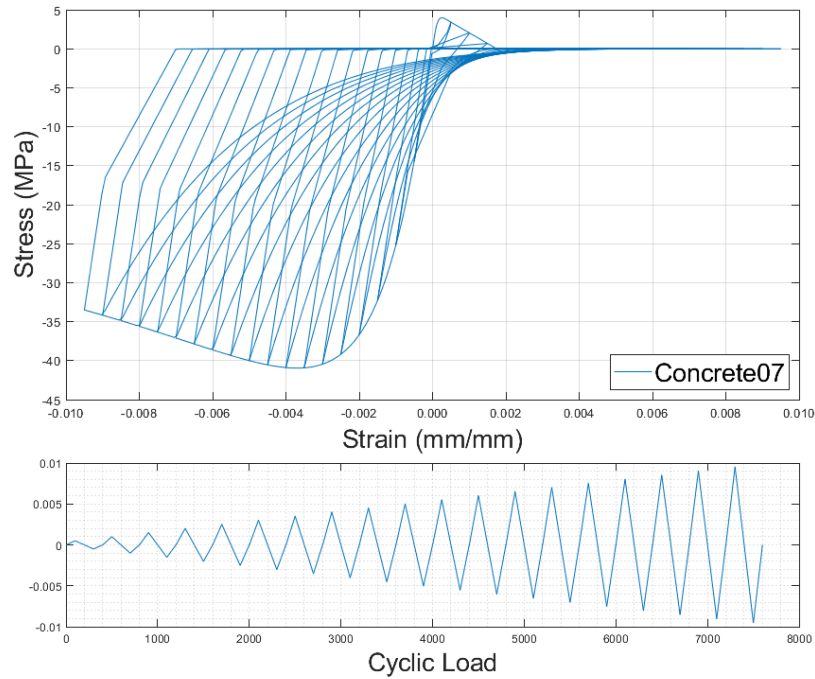
Figure 3.4 Uniaxial cyclic behaviour of implemented Concrete07 model

Reinforcing steel is modeled using the 'steel02' material provided by OpenSEES which uses the Menegotto-Pinto steel constitutive model (1973) which was later extended by Filippou et al. (1983) to include isotropic strain hardening. Furthermore, an OpenSEES material wrapper object, 'fatigue' has been merged with the steel02 model to include low-cycle fatigue based on Miner's rule linear strain accumulation which is implemented using a rainflow cycle counting algorithm. The fatigue material has the additional option to define maximum and minimum strain limits which have also been enabled and defined at $\varepsilon_s = 0.10$ to model longitudinal bar rupture.
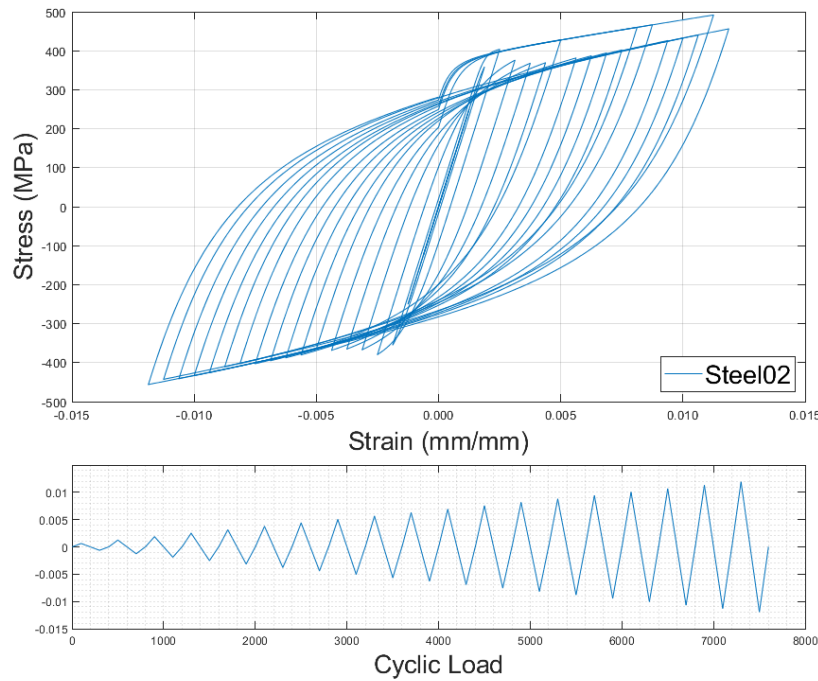
Figure 3.5 Uniaxial cyclic behaviour of implemented Steel02 model

The fiber sections are aggregated into a single material section, which is then used to model the pier in the finite element model space using a beam-column element. Currently, modelling reinforced concrete structures in OpenSEES is typically achieved through the use of fiber-based nonlinear beam column elements (BCE). Two modeling approaches exist; one which employs displacement-based beam column elements using the 'dispBeamColumn' command, and the other using force-based beam column elements via 'forceBeamColumn'. The calculation strategies used by the OpenSEES analysis object differ, and as such it is common to see a single element with 5-7 integration points being used in the case of force-based elements, and 3-5 separate elements for displacement-based BCEs to achieve comparable performance. In force-based BCEs, the predefined fiber sections are placed at discrete locations along the element dependent on the integration scheme specified, though Gauss-Lobatto is the default and most commonly used (Scott 2011). In this research, a modified force-based BCE is used through the command 'beamWithHinges' (BWH). The BWH element implementation is shown in Figure 3.6 and is comprised of two modified Gauss-Radau plastic hinge integration regions applied to the beam

32

ends at lengths of 4LpI and 4LpJ. Additionally, a distinct two-point Gauss integration region for the interior section is implemented for a total of six element integration points.
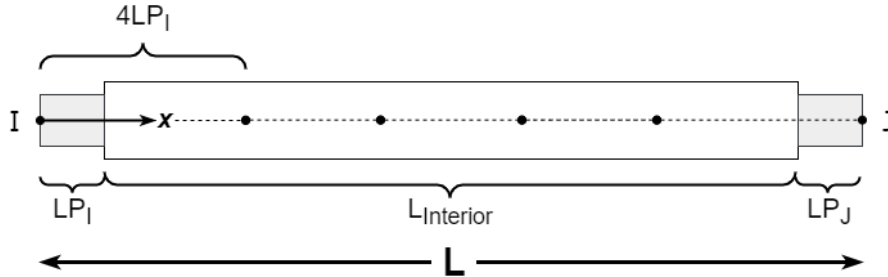


Figure 3.6 BeamWithHinges element implementation

Not only is the BWH element shown to provide more accurate moment curvature response (Scott and Fenves 2006), but there is an advantage to specifying different material section properties at the plastic hinge (PH) locations and the interior, as is the case for increased transverse reinforcement in the PH region. Plastic hinge length $L_p$ is calculated based on the equation determined by Paulay and Priestley (1992) which is approximated as:

$$L_p = 0.08L + 0.022d_b f_y \tag{12}$$

where $L$ is the length of the pier in mm, $d_b$ represents the longitudinal bar diameter, and $f_y$ is the yield strength of the rebar in MPa.

Node and element responses are obtained on-demand in OpenSEES, and in the case of fiber sections, are outputted as one fiber response per recorder. As such, the model has been programmed to output all fiber responses for the cover concrete and reinforcing fibers. Core concrete responses have been obtained from the outermost fibers only, as this is where the largest strains are to occur, and utilising the entirety of the fibers would prove to be an unnecessary

computational expense. Figure 3.7 illustrates the fiber section responses which are recorded as the shaded portions of the figure.



|  Cover  |  Core  |  Reinforcing  |
|  Concrete  |  Concrete  |  Steel  |
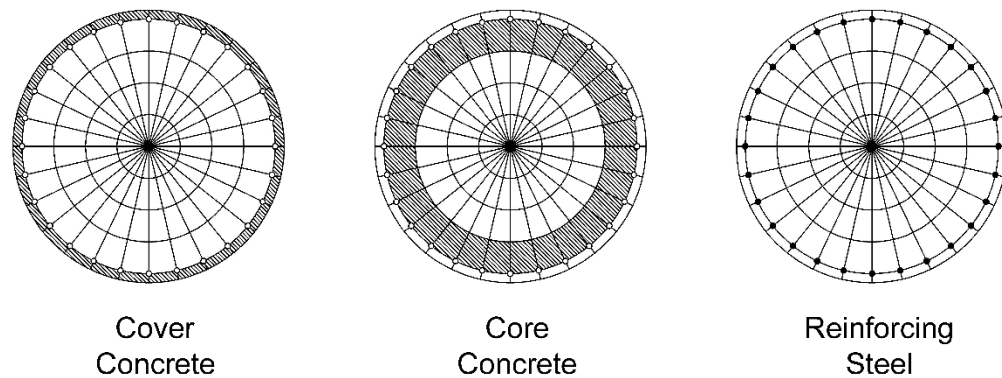
Figure 3.7 Fiber section stress-strain recorder placement

3.3.2 Validation

The developed nonlinear model exists in abstract space until its performance can be deemed accurate in simulating real world conditions. Fortunately, many research efforts from 1980-2000 focused on the performance of real bridge pier columns and have made their hysteretic responses available for validation efforts. One such study by Lehman and Moehle (2000) explored the performance of five concrete bridge columns with varying amounts of longitudinal steel and aspect ratios subjected to reversed cyclic loading. Column 415 has been selected to be modeled with the same material and geometric properties in order to validate the proposed OpenSEES model.
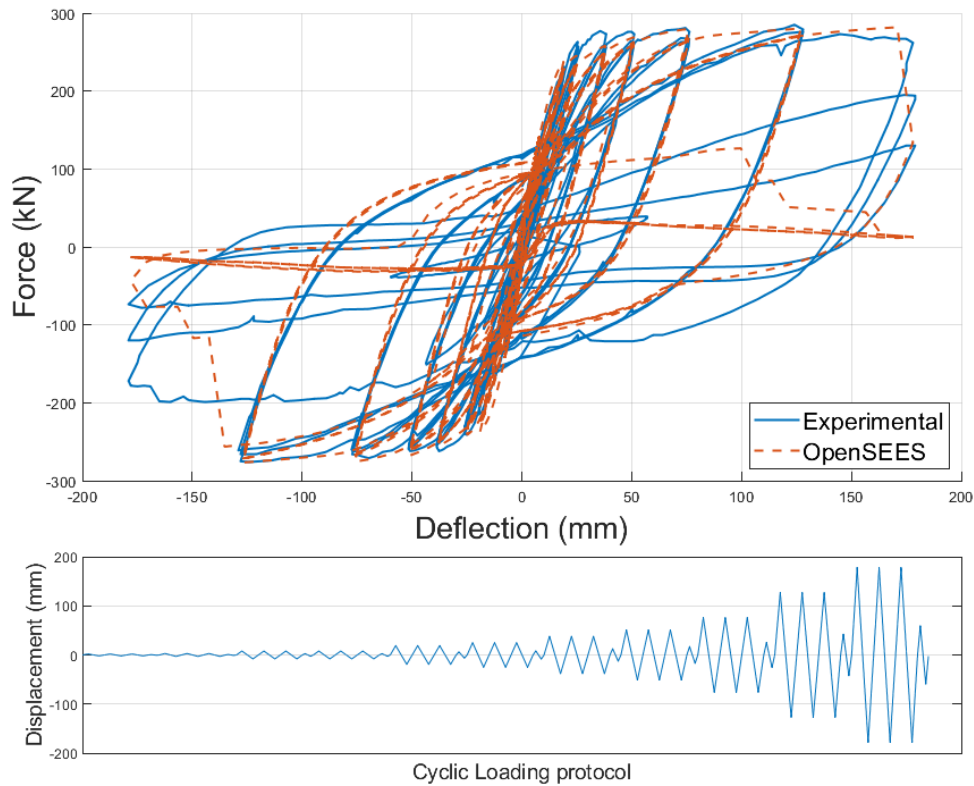
Figure 3.8 OpenSEES model column cyclic response compared to column 415 (Lehman and Moehle 2000)

From the above figure, it can be seen that the developed OpenSEES model achieves good agreement with the recorded experimental data. The developed model captures reinforced concrete hysteresis well during low displacement, and reasonably well during high energy dissipation cycles.

## 3.4  Strain-based strength degradation scheme

Strength and stiffness deterioration of materials is more difficult to capture in OpenSEES. Typically, material pinching effects are applied using one of several implementations of the Ibarra-Medina-Krawinkler Deterioration Model (2005). There are several studies which have used this model; however, it is necessary to calibrate all parameters for each configuration, which would pose a challenge for a large column test matrix. Instead, a simplified strain-based strength modification scheme is applied to the fiber elements located in the plastic hinge region of the

35

bridge pier at post-mainshock and post-aftershock column states. Recent studies which have evaluated the residual seismic capacity of post-earthquake RC column members in structures, have also assigned reduction factors which are associated with various damage levels. Di Ludovico et al. (2013) assembled and explored a database of cyclic tests of 23 flexure or flexure-shear failure dominated rectangular RC columns with deformed rebars, and 13 with smooth bars. Using the experimental data, modification factors for strength, stiffness, and residual drift were proposed for modifying the plastic hinges of RC columns which have exceeded elastic limits. Similarly, Chiu et al. (2019) performed experimental analysis of 6 column specimens, in which flexure, flexure-shear, and shear failure modes were observed and used to calibrate a residual seismic capacity model for which strength, stiffness, and energy dissipation are modified. The viability of the method was demonstrated by performing a post-earthquake assessment of a school building which was damaged during an earthquake in Taiwan.

Similarly, a reduction factor scheme is developed and suggested in this study for the sectional strength modification of concrete and reinforcing steel fibers in the bridge pier's plastic hinge region. Longitudinal steel damage levels have been proposed at five key strain damage levels as obtained from the appropriate literature. The initial damage state implemented for steel corresponding to $\varepsilon_s = 0.002$ is defined based on the commonly used 0.2% yield offset strain. Goodnight et al. (2015) performed large scale experiments of 30 bridge pier columns, where a high-fidelity 3D optical position measurement system to record column strain data was implemented. A statistical analysis of the obtained results during experimental testing correlated longitudinal rebar strain corresponding to 1mm and 2mm crack widths as $\varepsilon_s = 0.010$ and $\varepsilon_s = 0.020$ respectively. Furthermore, Goodnight et al. (2016) developed empirical formulations for bar buckling which were compared against the existing drift-based methods proposed by Berry and Eberhard (2003) and strain-based methods by Feng et al. (2015). Using the combined datasets from Goodnight et al. (2015) and Berry and Eberhard (2003) study, a modified approach for predicting bar buckling limit states was developed, and shown to produce more accurate peak tensile strain estimates when predicting bar buckling. Tensile strain corresponding to bar buckling is calculated as:

$$\varepsilon_{bb} = 0.03 + 700\rho_s \frac{f_{yh}}{E_s} - 0.1\frac{P}{f_c' A_g} \tag{13}$$

Where $\rho_s$ is the transverse volumetric steel ratio, $f_{yh}$ is the yield strain of transverse steel, $E_s$ is the corresponding transverse steel modulus of elasticity, and $P/f_c'A_g$ is the axial load ratio.

Table 3.5 Suggested reinforcing steel reduction factors

| Damage Level | Performance Criteria (rebar strain) | Damage State | Reduction Factor |
|---|---|---|---|
| 0 | *No Damage* | DS-0 | 1 |
| I | 0.002 | DS-1 | 0.8 |
| II | 0.010 | DS-2 | 0.6 |
| III | 0.020 | DS-3 | 0.4 |
| IV | $\varepsilon_{bb}$ | DS-4 | 0.2 |
| V | 0.100 | DS-5 | 0 |

Concrete material damage states have been proposed at four strain levels. The initial damage state implemented for concrete corresponding to $\varepsilon_c = 0.004$ is defined based on the serviceability concrete compression strain (Kowalsky 2000). Damage level II $\varepsilon_c = 0.006$ is adopted by S6-19 for minimal damage performance as the strain corresponds to the onset of cover concrete spalling (Priestley et al. 1996) . Furthermore, concrete core crushing strain is approximated at $\varepsilon_c = 0.015$, and ultimate concrete compressive strain is approximated using the following formula (Priestley et al. 1996)

$$\varepsilon_{cu} = 0.004 + {}^{1.4\rho_s f_{yh}\varepsilon_{su}}\big/_{f_c'} \qquad (14)$$

Where $\rho_s$ is the transverse volumetric steel ratio, $f_{yh}$ is the yield strain of transverse steel, $\varepsilon_{su}$ is the ultimate steel tensile strain, and $f_c'$ is the concrete compressive strength.

Table 3.6 Suggested reinforced concrete reduction factors

| Damage Level | Performance Criteria (concrete strain) | Damage State | Reduction Factor |
|---|---|---|---|
| 0 | No Damage | DS-0 | 1 |
| I | 0.004 | DS-1 | 0.75 |
| II | 0.006 | DS-2 | 0.50 |
| III | 0.015 | DS-3 | 0.25 |
| IV | $\varepsilon_{cu}$ | DS-4 | 0 |

Regression functions are proposed for the strength reduction parameters which are applied to the concrete and reinforcing steel fibers located in the plastic hinge region of the bridge pier. Figure 3.9 and Figure 3.10 represent the 3rd order polynomial line fitted to the damage level strains. Floating point values based on maximum concrete compressive and rebar tensile strains which are obtained from MS-only and MS+AS analysis are determined and applied to the material strength properties. Concrete compressive strength, $f_c'$ is multiplied by the reduction factor, and both confined and unconfined material properties are recalculated based on the reduced strength. Similarly, reinforcing steel $f_y$, is also multiplied by the steel reduction factor. It should be mentioned that material reduction parameters are applied to the intact properties only, i.e. 75% and 60% reduction factors determined for post-MS and post-AS states respectively are exclusively applied to the intact material properties and do not "compound" for a total reduction of 45%.
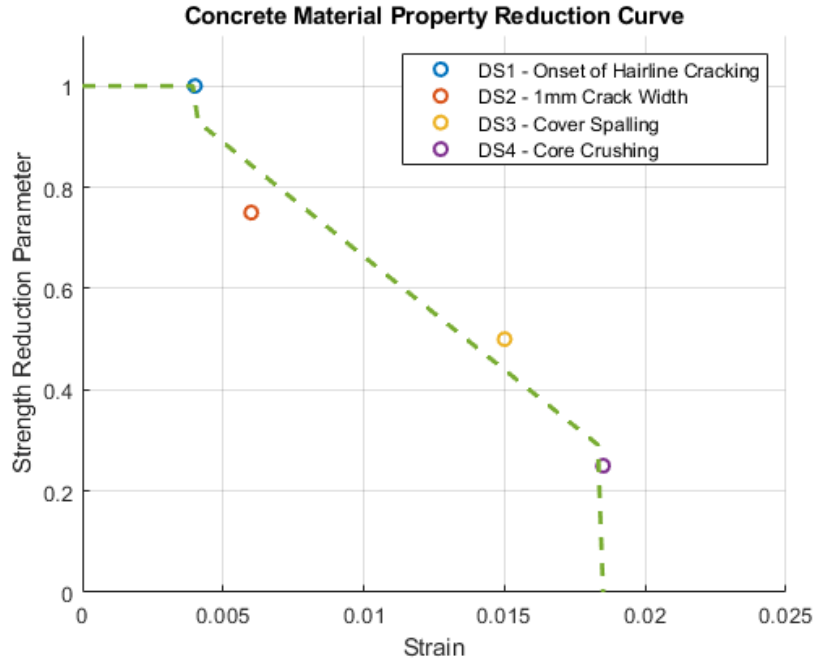
Figure 3.9 Concrete material property reduction curve
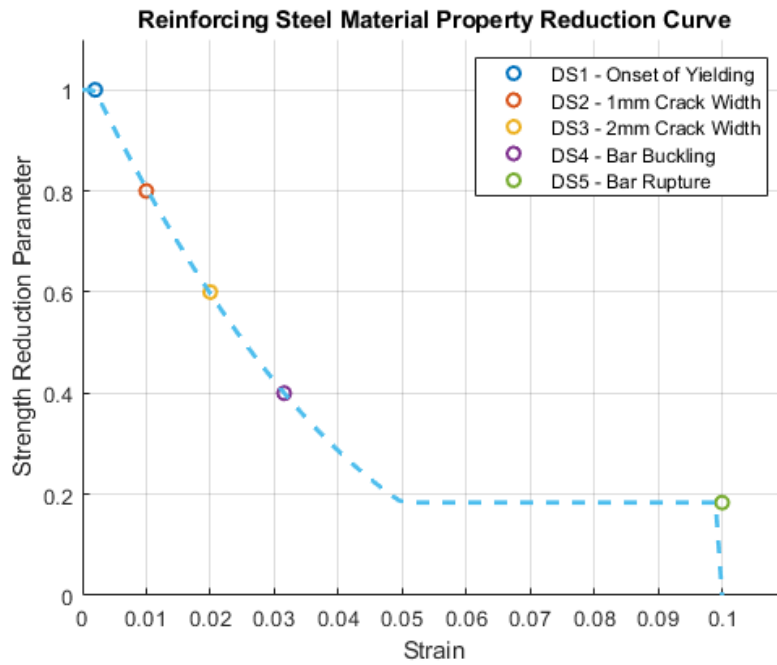


Figure 3.10 Reinforcing steel material property reduction curve

To further illustrate the effect of the material property reduction values, the individual uniaxial material models have been plotted again in Figure 3.11, for the intact and two reduced strength states. The different behaviour of the material reductions can be noticed in the figure, where the concrete strength reduction is applied to the compressive strength, $fc'$ and the remaining properties have been recalculated, resulting in the compressive envelope being shortened while the tensile strength remains relatively unchanged. In the case of the steel material, the reduction parameter is applied to the modulus of elasticity, $E_s$ which results in an envelope which is shifted and produces lower peak compressive and tensile strengths.
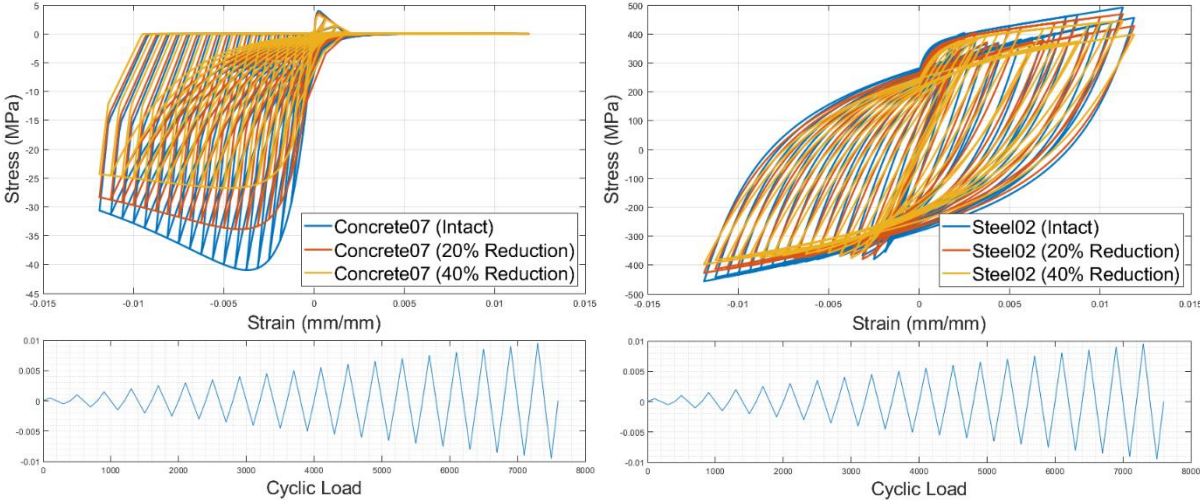


Figure 3.11 Effect of strength reduction for (a) Concrete07 and (b) Steel02 uniaxial materials

## 3.5    Ground motion suite

Mainshock-Aftershock ground motion records are selected for assessing the seismic performance of the bridge pier components of a multi-span highway bridge in Vancouver, British Columbia. Each ground motion consists of a mainshock and aftershock(s), such that the effects due to mainshock-aftershock sequences rather than conventional mainshock-only records, can be investigated using the selected records. Figure 2.2 illustrates a typical MS-AS ground motion

record. The record selection procedure is based on the multiple conditional mean spectra (CMS) (Baker 2011; Goda and Atkinson 2011), where separate target response spectra are developed for earthquakes having distinct record characteristics. For the seismicity in Vancouver, consideration of shallow crustal, deep inslab, and mega-thrust Cascadia subduction events is important because they have very different event and ground motion characteristics due to different source and path effects. The multiple CMS-based record selection can take into account such physical characteristics and their relative contributions to overall seismic hazard. To define the CMS for different earthquake types, regional seismic hazard information on dominant scenarios is required. This information is obtained from detailed probabilistic seismic hazard analysis (PSHA) for typical sites in Vancouver (Atkinson and Goda 2011).

The multiple CMS-based record selection is carried out by following the same procedures described in Tesfamariam et al. (2015) and Tesfamariam and Goda (2015). The target CMS are developed for crustal, interface, and inslab earthquakes, based on full PSHA results. The site of interest is downtown Vancouver, and its surface soil is classified as site class D. The PSHA is conducted based on the updated regional seismic hazard model by Atkinson and Goda (2011). Figure 3.12 and Figure 3.13 show the uniform hazard spectrum (UHS) and seismic deaggregation result at the return period of 475-year and 2475-year return periods, respectively. Seismic deaggregation is based on spectral acceleration at 1.0 s. To develop CMS for different earthquake types, mean record characteristics for individual earthquake types are obtained from the PSHA results.
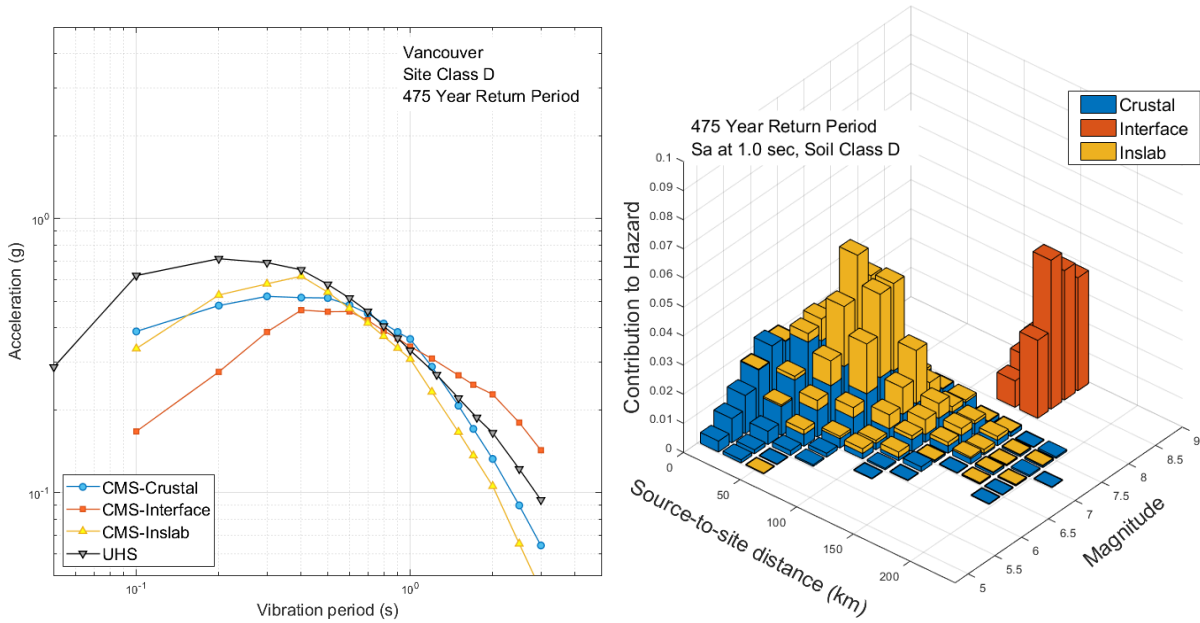
Figure 3.12 Uniform hazard spectrum and conditional mean spectra for crustal, interface, and inslab events in Vancouver (site class D; return period of 475 years), and seismic deaggregation for spectral acceleration at 1.0 s in Vancouver (site class D; return period of 475 years)
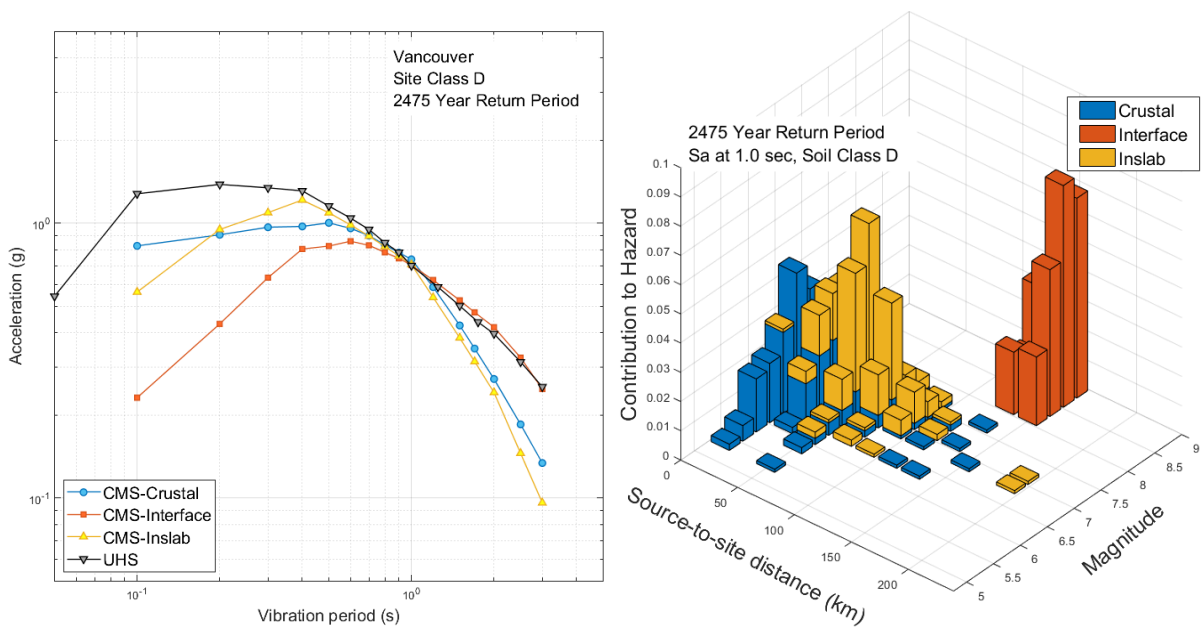


Figure 3.13 Uniform hazard spectrum and conditional mean spectra for crustal, interface, and inslab events in Vancouver (site class D; return period of 2475 years), and seismic deaggregation for spectral acceleration at 1.0 s in Vancouver (site class D; return period of 2475 years)

The record database is built from an extended dataset of real mainshock-aftershock sequences; it has been developed by combing the NGA database (Goda and Taylor, 2012) with the updated version of the KKiKSK database (Goda, 2012; Tesfamariam and Goda, 2015). The number of available mainshock-aftershock sequences is 606; among them, there are 197 crustal earthquakes, 340 interface earthquakes, and 69 inslab earthquakes. The interface events are from the 2003 Tokachi-oki earthquake and the 2011 Tohoku earthquake which have similar event characteristics as the expected Cascadia subduction earthquake.

Using the target CMS, a set of ground motion records are selected by comparing response spectra of candidate records with the target spectra. The total number of MS-AS records is set to 50 with an even distribution of earthquake type representation selected to include crustal, interface, and inslab earthquakes. Since MS-AS records are multicomponent ground motions, the response spectra is defined as the geometric mean of the two horizontal components and the target CMS is computed for the MS portion of the MS-AS sequences. The vibration period range for the spectral matching is considered from 0.5 $T_1$ to 2.0 $T_1$, which is inclusive of the major vibration periods of the bridge piers studied. Furthermore, the response spectra of the selected records and the target CMS are similar for the crustal and interface records; for inslab records, the selected records contain richer short-period spectral content than the target spectra. Given the availability of ground motion records and the size of ground motion records (i.e., 16-17 for each earthquake type), matching of the candidate response spectra with the target is deemed to be adequate.

Figure 3.14 shows the magnitude-distance distribution of the selected earthquake records where record characteristics for mainshocks and major aftershocks are included. For clarification, major aftershocks are the single largest magnitude aftershock in the case of MS-AS sequences which contain multiple aftershocks. Finally, Figure 3.15 compares duration metrics such as the duration-Arias intensity (AI) plot and the duration-cumulative absolute velocity (CAV) plot for the different earthquake types. Furthermore, Figure 3.15(b) demonstrates the long duration effects of the interface records which have larger CAV values than the crustal and inslab records.
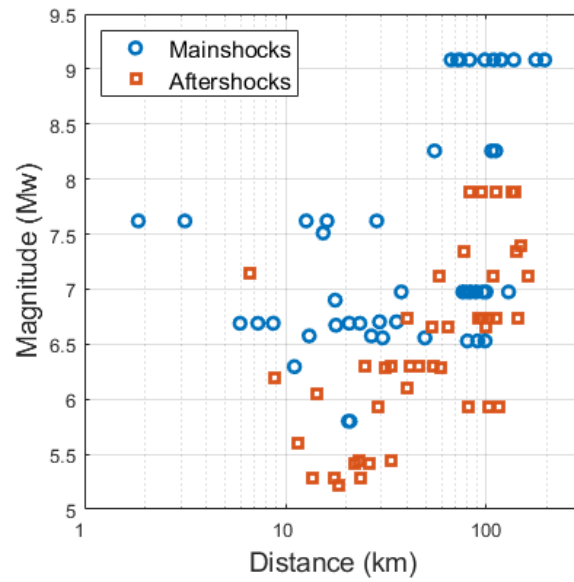
Figure 3.14 Magnitude-distance distribution of mainshocks and major aftershocks of the selected ground motion sequences.
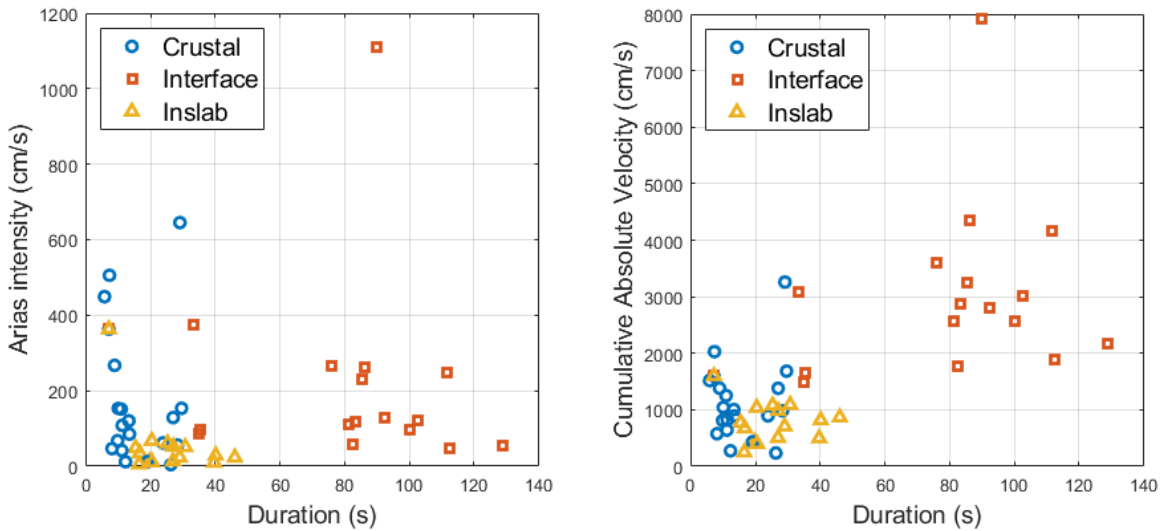


Figure 3.15 Duration-Arias intensity distribution (a) and duration-cumulative absolute velocity distribution (b) of the selected (mainshock) ground motion records.

## 3.6 Static pushover and nonlinear time history analyses

After generating the finite element models, the piers are subjected to a static analysis where the superstructure mass is gradually applied to the top of the column. A static pushover analysis in both orthogonal directions (i.e. lateral and axial) is performed for each intact column following gravity loading to establish intact pier capacity prior to any earthquake loading. Eigenvalue analysis is performed for the first mode of the column and a 5% Rayleigh damping is applied. The first nonlinear time history analysis is performed, in which the MS-only component of the selected ground motion is analysed using the Newmark average acceleration method integrator. Material reduction factors are calculated based on the outputted strains and are applied for the following post-MS pushovers to determine residual capacities. Subsequently, a second time history analysis is performed using the post-MS damaged model, where the aftershock component of the records is analysed. A final strength modification factor is determined for the post-AS damage state, and residual lateral and axial capacities are again determined.

Figure 3.16 and Figure 3.17 illustrate a sample of the post-MS and post-AS residual capacity results obtained from the axial and lateral pushover analyses, respectively. Three additional lines are plotted to demonstrate $25^{th}$, median ($50^{th}$), and $75^{th}$ percentile ranges for the residual capacities in each figure. Though the data generated here is an intermediate step in preparation for the following chapters, it is clear that the consideration of aftershocks increases the susceptibility to further damage accumulation in bridge components, as can be seen by the decrease in median residual capacity when comparing post-MS and post-AS damage states. Furthermore, the divergence of the median and $25^{th}$ percentile lines shown in the post-AS figures suggest that overall, more damage is occurring to bridge piers which remained undamaged during mainshock-only analysis. The data generated in this chapter will be further processed in chapter 4, where it will be used as outputs for the data driven machine learning models, as well as in chapter 5 where it will make the basis of the fragility analysis of the bridges.
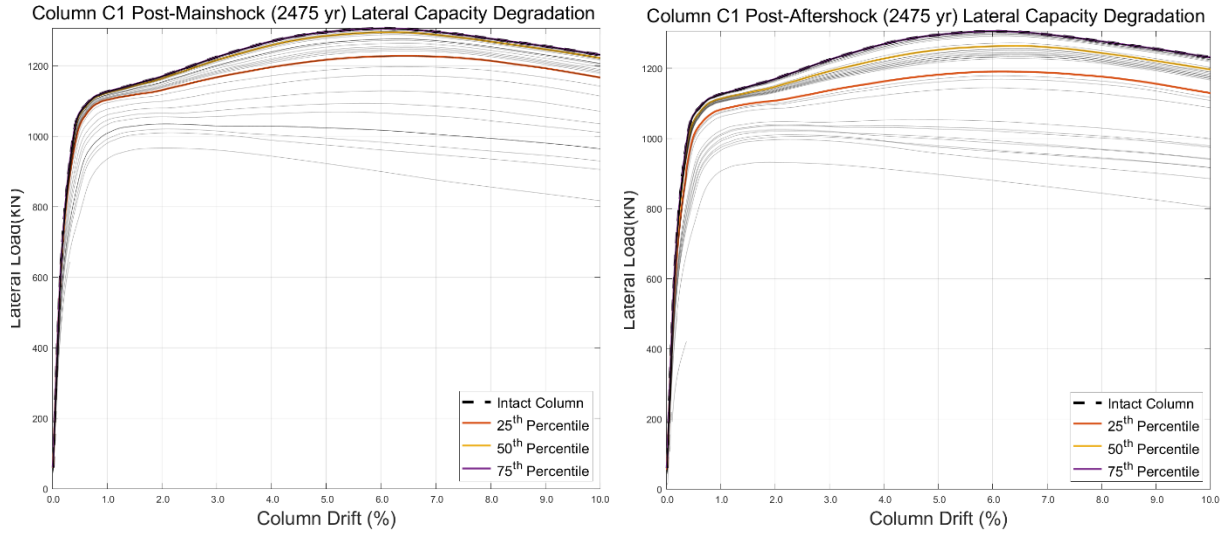
Figure 3.16 Column C1 (a) post-MS and (b) post-AS lateral capacity, analysed using 2475-year return period ground motions.
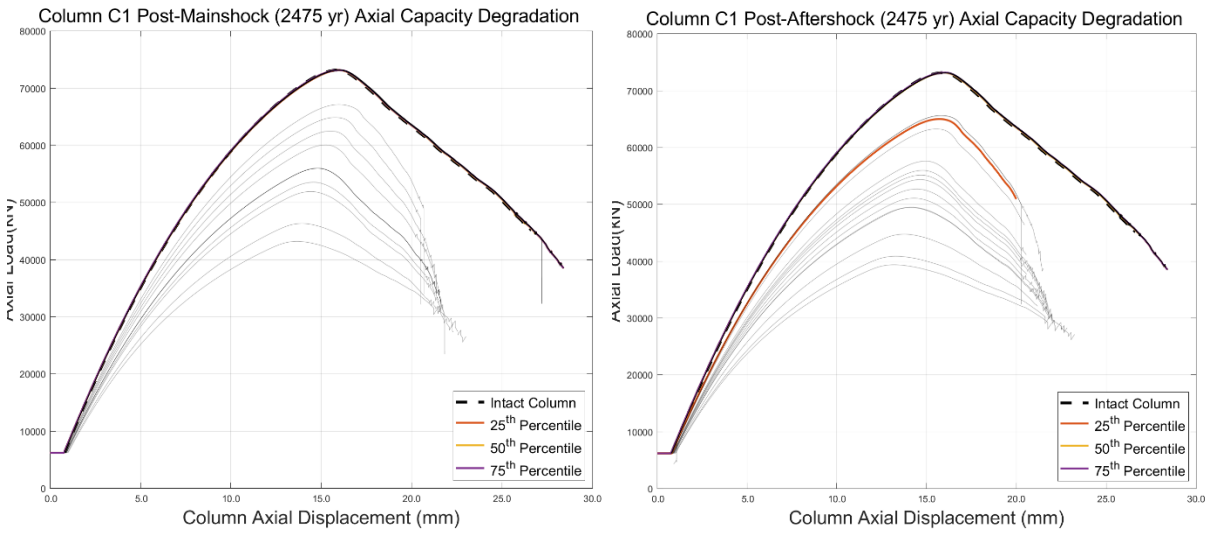


Figure 3.17 Column C1 (a) post-MS and (b) post-AS axial capacity, analysed using 2475-year return period ground motions.

## 3.7 Summary

This chapter provides design and modelling details which are employed in the modelling of the developed bridge pier test matrix in OpenSEES. An SDOF, fiber-based model is developed for each of the bridge piers, and is evaluated under MS-only and MS-AS time history. Material strains in the plastic hinge region of the column are recorded during each time history analysis and are used to generate an array of material strength reduction parameters. The post-MS and post-AS strength reductions are applied to the material models prior to the subsequent analyses. Static push over analyses are performed for the intact columns, as well as the damaged columns following MS and AS sequences in both orthogonal directions. The respective lateral and axial loading curves are collected for the evaluation of post-earthquake residual capacity for the piers, as implemented in chapter 4. The resulting strains and displacements recorded during the time history analyses serve as the IM's which are used to perform fragility analysis of the piers in chapter 5.

# Chapter 4 Post-earthquake Seismic Capacity Estimation using Machine Learning Techniques

## 4.1 General

Machine learning techniques are a promising computer science tool that can develop regression models capable of deeper understanding as compared to statistical analysis techniques which have been employed in past research. In this chapter, the geometrical and material properties, along with post earthquake capacities of the bridge pier models which were developed in the previous chapter are used in training multiple machine learning regression models. A common approach of using a train-test split is applied in this study to evaluate the performance of the proposed machine learning model against the test set data, which is representative of future user input data based on real world observations. Furthermore, a hyperparameter optimization scheme for further tuning the models is deployed alongside a 5-fold crossvalidation scheme which ensures that the models are not tuned to overfit instead. To ensure an objective comparison between the models explored, a multiple scorer reference index is assembled that captures both model accuracy and precision when assessing best model fit. The best configuration of the tuned models is then tested against a set of data which has been held out during the training portion and is evaluated again to determine a single best performing model. The proposed model allows for the rapid evaluation of a bridge pier's post earthquake capacities, and can serve as a potential tool for determining rapid bridge repair strategies following mainshock-aftershock events, or for risk mitigation over the service life of such bridges by assisting in the retrofit or structural upgrade decision making process.

## 4.2 Column database and pre-processing

The accuracy of machine learning models largely depends on the data which is used to train them. In the context of bridge piers, there are only several material and geometrical properties which accurately capture seismic performance, and are easily obtainable in the case of real-world inspection of existing infrastructure. In studies which have observed the cyclic performance of reinforced concrete columns, several parameters are often used. Berry and Eberhard (2003) studied different parameters that affect the column seismic performance limit states such as concrete spalling and longitudinal bar buckling. They investigated tie spacing ($s$), the diameter of the longitudinal reinforcing bar ($d_b$), volumetric transverse reinforcement ratio ($\rho_s$), the yield stress of the transverse reinforcement ($f_{ys}$), concrete compressive strength ($f_c{'}$), axial load ($P$), gross area of

48

the cross-section ($A_g$), longitudinal reinforcement ratio ($\rho_l$), yield stress of the longitudinal reinforcement ($f_y$), and column length ($L$) and depth ($D$) and their interaction to find out the most significant variables which affect performance limit states. Berry and Eberhard (2003) identified axial load ratio ($P/A_g fc'$) and column aspect ratio ($L/D$) as the governing parameter affecting concrete spalling and proposed a regression equation for predicting the drift at the onset of concrete spalling. For bar buckling, an effective confinement ratio ($\rho_{eff} = \rho_s f_{ys}/f_c'$) was identified as an additional factor that affects the bar buckling limit state. On the other hand, Goodnight et al. (2015) identified axial load ratio ($P/A_g fc'$), column aspect ratio ($L/D$), and expected yield strain of the transverse steel ($f_{yh}/E_s$) as the significant parameters affecting longitudinal bar buckling. For predicting column failure modes, Ma and Gong (2018) and Mangalathu and Jeon (2019) considered four input variables such as the aspect ratio, axial load ratio, longitudinal reinforcement ratio, and transverse reinforcement ratio. Based on these studies, six input parameters are considered as listed in Table 4.1, with the additional input of the MS-AS record PGA, which has been added to capture the intensity of the applied groundmotion.

Table 4.1 Statistical ranges of bridge pier column input and output parameters

| Input Parameters | Minimum | Maximum | Mean | Std. Dev |
|---|---|---|---|---|
| Axial load ratio, P/fc'Ag | 0.100 | 0.125 | 0.102 | 0.007 |
| Concrete compressive strength (MPa), fc' | 30.000 | 55.000 | 40.253 | 7.826 |
| Aspect ratio, L/D | 5.000 | 9.000 | 7.000 | 1.550 |
| Longitudinal reinforcement ratio, $\rho l$ | 1.188 | 1.901 | 1.561 | 0.277 |
| Transverse reinforcement ratio, $\rho s$ | 0.429 | 1.225 | 0.768 | 0.300 |
| Peak ground acceleration (g), PGA | 0.058 | 0.883 | 0.266 | 0.170 |
| | | | | |
| **Output Parameters** | | | | |
| Post-MS Lateral Capacity (%) | 46.28 | 100.00 | 97.57 | 4.98 |
| Post-AS Lateral Capacity (%) | 24.46 | 100.00 | 96.28 | 6.86 |
| Post-MS Axial Capacity (%) | 58.46 | 100.00 | 97.94 | 6.29 |
| Post-AS Axial Capacity (%) | 41.90 | 100.00 | 95.82 | 9.60 |

The machine learning regression methods covered in the proceeding section are to be applied to the compiled database for regression of lateral and axial residual capacities. To evaluate the performance of the proposed regression models in predicting future data, the database is divided

into a training and testing set using an 80%-20% ratio, respectively. Training and testing set assignment is shuffled using a predefined seed for repeatability, and is scaled using a MinMaxScaler to boost performance in certain models trained such as ANN and K-NN. Training data makes up the majority of the database and is used to establish all regression models, whereas the testing data is held out to evaluate the accuracy of the proposed models in predicting outputs for new data; demonstrative of the performance expected in future model fitting with new data. When deployed, 100% of the data generated from this study will instead be used for training the proposed model, and user-input data would represent testing data.

## 4.3 Machine learning regression models

The objective of this chapter is to identify the most suitable machine learning regression technique for the rapid prediction of bridge pier lateral and axial capacity degradation following a mainshock-aftershock sequence as a function of its selected input parameters. Machine learning methods explored in this study have been implemented using the Python programming language via Jupyter Notebook on a 3.30 GHz quad-core computer, achieving very fast testing execution times. As such, various regression methods such as decision trees (DT), K-nearest neighbors (KNN), support vector machines for regression (SVMR), and artificial neural networks (ANN) are explored. An overview of each regression algorithm is provided in the following section, along with the reasoning behind input parameter selection.

### 4.3.1 Linear Regression

Linear regression (LR) is the simplest and most commonly applied regression technique that generates a line of best fit through a specified set of points, in the form of:

$$y = \beta_o + \sum_{j=1}^{p} x_j \beta_j \qquad (15)$$

Where $p$ number of unknown $\beta_j$ coefficients exist for each input parameter. Coefficients $\beta_j, \beta_k, \beta_l \cdots \beta_p$ are typically estimated using the least-squares method, in which the coefficients are selected to minimize the residual sum of squares in equation (15).

$$RSS(\beta) = \sum_{i=1}^{N}\left(y_i - \beta_o - \sum_{j=1}^{p} x_{ij}\beta_j\right)^2 \tag{16}$$

4.3.2 Ridge Regression

Ridge regression (RR) is a shrinkage method that implements a size penalty on regression coefficients. Shrinkage methods retain a subset of predictors to produce a model that tends to have lower variance as compared to the least-squares estimator as discussed previously. Ridge regression penalizes the residual sum of squares as

$$\hat{\beta}^{ridge} = \underset{\beta}{argmin}\left\{\sum_{i=1}^{N}\left(y_i - \beta_0 - \sum_{j=1}^{p} x_{ij}\beta_{ij}\right)^2 + \alpha \sum_{j=1}^{p}\beta_j^2\right\} \tag{17}$$

Where $\alpha$ is the nonzero complexity parameter that controls the amount of shrinkage. A larger $\alpha$ corresponds to a greater amount of model shrinkage and thus the models become more resistant to collinearity. $\alpha$ values ranging from $10^{-6}$ to $10^6$ have been explored for model hyperparameter tuning. Typically, a size constraint $t$ for inputs is also implemented in ridge regression, and coefficients are scaled respectively such that

$$\sum_{j=1}^{p}\beta_j^2 \leq t \tag{18}$$

Imposing a size constraint alleviates a problem of high variance in the correlation variables, however, the inputs also need to be standardized in order to ensure that solutions are equivariant.

4.3.3 Lasso Regression

Lasso regression is another shrinkage method that implements size penalties on regression coefficients, sharing many similarities to the aforementioned ridge regression model. Lasso regression also penalizes the residual sum of squares, instead producing nonlinear solutions in the $y_i$ as

$$\hat{\beta}^{lasso} = \underset{\beta}{argmin} \left\{ \frac{1}{2} \sum_{i=1}^{N} \left( y_i - \beta_0 - \sum_{j=1}^{p} x_{ij}\beta_{ij} \right)^2 + \alpha \sum_{j=1}^{p} |\beta_j| \right\} \qquad (19)$$

$$subject\ to \quad \sum_{j=1}^{p} |\beta_j| \leq t \qquad (20)$$

Where $\alpha$ is the nonzero complexity parameter that instead translates each coefficient via soft thresholding. Again, $\alpha$ values ranging from $10^{-6}$ to $10^{6}$ have been explored for model hyperparameter tuning.

4.3.4 K-Nearest Neighbors Regression

K-nearest neighbors regression (KNN) is a nonparametric method that predicts a numerical target based on a distance function to its K-nearest neighbors. In this study's defined search space, the KNN makes use of an automatic search algorithm that tests both k-d tree and ball tree search within the multidimensional search space. Both search algorithms are aimed at computational efficiency in the sphere of tree search algorithms where k-dimensional trees are less computationally intensive as compared to ball tree structures, albeit with lower data structure efficiency in high dimensional searches. For the predicted data $x_i$, the KNN identifies $k$ number of neighbors from its training data which are closest to $x_i$. Using the following Euclidian distance function, a weighting factor is calculated to generate the prediction:

$$D = \sqrt{\sum_{i=1}^{k} (x_i - y_i)^2} \qquad (21)$$

The choice of K has a great influence on the performance of the KNN model. Lower K values limit model bias and allow for higher variance, whereas high K values limit model variance and allow for higher bias. In this study, $k$ values ranging from 2 to 25 have been searched to determine optimal tuning.

4.3.5 Decision Tree Regression

Decision trees are another nonparametric regression method that operates by forming a tree-like network by learning simple decision rules inferred from the data features. In this study, a nonlinear

relationship between predictors and response warrants the use of the classification and regression trees (CART) algorithm by the decision tree regressor. The decision tree algorithm works to recursively split an input space into a number of partitions, while minimizing the impurity of current partitions and those ahead. Trees are initiated with a root node and using greedy splitting with binary operators, interior and terminal nodes are formed where each internal node has only one parent and two children, and each terminal node has one parent only. The decision tree regressor is terminated when all nodes are generated, covering all features, or reaching minimum node impurity decrease thresholds. Additionally, a max depth of the tree can be specified as a stopping or tuning parameter, though it is typically left infinite by default. Tree depths between 1 and 10 as well as infinite have been searched in this study. Figure 4.1 illustrates the architecture of a generated tree structure.
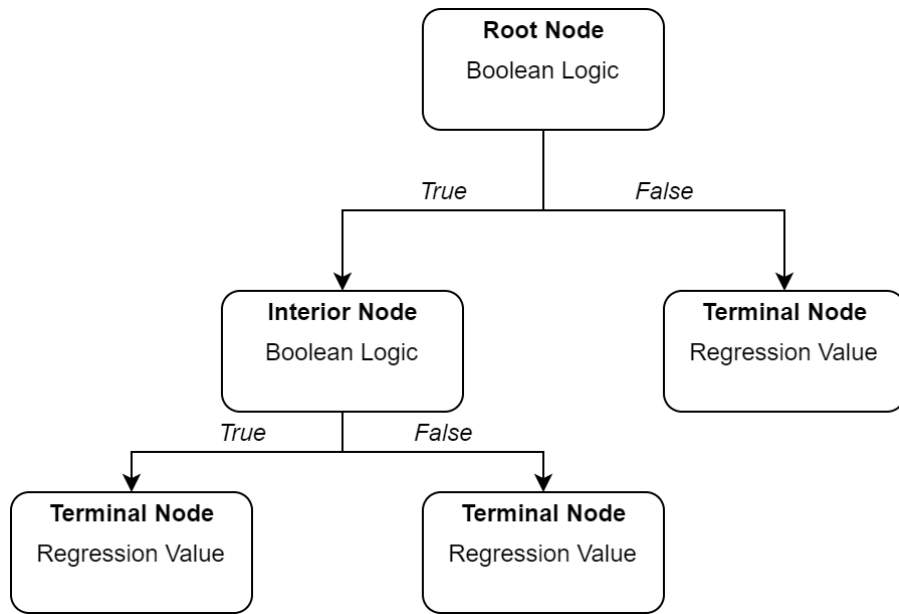


Figure 4.1 Decision tree layout for residual earthquake capacity predictions

4.3.6 Random Forest Regression

Random forest (RF) is an ensemble method that creates multiple parallel tree structures consisting of decision trees (Breiman 2001). RF implements bootstrap aggregation (bagging) and random feature selection which generates each tree using the bootstrap sampled versions of the training data. The regression model generated is the averaged regressor of each decision tree subassembly.

Random forests make for a powerful regression model since the relatively low bias of decision trees is maintained, while a common problem in decision trees, noise is reduced by averaging. A generalized random forests algorithm consists of the following procedure:

For $b = 1\ to\ B$

- Select a bootstrap sample $Z^*$ from all available training data used to build each tree.
- Grow a decision tree $T_b$ from each bootstrap sample data, by randomly selecting a portion $(m)$ of the variables from all available variables $(p)$ $(\frac{p}{3}$ is recommended) and selecting the best split among the data until the minimum node size is reached.
- Output the forest ensemble $\{T_b\}_1^B$

Predictions for $x$ are then generated in the form of

$$\hat{f}_{rf}^B(x) = \frac{1}{B} \sum_{b=1}^{B} T_b(x) \tag{22}$$

Hyperparameter tuning for the random forests regressor in this study has been carried out by searching max number of samples $(m)$ between 2 and 5, and number of trees in each forest between 50 and 1000, in increments of 50.

4.3.7 Support Vector Machines for Regression

Support Vector Machines, while typically employed for the purpose of machine learning classification, are also able to perform regression when supplied training vectors $x_i$, where $i = 1, ..., n$ and test vectors $y_i$, each corresponding to an n-dimensional vector. Support Vector Machines for Regression (SVMR) operates by generating a hyperplane within the feature space which optimally separates two classes of data to minimize the primal problem in the following equation (23).

$$\min \frac{1}{2} w^T w + C \sum_{i=1}^{n} (\zeta_i + \zeta_i^*) \tag{23}$$

$$\text{subject to} \quad \begin{aligned} y_i - w^T\phi(x_i) - b &\leq \varepsilon + \zeta_i, \\ w^T\phi(x_i) + b - y_i &\leq \varepsilon + \zeta_i^*, \\ \zeta_i, \zeta_i^* &\geq 0, i = 1, \ldots, n \end{aligned} \quad (24)$$

In C-ε SVMR such as the one employed in this research, an ε-tube surrounds the generated hyperplane in which occurring samples do not penalize the model; as slack variables $\zeta_i, \zeta_i^*$ are implemented to minimize $w^T w$ corresponding to positive and negative deviation of the predicted values. The cost function, C is used to control the amount of misclassification possible, leading to a trade-off between model error and model complexity. SVMR hyperplanes are typically generated using a linear function $\phi(x_i)$; however, other functions such as polynomial, sigmoidal, and radial basis functions (RBF) are also available and have been explored in this research. In computing, the minimization function is transformed into a dual problem which is then able to be solved using quadratic programming. The resulting solution allows for predictions in the form of:

$$\sum_{i \in SV} (\alpha_i - \alpha_i^*)K(x_i, x) + b \quad (25)$$

where $K(x_i, x)$ is the kernel function and $b$ is model bias. Several kernel function tuning parameters such as linear, polynomial (with degrees of 3, 4, and 5), radial basis function, and sigmoidal for this regressor have been searched. In addition, C values ranging from 1 to 10 and 50 to 1000 (in increments of 50), as well as ε values ranging from $10^{-6}$ to $10^{6}$ have been explored

4.3.8 Artificial Neural Network

Artificial neural networks are a type of nonlinear regression model which operate by emulating the function of neurons found in biology. Typical multilayer perceptron (MLP) (Haykin and Haykin 2009; Sarle 1994) neural networks are composed of an input layer, several hidden layers, and a single output layer. Hidden layers used are comprised of neurons that feed forward to the next layer using a weighting function. Each neuron in a hidden layer has the following output signal:

$$y_k = \varphi\left[\sum_{j=1}^{m} w_{kj}x_j + b_k\right] \quad (26)$$

In which $\varphi$ is the neuron's activation function; m is the number of neurons in the hidden layer; $w_{kj}$ are the synaptic weights; $x_j$ are the input signals; and $b_k$ is the hidden neuron bias.

Three types of regression activation functions are explored in this chapter such as the sigmoid, hyperbolic tangent (tanh), and rectified linear unit (ReLU). Sigmoid and hyperbolic tangent functions are commonly used in single layer neural networks, however suffer from problems such as exploding or vanishing gradients in deeper networks. On the other hand, rectified linear functions lend themselves particularly well to better performance in deep learning network architectures (Glorot et al. 2011).

$$\varphi_{sigmoid}(v) = 1/(1 + e^{-v}) \tag{27}$$

$$\varphi_{ReLU}(v) = max\ (0, v) \tag{28}$$

$$\varphi_{tanh}(v) = tanh\ (v) \tag{29}$$

Neural network configurations consisting of 1, 2 and 3 hidden layers, each with varying numbers of neurons ranging from 8 to 128 in increments of 8 have been explored using grid search for all three activation functions. For brevity, the three hidden layer tanh feedforward MLP with 128, 80, and 80 neurons respectively which was shown to be the best configuration for ANN regression in this study has been visualized in Figure 4.2.
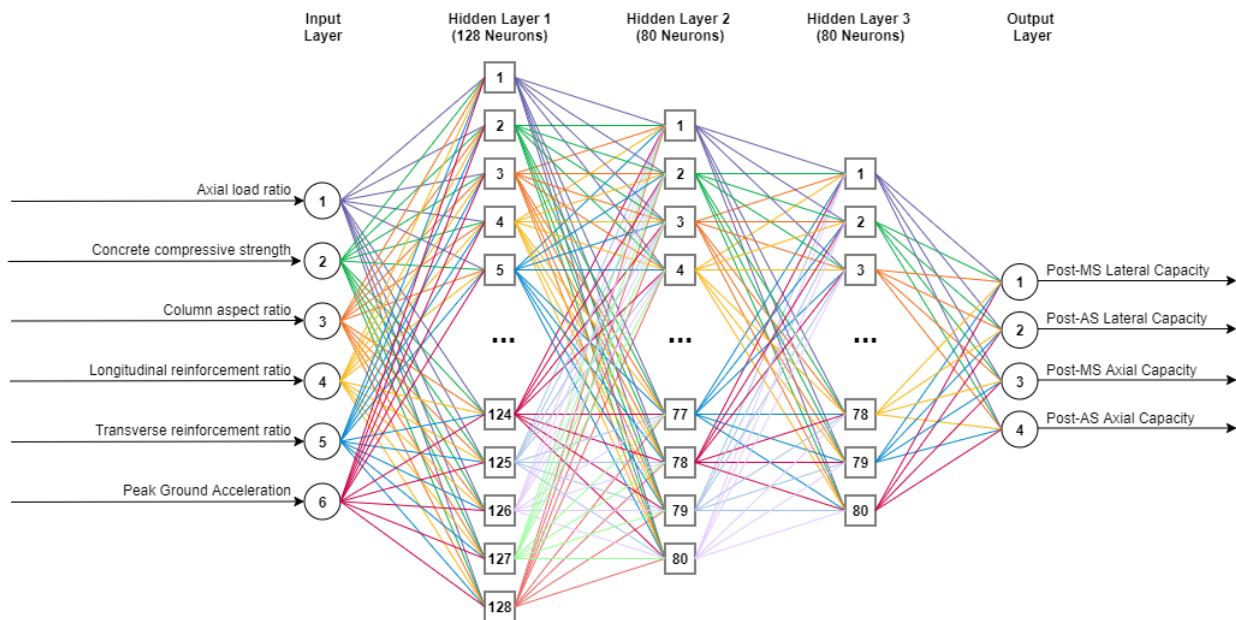


Figure 4.2 Artificial neural network layout for residual earthquake capacity predictions

4.3.9 Additional Regression Methods

It is important to mention that due to the nature of machine learning models, variations which operate on similar fundamentals or with additional modifications are available to perform similar regression as the research in this chapter. Furthermore, it is worth noting that as machine learning continues to gain in popularity, more approaches are developed and made available. Consequently, this study has chosen the canonical variations of each of the aforementioned methods as they sufficiently cover all fundamental types of available ML regression methods, lend themselves to ease of access and have the ability to be published open source.

## 4.4    Grid Search Algorithm for Hyperparameter Optimization

There exist parameters in various models which affect the overall performance of the predictions generated. While it is possible to use default, recommended, or arbitrary values, there is more performance to be discovered by tuning these hyperparameters. Grid search algorithm (GSA) has been implemented to test a wide array of hyperparameters for the majority of the previously mentioned ML models such as RR, Lasso, K-NN, DT, RF, ANN and SVMR. The parameter spaces considered for the exhaustive search have been specified in the previous sections which detail each of the methods. Predictor performance for the selection of a single best configuration of tuning parameters is assessed by four commonly used metrics which are indicators of a model's accuracy and precision, including Pearson's r correlation coefficient, coefficient of determination ($R^2$), symmetrical mean absolute percentage error (SMAPE), and root mean squared error (RMSE). The definitions for each of the metrics is as follows:

$$Pearson's\ r = \frac{\sum_{i=1}^{n}(Y'_i - \bar{Y'})(Y_i - \bar{Y})}{\sqrt{\sum_{i=1}^{n}(Y'_i - \bar{Y'})}\sqrt{\sum_{i=1}^{n}(Y_i - \bar{Y})}} \tag{30}$$

Where $Y'$ is the actual value and $Y$ is the corresponding prediction, and $\bar{Y'}, \bar{Y}$ are their average values, respectively. Pearson's r coefficient is a measure of the statistical relationship between two continuous variables, where values range between -1 and 1, where higher values closer to 1 signify a perfect linear correlation between the two variables. Furthermore, values which range between $0.5 - 1.0$ are said to have a strong statistical significance.

$$R^2 = 1 - \frac{\sum_i (Y_i - Y')^2}{\sum_i (Y_i - \bar{Y})^2} \tag{31}$$

Where again $Y'$ is the actual testing set result and $Y$ is the corresponding regression model prediction. The coefficient of determination quantifies model goodness-of-fit based on the sum of squares method, where values closer to 1 translate to higher performance, and values below 0 signify performance that is objectively worse than fitting the values to a horizontal line.

$$SMAPE = \frac{100\%}{n} \sum_{i=1}^{n} \frac{|Y_i - Y'_i|}{(|Y_i| + |Y'_i|/2)} \tag{32}$$

$$RMSE = \sqrt{\frac{1}{n} \sum_{i=1}^{n} (Y'_i - Y_i)^2} \tag{33}$$

Where $Y'$ is the actual testing set result and $Y$ is the corresponding regression model prediction. In these metrics percent model error and model deviation are quantified respectively, and as such better performing models will see lower error values.

## 4.5 Model cross-validation, testing, and hyperparameter tuning

One of the pitfalls which can be encountered with machine learning models is the overfitting of data to suggest extreme accuracies that in reality are not plausible when external data is input. A systemic approach is needed throughout model development in order to select the top performing model across multiple metrics and scenarios. Consequently, 5-fold cross-validation is performed during hyperparameter tuning where the training data is split into 5 partitions and the same configuration is trained 5 times wherein each iteration uses a different 4 of the folds to train the particular model configuration against the remaining fold; averaging the results from each of the five folds at the end. This technique of sub-sampling is employed to reduce the unwanted bias that tuning models evaluated to the final testing set would introduce. To evaluate the tuning configuration's performance using a single metric, the scorers for each configuration are normalized by ascending or descending order in favour of better performance, and a weighting scheme of 10% Pearson's r, 30% Coefficient of Determination, 30% SMAPE, and 30% RMSE is employed to define a single reference index. Models with favourable predictive capabilities are quantified by a high goodness of fit, by way of Pearson r and $R^2$ values, and minimal error as

characterized by low model variance, displayed by SMAPE and RMSE. Table 4.2 presents the results of the grid search hyperparameter tuning in which the top performing configuration amongst all crossvalidation folds have been summarized, as the configurations presented are the top performers, the reference indices have been omitted.

Table 4.2 Crossvalidation hyperparameter configurations for proposed ML models

| Model | Optimal configuration | Average Pearson's r | Average $R^2$ | Average SMAPE | Average RMSE |
|---|---|---|---|---|---|
| Linear Regression | *N/A* | *0.425* | *0.179* | *5.598* | *0.088* |
| Ridge Regression | *α = 10* | *0.428* | *0.181* | *5.557* | *0.088* |
| Lasso Regression | *α = 0.001* | *0.430* | *0.181* | *5.504* | *0.088* |
| K-Nearest Neighbours | *K = 25* | *0.591* | *0.291* | *4.790* | *0.084* |
| Decision Trees | *Depth = 7* | *0.774* | *0.539* | *3.563* | *0.062* |
| Random Forests | *m = 5, trees = 250* | *0.442* | *0.151* | *5.740* | *0.089* |
| Support Vector | *$f_x$ = RBF, C = 1, ε = 0.010* | *0.461* | *0.167* | *4.464* | *0.089* |
| Neural Network | *$H_1$ = 128, $H_2$ = 80, $H_3$ = 80, $f_x$ = tanh* | *0.554* | *0.301* | *6.015* | *0.094* |

The performance metrics of all 5 folds which are evaluated during the grid search tuning phase of the models are averaged using equal weights to produce the above values. The advantage of this approach needs again be mentioned as finding an optimal model configuration which proves its accuracy and consistency over 5 separate folds is preferred; since recommending a model which 'got lucky' during a single fold of testing is often ill-advised. Table 4.2 does not show the comparative reference index of the selected models amongst each other, as the goal of the GSA tuning phase is to determine the best performing configuration for each model. However, it is made clear that there is a divide in model performance which can easily be illustrated by the polar graph in Figure 4.3. By normalizing Pearson's *r* and $R^2$ (higher = better) and inverse normalizing *SMAPE* and *RMSE* (lower = better) values, it is evident that during crossvalidation the decision trees model fitted validation training data to test data splits with the highest accuracy and lowest variance as compared to the other models tested.
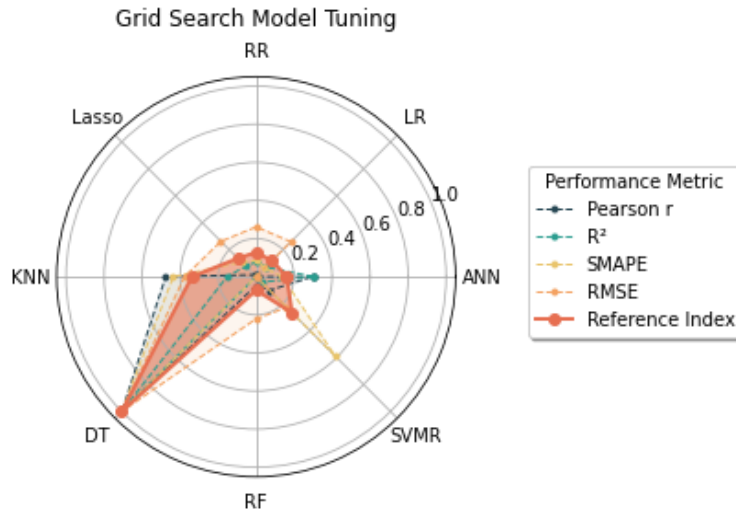
Figure 4.3 Crossvalidation reference index of optimally tuned models

## 4.6 Optimal model selection and performance

A final comparison between the testing data and the machine learning predictions generated by the best tuned models' results is presented in Figure 4.4, where the vertical distance of a point from the red 1:1 line is the error of the specific prediction made by the proposed model and a linear trendline is fitted for each model's predictions. Note that the linear trendline does not represent the function of the regressors, however is instead displayed to generalize the predictive capability of the models given new data from the testing split. As a whole, the predictions generated by the decision trees model show the least variance for all four outputs, and have trendlines which are closest to the 1:1 line. Based on this, the DT models are expected to generate predictions for each of the residual capacity outputs which perform very well, albeit would tend to overestimate residual capacity based on the vertical position of the trendline being above the 1:1 line. In the case of comparing residual lateral to residual axial capacity outputs, it is expected that the predictions generated for the axial capacity will be more accurate, as subplots (c) and (d) in Figure 4.4 tend to have much larger variance, especially in instances of undamaged bridge piers. Furthermore, the advantages of the more complex ML models such as DT, ANN, KNN and SVMR over the simpler models such as LR, RR, and Lasso are demonstrated by Figure 4.4 wherein, the complex models rarely suggest residual capacities over 100%
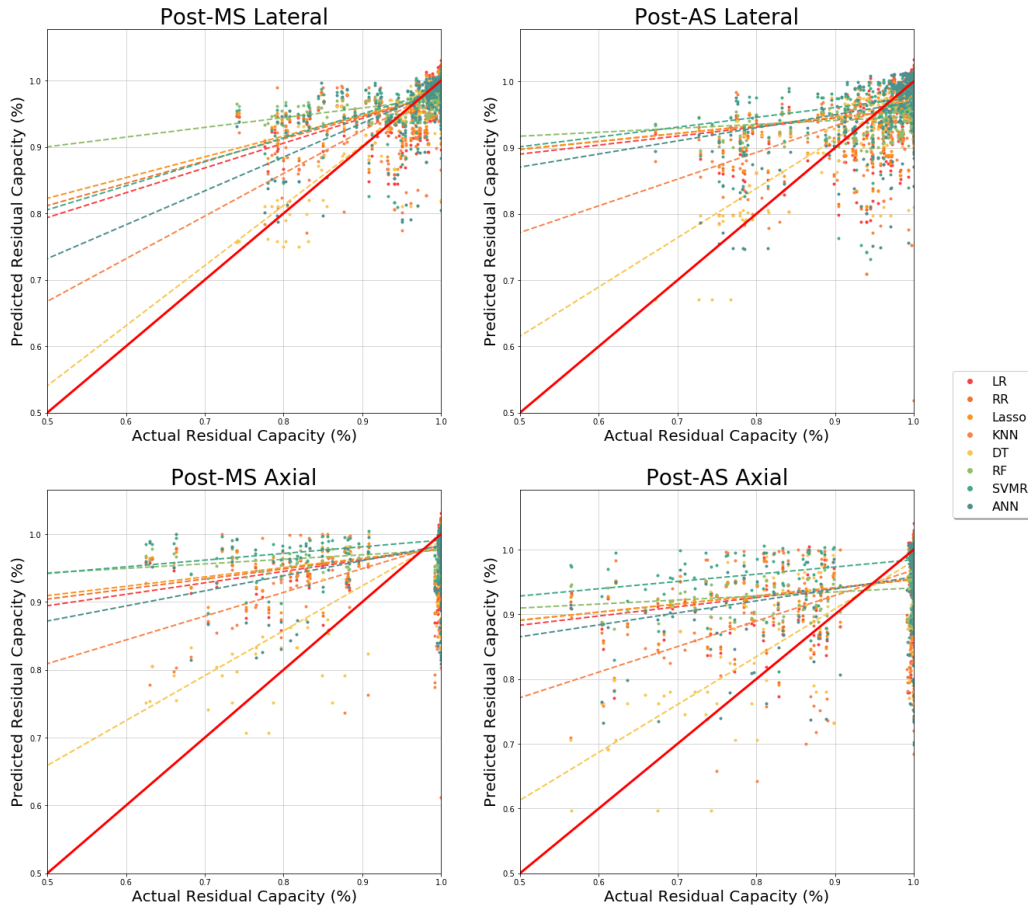
Figure 4.4 Results of training and testing of proposed ML models

The reference index metric is again applied to the models during the testing phase, where this time, model performance is normalized in order to compare performance amongst each type of model being explored. The performance of the predictive capabilities of the models as compared to the withheld test set are summarized in Table 4.3, and an additional set of polar graphs is presented in Figure 4.5, where the model metrics are recalculated for each individual output scenario. The same divide which was observed during the hyperparameter tuning is apparent in the testing set results once more, where the performance of the decision tree regressor is significantly improved as compared to the other models. The resulting metrics for the decision tree regressor describe a model which has both the highest overall accuracy as well as precision. A Pearson's r correlation coefficient above 0.70 is typically deemed to represent data which has high statistical significance; and similarly, a coefficient of determination which is near 0.75 demonstrates a strong goodness-

of-fit, especially when compared to the relative scores of the other models considered. Moreover, the SMAPE and RMSE values which indicate an ML model's residual error are also the lowest of those compared, which suggests the proposed model is highly suitable for the purpose of this residual strength prediction as it is overall very robust.

Table 4.3 Performance metrics of proposed ML models' predictive capabilities as compared to test set data

| Model | Pearson r | $R^2$ | SMAPE | RMSE | Reference Index |
|---|---|---|---|---|---|
| LR | 0.403 | 0.153 | 6.002 | 0.091 | 0.073 |
| RR | 0.403 | 0.162 | 5.935 | 0.091 | 0.085 |
| Lasso | 0.405 | 0.166 | 5.873 | 0.091 | 0.094 |
| K-NN | 0.575 | 0.277 | 4.896 | 0.083 | 0.331 |
| DT | 0.864 | 0.736 | 3.284 | 0.048 | 1.000 |
| RF | 0.400 | 0.121 | 6.464 | 0.093 | 0.000 |
| SVMR | 0.406 | 0.146 | 4.946 | 0.092 | 0.164 |
| ANN | 0.439 | 0.179 | 5.201 | 0.090 | 0.175 |

The predicted test set outputs are separated and illustrated in four individual polar graphs summarizing performance in post-MS and post-AS lateral and axial residual capacities, respectively. The differences in model capability can be seen through the distribution of performance metrics in Figure 4.5. It can be generalized that DT, ANN, and SVMR regressors bring forth the best individual performance, with a distinction in DT greatly outperforming all models in both post-MS states, whereas the distribution of model efficiency is shifted towards ANN and SVMR in the lateral and axial post-AS states. While specifying four separate models for each predicted limit state is possible, it is not recommended and is not pursued in this study. Instead, the figure serves to demonstrate the relative variance in the performance of each model for each of the outputs. The further that the reference index is divided, the more obscured the data becomes as since it is normalized amongst each output in the case of this figure, the performance improvement among each model displayed is only relative and could be insignificant when compared as a whole.
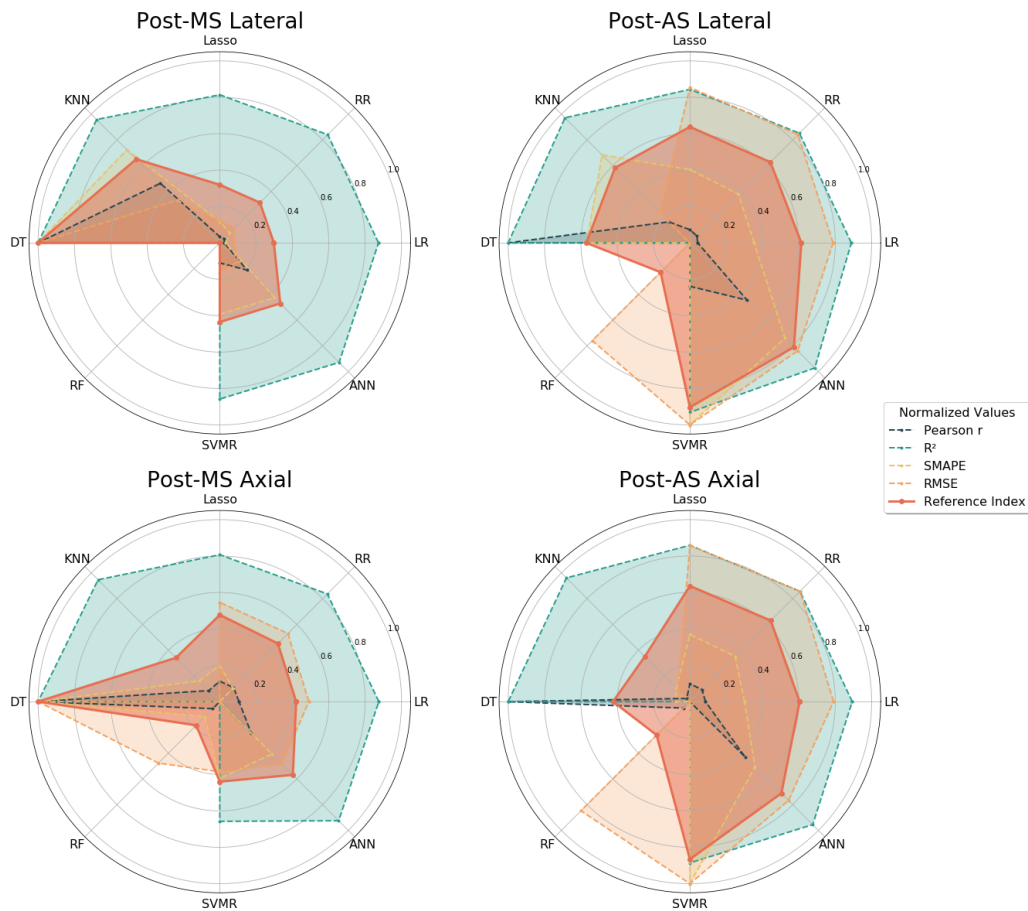
Figure 4.5 Individual performance metrics of proposed ML models' predictive capabilities as compared to test set data

## 4.7  Influence of parameter inputs

Since several variables are utilized as features in this study, it is advantageous to determine which features are influential in accurately predicting the post-earthquake lateral and axial load capacities of bridge piers. In addition to determining the best performing ML model, the importance of the input parameters has also been evaluated using the inbuilt scorer for feature importance. Feature importance describes a technique in which scores are assigned to input variables which specify the relative importance of each input when predictions are made. Figure 4.6 sorts and displays the feature importance of the selected decision tree regressor's model inputs. Earthquake intensity, followed by pier aspect ratio and axial load ratio are identified as being the dominant features which affect seismic performance. This is to be expected as the aspect ratio determines the column length, and load ratio represents superstructure mass, all of which greatly influence how an

63

idealized bridge pier is expected to behave under dynamic loading. Previous research studies on bridge damage assessment using ML techniques (Mangalathu et al. 2019a) also concluded that the intensity of ground motion is the most sensitive parameter for the damage evaluation of bridges. However, the conclusion by Mangalathu et al. (2019) was based on damage classification of bridges not on evaluation of a bridge pier's post-earthquake capacities.
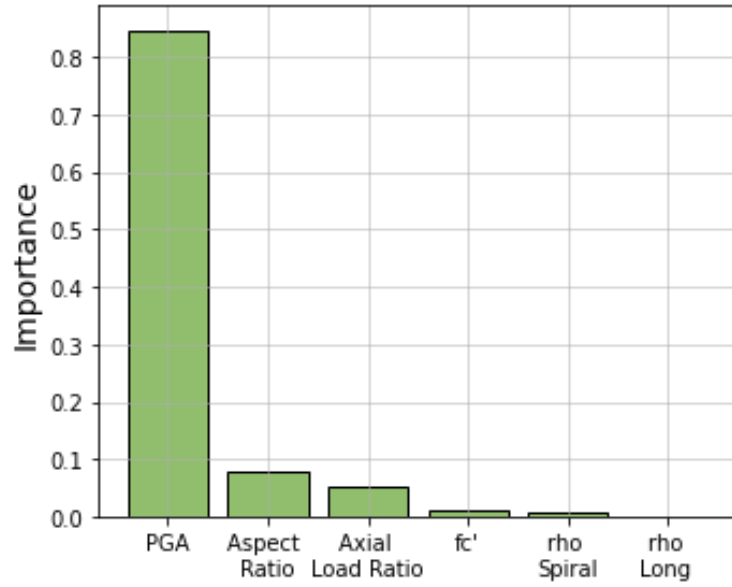


Figure 4.6 Relative importance factors for model input features

4.7.1 SHAP implementation for input feature explanation

Shapley additive explanations (SHAP) is a method which employs a coalitional game theory approach to explain the output of a machine learning model. In additive feature attribution methods, the explanation models, *g(z')* are represented using a linear function of binary input variables in the form of:

$$f(x) = g(z') = \Phi_0 + \sum_{i=1}^{M} \Phi_i z_i' \tag{34}$$

Where $f(x)$ is the original output of the ML model, $z' \in \{0,1\}^M$, M is the number of simplified input features, and $\Phi_i$ is the effect coefficient which is attributed to each feature, and is also of $\Phi_i \in \mathbb{R}$.

While other methods such as LIME also satisfy the condition of equation (34), SHAP has the advantage of generating a single unique solution with the three desirable properties local accuracy, missingness, and consistency. Lundberg and Lee (2017) formulated the SHAP explanation model as:

$$\Phi_i(f,x) = \sum_{z' \subseteq x'} \frac{|z'|!\,(M - |z'| - 1)!}{M!}[f_x(z') - f_x(z'\backslash i)] \qquad (35)$$

where $|z'|$ represents the number of non-zero entries in z', and $z' \subseteq x$ represents all $z'$ vectors where the nonzero entries are also a subset of the nonzero entries in $x'$. SHAP values are able to satisfy the local accuracy, missingness, and consistency properties which are detailed by Lundberg and Lee (2017), and are expressed as:

$$f_x(z') = f\big(h_x(z')\big) = E[f(z)|z_S] \qquad (36)$$

Where S is the set of non-zero indices in z', wherein $h_x(z') = z_S$ is the simplified input mapping where $z_S$ has missing values for features not in the set S. In simpler terms, SHAP explains a model by decomposing each of its input parameters and explaining whether their contribution adds or subtracts to the model output. SHAP are used in this study to explain the predictions and importance of each individual input feature for the proposed Decision Tree model. This is demonstrated in Figure 4.7 where a summary plot for each output prediction is separately generated.

(a)



(b)



(c)
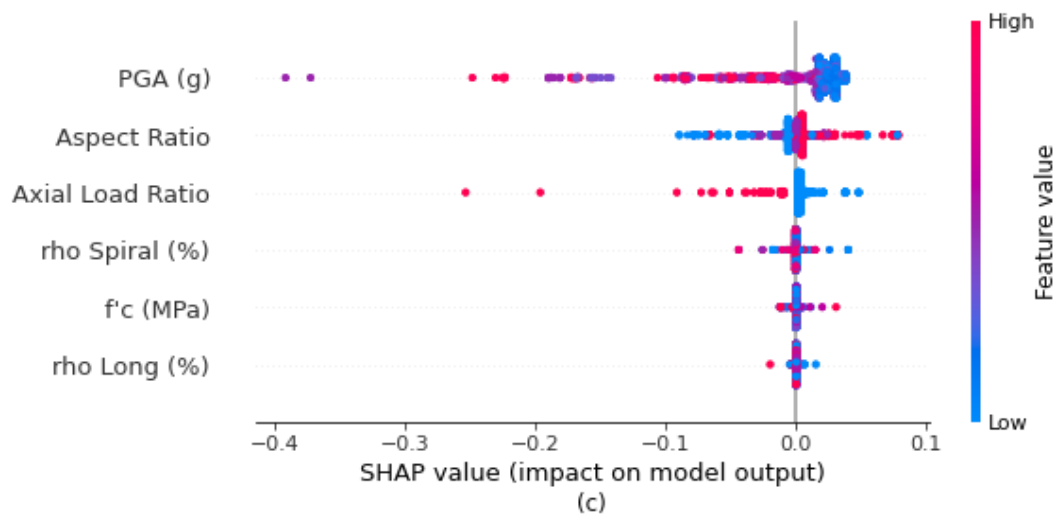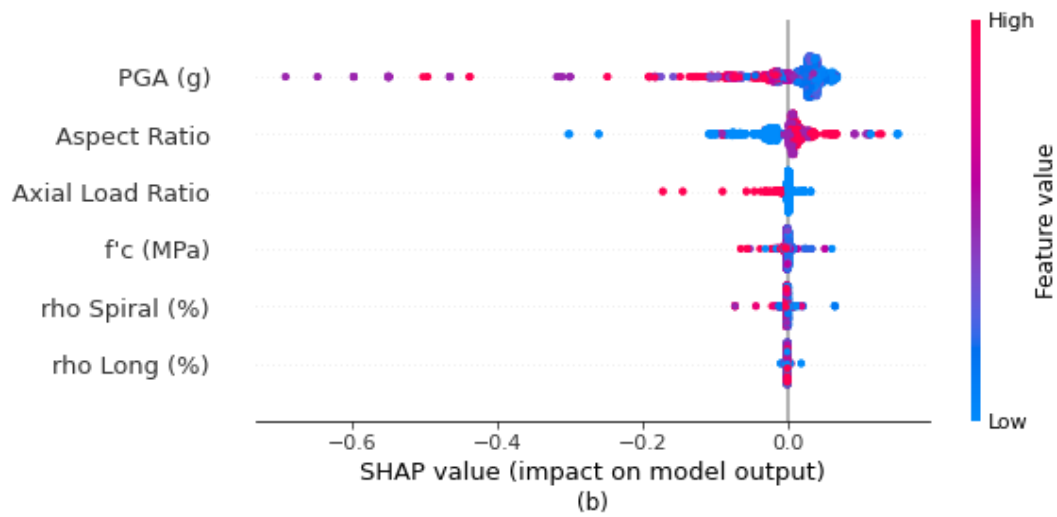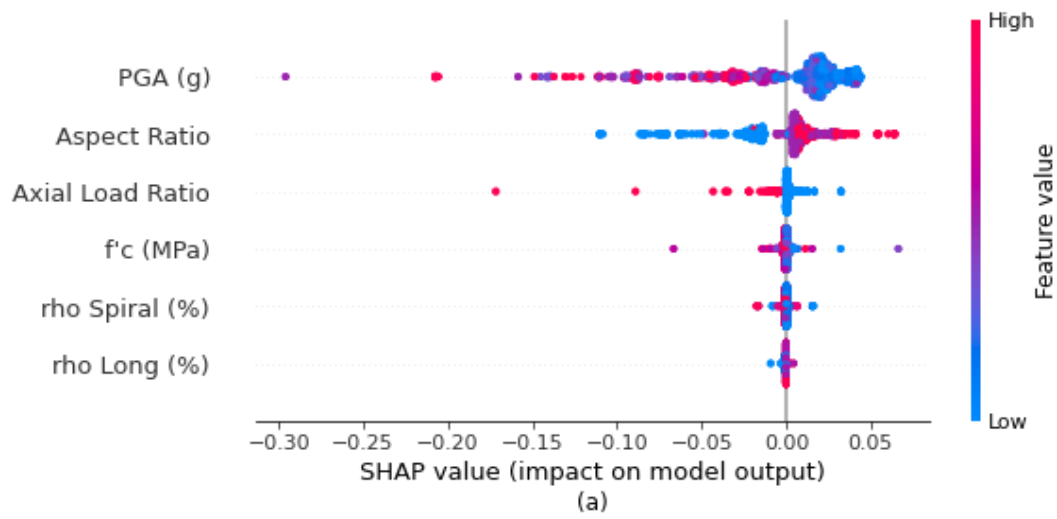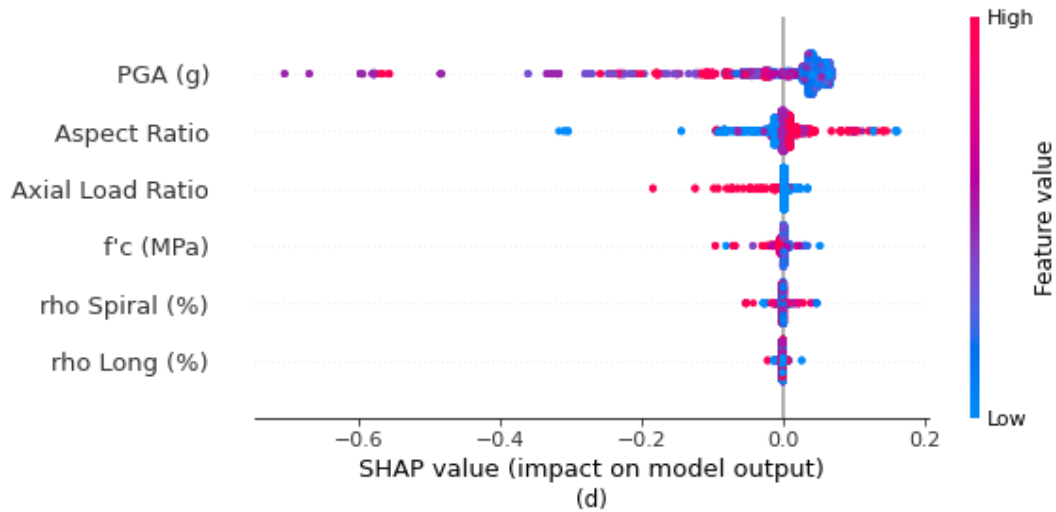
Figure 4.7 SHAP summary plots describing input feature importance in the regression of: (a) residual post-MS lateral capacity reduction, (b) residual post-AS lateral capacity reduction, (c) residual post-MS axial capacity reduction, (d) residual post-AS axial capacity reduction

From Figure 4.7, it can be seen that the allocation of input feature importance allows for greater insight of model performance. Peak ground acceleration is again determined as having the highest influence on model output; however, with SHAP it is also evident that higher PGA values contribute to lower residual post-earthquake axial and lateral capacities, as was expected. Similarly, the effect of column aspect ratio is deemed to contribute to relatively higher residual capacities in cases of high values, representing taller columns with higher fundamental periods. Axial load ratio is also shown to have the same explanation as was inferred in the previous section; wherein higher axial load ratios equate to a higher mass. Of the remaining input features, longitudinal reinforcement ratio is consistently the least important variable in both explainers. This offers more insight into the formulation of the machine learning models, than it does into the seismic performance of the columns, since it should have been expected to influence column axial capacity. However, since the residual capacities output by the models are done using percent values instead of kilonewtons, there is little output variance to be explained by the SHAP.

## 4.8 Summary

This chapter presented a detailed overview of the methods selected to drive the machine learning framework for use in the prediction of residual bridge pier capacities following mainshock-

aftershock sequences. Multiple techniques are selected for evaluation which cover simplistic linear models, shrinkage methods, nearest neighbors, decision tree methods, support vector machines, and neural networks. To effectively select the top performing machine learning model two evaluation strategies are employed, namely train-test splitting and k-fold crossvalidation. Models are first established and data is scaled and shuffled to ensure random sampling and better performance. A grid search algorithm for tuning each of the models is combined with the k-fold crossvalidation to determine the optimal parameter configuration for each of the ML methods which are being tested, using a reference index of four commonly used metrics. The tuned models' predictive capabilities are analysed using the previously withheld test data to demonstrate the accuracy of the models in the future when faced with outside sources of data. Among the models evaluated, the decision tree regressor was determined to be most suitable in predicting bridge pier residual capacities. The associated metrics which were obtained during the test set evaluation suggest that the DT model has good correlation and strong statistical significance, and the lowest residual errors amongst the other models tested.

# Chapter 5    Fragility Analysis of Reinforced Concrete Bridge Pier

## Subjected to Mainshock-Aftershock Sequence

## 5.1    General

Bridges play a key role in the transportation sector while serving as lifelines for the economy and safety of communities. The need for resilient bridges is especially important following natural disasters, where they serve as evacuation, aid, and supply routes to an affected area. The reliance on the services bridges provide is a driving force in minimizing their loss of functionality against seismic hazards. One approach in ensuring the uninterrupted service of bridges during earthquakes is the evaluation of seismic vulnerability, through the use of fragility curves. Analytical fragility functions serve as a tool which express the probability of a structure reaching a certain damage state, when subjected to an earthquake of a particular intensity. The fragility of a given structure, is expressed as the conditional probability of a damage state (DS) occurring given a specific intensity measure (IM), which can be expressed mathematically as:

$$\text{Fragility} = \text{P}[DS|IM] \tag{37}$$

The objective of this chapter is to assess the fragility of the bridge piers divided into two classes such as piers designed using current PBD guidelines (PBD-compliant) and piers with deficient transverse reinforcement (PBD-deficient) to explore the additional hazard imposed by mainshock-aftershock sequences. The analytical modelling techniques which were detailed in Chapter 3 are employed in performing nonlinear time history analysis for 50 mainshock-only and mainshock-aftershock ground motions. The resulting seismic responses of the bridge piers are used in deriving fragility curves to evaluate the increased aftershock demand of the studied piers.

## 5.2    Probabilistic seismic demand model

For bridges subjected to aftershocks following an initial mainshock, the probability of additional damage to the already affected structure can be expected to increase. Probabilistic seismic demand models (PSDM) provide the basis for fragility curve development, where the conditional probability of damage state exceedance under a given ground motion intensity is expressed. The

PSDM establishes a correlation between the engineering demand parameters (EDP) and the ground intensity measures (IMs). In this research, the component level models are used to generate the analytical fragility functions using nonlinear time history analyses of models C1 to C10 and C11 to C20, respectively. Two of the most common approaches for PSDM are the scaling approach (Bhuiyan and Alam 2012; Zhang and Huo 2009) and the cloud approach (Billah et al. 2013; Choi et al. 2004; Nielson and DesRoches 2007a; b; Ramanathan et al. 2015). In the scaling approach, ground motion data is scaled to determined intensity levels, via incremental dynamic analysis (IDA) which is performed for each increment. In contrast, the cloud approach neglects any scaling, and instead performs nonlinear time history analysis (NLTHA) using the as-recorded motions to develop the PSDM.

In this research, the cloud method is utilised due to the quality and availability of the as-recorded mainshock-aftershock records which have been gathered specifically to represent the seismic hazards typically present in Vancouver, British Columbia. In the selected PSDM approach, regression analysis is performed to obtain the mean and standard deviation for the minimum and extensive damage states based on the power-law function (Cornell et al. 2002) which provides a logarithmic correlation between the EDP and selected IM in the form of:

$$\text{EDP} = \text{a}(IM)^b \tag{38}$$

The above equation can be expressed in the transformed space, where the parameter b is the slope and parameter ln(a) is the vertical intercept, such that a and b can be estimated through regression analysis of the response data provided through the NLTHA. The transformed equation is expressed as:

$$\ln(EDP) = \ln(a) + \text{b} * \ln(IM) \tag{39}$$

In order to supplement additional data for the cloud approach where the peak ground acceleration (PGA) exceeds the maximum unscaled PGA of the selected ground motion records, additional entries are extrapolated using the above equation. In the development of the PSDMs, the suite of parameterized bridge piers are subjected to the aforementioned MS-AS groundmotion suite, with peak column drift demands recorded. The logarithmic standard deviation (dispersion) of the drift demand, $\beta_{EDP|IM}$ conditioned upon the IM is estimated using the following equation (Baker and Cornell 2006):

$$\beta_{\text{EDP|IM}} \cong \sqrt{\frac{\sum_{i=1}^{N}(\ln(EDP) - \ln(a * IM^b))^2}{N-2}} \qquad (40)$$

where N is the total number of EDP|IM data entries. The fragility curves for the different damage levels considered can be developed using the intensity measure and engineering demand parameters using equation (41) (Nielson 2005).

$$P[DS|IM] = \Phi\left[\frac{\ln(IM) - \ln(IM_n)}{\beta_{comp}}\right] \qquad (41)$$

$$where, \qquad \ln(IM_n) = \frac{\ln(S_c) - \ln(a)}{b} \qquad (42)$$

In which, $\Phi(\cdot)$ is the standard normal cumulative distribution function, $IM_n$ is the median value of the intensity measure, $S_c$ is the median value for the damage states of the bridge pier, and a and b are the regression coefficients of the PSDM. Lastly, the dispersion component is calculated using equation (41) (Nielson 2005).

$$\beta_{comp} = \frac{\sqrt{\beta_{\text{EDPIM}}^2 + \beta_c^2}}{b} \qquad (43)$$

Where $\beta_c$ is the dispersion value for the damage states of the bridge pier.

## 5.3    Fragility Assessment of Bridge Piers Subjected to Mainshock-Aftershock Sequence

5.3.1 Characterization of damage states

Fragility function requires the description of damage states (DS) which reflect the element and system level damage quantitatively and qualitatively. An important step in generating fragility curves is to define a qualitative or quantitative measure of various stages of damage known as damage states (DS). Past researchers have considered different forms of EDPs to measure the DS of bridge piers such as Park and Ang damage index (Park and Ang 1985), bridge pier capacity demand ratio (Hwang et al. 2000), drift limits (Dutta and Mander 1999), displacement ductility (Alipour et al. 2013; Billah et al. 2013), curvature ductility (Nielson and DesRoches 2007b; Padgett and DesRoches 2009), rotational ductility (Banerjee and Chi 2013), maximum drift (Billah

and Alam 2018; Gardoni et al. 2003), and residual drift (Billah and Alam 2015, 2018). Some researchers considered material strain-based damage states (Mackie and Stojadinović 2005) and maximum drift corresponding to different seismic performance criteria as DS (Billah and Alam 2016; Todorov and Billah 2021) for fragility assessment of bridge piers.

A common approach to defining damage states in the seismic vulnerability assessment of engineering structures (Billah and Alam 2016; Billah et al. 2013; Todorov and Billah 2021) is accomplished using the damage levels provided in HAZUS-MH (2011). However, in order to provide a basis for comparison with existing CHBDC PBD guidelines, the established damage levels for major route bridges are used instead; namely, minimal and extensive damage states. Limit state capacities are derived based on the drifts obtained from static pushover analysis of the bridge piers corresponding to the performance levels defined in CHBDC (Table 3.2). Typically, DSs are linked to each bridge piers' capacity which are characterized by the two parameters median, $S_C$ and dispersion, $\beta_c$ as shown in Eq. 37 and 38, respectively. These two parameters are considered to follow a lognormal distribution. However, all the limit state capacities obtained from pushover analyses are associated with uncertainties that are described using a lognormal standard deviation or dispersion ($\beta_c$). The values of lognormal standard deviation or dispersion ($\beta_c$) have been obtained following the procedure described in Nielson (2005). Table 5.1 and Table 5.2 present the limit state capacities for the bridge piers in terms of median and dispersion values.

Table 5.1 Limit states for PBD-compliant bridge pier fragility assessment

|  | Minimal Damage | | Extensive Damage | |
|---|---|---|---|---|
|  | $S_c$ | $\beta_c$ | $S_c$ | $\beta_c$ |
| Column C1 | 1.15 | 0.59 | 4.29 | 0.64 |
| Column C2 | 1.56 | 0.59 | 5.87 | 0.64 |
| Column C3 | 1.91 | 0.59 | 7.32 | 0.64 |
| Column C4 | 1.20 | 0.59 | 4.33 | 0.64 |
| Column C5 | 1.63 | 0.59 | 5.92 | 0.64 |
| Column C6 | 2.01 | 0.59 | 7.36 | 0.64 |
| Column C7 | 1.23 | 0.59 | 4.12 | 0.64 |
| Column C8 | 1.68 | 0.59 | 5.62 | 0.64 |
| Column C9 | 2.06 | 0.59 | 6.93 | 0.64 |
| Column C10 | 1.67 | 0.59 | 5.29 | 0.64 |

Table 5.2 Limit states for PBD-deficient bridge pier fragility assessment

|  | Minimal Damage | | Extensive Damage | |
| --- | --- | --- | --- | --- |
|  | $S_c$ | $\beta_c$ | $S_c$ | $\beta_c$ |
| Column C11 | *1.16* | *0.59* | *3.51* | *0.64* |
| Column C12 | *1.59* | *0.59* | *4.74* | *0.64* |
| Column C13 | *1.95* | *0.59* | *5.79* | *0.64* |
| Column C14 | *1.23* | *0.59* | *2.76* | *0.64* |
| Column C15 | *1.68* | *0.59* | *3.73* | *0.64* |
| Column C16 | *2.07* | *0.59* | *4.52* | *0.64* |
| Column C17 | *1.27* | *0.59* | *2.87* | *0.64* |
| Column C18 | *1.73* | *0.59* | *3.89* | *0.64* |
| Column C19 | *2.13* | *0.59* | *4.72* | *0.64* |
| Column C20 | *1.70* | *0.59* | *3.31* | *0.64* |

5.3.2 Development of Fragility Curves

The formulated PSDM is used to derive the fragility curves which help express the effect of aftershock consideration on the seismic demand imposed on the studied bridge piers. Because of the efficiency, practicality, sufficiency, and hazard computability of PGA, many researchers (Billah et al. 2013; Padgett et al. 2008) have suggested PGA as the optimal intensity measure for fragility assessment of bridges and bridge piers. Accordingly, for the purpose of this study, and to maintain consistency with the CHBDC, PGA is selected as the optimal IM for this study. Furthermore, the PGA intensity measure is distinguished for both mainshock-only and mainshock-aftershock fragility analyses. An appropriate EDP selection is a function of the structural system and desired performance objectives. In this study, maximum drift (MD) of the bridge pier, which represents different performance-based limit states as per CHBDC, is considered as the EDP.

Nonlinear time history analyses which were carried out for each of the bridge piers for both MS-only and MS-AS earthquake records are used to determine the maximum drift of the piers. The resulting maximum drift and peak ground acceleration pairs are incorporated into a PSDM which establishes a linear regression of the pair in the log-transformed space for each of the ground motions considered. Figure 5.1 shows the PSDMs for columns C1 and C11 for MS-only and MS-AS ground motions, where the equation for the linear regression line as well as the corresponding $R^2$ value are also shown. The corresponding $R^2$ values of the PSDMs show a weak correlation,

which is in part due to the generally low number of EDP-IM pairs considered. It is commonplace to simply use more ground motions or to perform multiple NLTHAs with scaling such as incremental dynamic analysis (IDA) in order to generate more points for this approach, however, due to the large number of columns considered in this study, a trade-off was made in PSDM correlation strength.
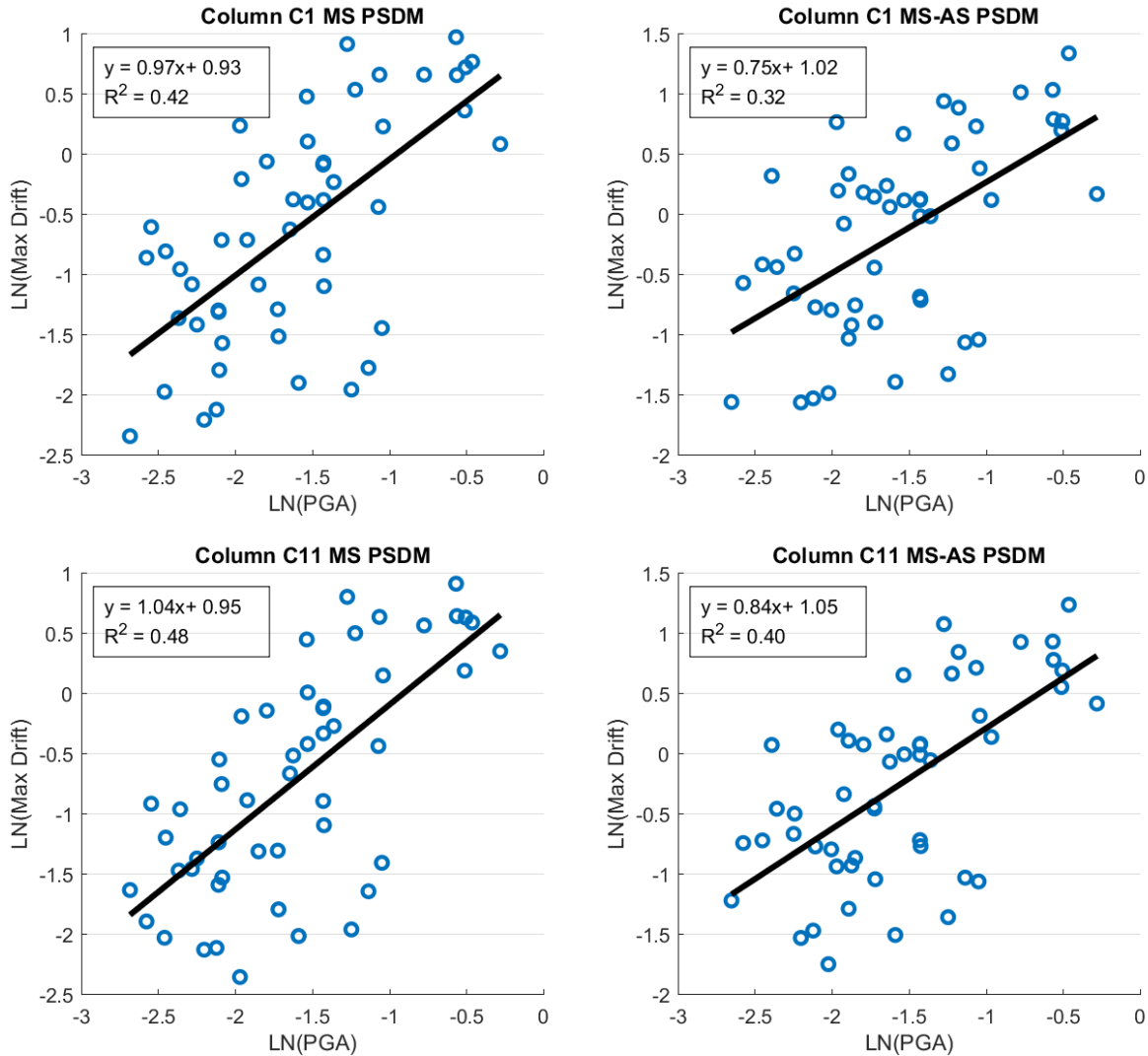


Figure 5.1 PSDMs for different bridge piers subjected to: (a) column C1 subjected to MS-only ground motion, (b) column C1 subjected to MS-AS ground motion, (c) column C11 subjected to MS-only ground motion, (d) column C11 subjected to MS-AS ground motion

Peak responses are determined from each of the analysis results and a regression analysis is carried out to estimate a, b, and $\beta_{EDP|IM}$. Table 5.3 and Table 5.4 detail the regression parameters from equations (38) and (39) for each of the studied bridge piers in MS-only and MS-AS scenarios. It can be seen that an increase in the regression parameters a and b is evident when comparing MS-only to MS-AS PSDMs, as well as the comparison between the two classes of bridge piers (i.e., C1 compared to C11). These differences correlate to an increase in median seismic demand when considering aftershock effects, or subjecting a bridge pier with deficient transverse reinforcement to the same set of hazards. On the other hand, the dispersion parameter $\beta_{EDP|IM}$ tends to decrease for the same scenarios, this however only suggests a stronger correlation of the estimated a and b values.

Table 5.3 PSDMs for PBD-compliant bridge piers

|  | Mainshock-Only | | | Mainshock-Aftershock | | |
|---|---|---|---|---|---|---|
|  | a | b | $\beta_{EDP|IM}$ | a | b | $\beta_{EDP|IM}$ |
| Column C1 | 2.523 | 0.965 | 0.448 | 2.785 | 0.755 | 0.414 |
| Column C2 | 1.788 | 0.614 | 0.483 | 2.553 | 0.568 | 0.418 |
| Column C3 | 2.393 | 0.663 | 0.322 | 2.701 | 0.514 | 0.339 |
| Column C4 | 2.113 | 0.788 | 0.437 | 2.516 | 0.629 | 0.415 |
| Column C5 | 2.629 | 0.783 | 0.377 | 2.988 | 0.623 | 0.386 |
| Column C6 | 1.808 | 0.470 | 0.349 | 2.423 | 0.426 | 0.333 |
| Column C7 | 2.055 | 0.739 | 0.442 | 2.558 | 0.597 | 0.430 |
| Column C8 | 2.624 | 0.752 | 0.354 | 3.026 | 0.602 | 0.361 |
| Column C9 | 2.420 | 0.612 | 0.309 | 2.874 | 0.505 | 0.322 |
| Column C10 | 2.878 | 0.769 | 0.320 | 2.984 | 0.567 | 0.314 |

Table 5.4 PSDMs for PBD-deficient bridge piers

| | Mainshock-Only | | | Mainshock-Aftershock | | |
|---|---|---|---|---|---|---|
| | a | b | $\beta_{EDP|IM}$ | a | b | $\beta_{EDP|IM}$ |
| Column C11 | 2.579 | 1.038 | 0.423 | 2.860 | 0.836 | 0.387 |
| Column C12 | 2.392 | 0.829 | 0.432 | 2.815 | 0.662 | 0.404 |
| Column C13 | 2.428 | 0.772 | 0.400 | 2.370 | 0.511 | 0.352 |
| Column C14 | 1.748 | 0.772 | 0.471 | 2.356 | 0.681 | 0.410 |
| Column C15 | 2.172 | 0.724 | 0.389 | 2.685 | 0.608 | 0.399 |
| Column C16 | 2.332 | 0.678 | 0.304 | 2.534 | 0.504 | 0.326 |
| Column C17 | 2.151 | 0.872 | 0.426 | 2.424 | 0.674 | 0.399 |
| Column C18 | 2.049 | 0.680 | 0.404 | 2.431 | 0.537 | 0.394 |
| Column C19 | 2.116 | 0.636 | 0.351 | 2.340 | 0.442 | 0.312 |
| Column C20 | 2.660 | 0.750 | 0.374 | 2.925 | 0.571 | 0.328 |

Using the formulation shown in Eq. (41) combined with the seismic demand and capacity models described in the preceding sections, fragility curves for the PBD-compliant and PBD-deficient bridge piers are generated. These curves provide the basis for comparing the effect of aftershocks as well as the bridge pier transverse reinforcement configurations on bridge pier vulnerability. Since it is not worthwhile to compare the fragilities of each bridge pier individually, median fragility curves are developed for the PBD-compliant and PBD-deficient bridge piers to facilitate a meaningful comparison. The median fragility curves developed for the PBD-compliant bridge piers (C1 - C10) are displayed in Figure 5.2, and fragility curves developed for columns C11 - C20 which are representative of columns with inadequate transverse reinforcement are shown in Figure 5.3. Comparison between the MS-only and MS-AS fragility curves in Figure 5.2 confirm the conclusions which other research has found where an increased seismic vulnerability of structures subjected to aftershock effects is observed. Moreover, the vertical offset between the MS-only and MS-AS curves for the minimal damage level demonstrate a large increase in the probability of damage occurrence which is especially high at lower groundmotion intensities, and later converging at higher intensities. A dissimilar effect is observed for the extensive damage level, where low intensities pose similar levels of risk, and a divergence is observed when the ground motion intensity increases.

Table 5.5 summarizes the median probability of exceeding minimal and extensive damage states for the PBD-compliant and PBD-deficient bridge piers at peak ground acceleration of 0.20g and

0.37g corresponding to the design PGA for the 475- and 2475-year return period earthquake, respectively. For the PBD-compliant piers, a 35.7% increase in the median probability of exceedance is observed for minimal damage levels when aftershock effects are considered. On the other hand, the probability of exceedance for extensive damage levels does not increase much when subjected to aftershock. Overall, the increased seismic demand that aftershocks present for the extensive damage level is fairly insignificant, whereas the minimal damage criteria show a larger variance in the two curves. This suggests that the PBD-compliant columns are fairly well designed for aftershock effects in the case of extensive damage levels, and are relatively under-designed in the case of minimal damage levels.

Table 5.5 Probability of exceeding different damage states at design PGAs

| | Probability of exceedance (%) | |
|---|---|---|
| Damage State | PBD-Compliant | PBD-Deficient |
| MS-Minimal | 28.77 | 18.10 |
| MS-AS Minimal | 64.47 | 54.22 |
| MS-Extensive | 0.07 | 0.60 |
| MS-AS Extensive | 1.18 | 4.59 |

Moreover, in the case of fragility curves for the PBD-deficient columns shown in Figure 5.3, the same effect of increased seismic demand is present for aftershock effects. For the PBD-deficient piers, a 36.1% increase in the median probability of exceedance is observed for minimal damage levels in Table 5.5. This increase is very similar to the PBD-compliant piers; however, the overall risk of exceedance is approximately 10% lower. This suggests a lower seismic demand as compared to the PBD-compliant piers which is contrary to what is expected, and warrants further investigation. For extensive damage levels, there is a much greater risk of exceedance as compared to the PBD-compliant columns. Despite a 4% increase in aftershock vulnerability being observed at the design PGA, the fragility curves in Figure 5.3 demonstrate a much greater seismic vulnerability at higher intensities as compared to the PBD-compliant. Overall, the increased seismic demand that aftershocks present for bridge piers with insufficient transverse reinforcement is telling of a much greater seismic risk. This suggests that there is a need for retrofitting strategies for much of the aging infrastructure where exposure to aftershocks is a possibility.

Furthermore, the large variation in fragility between the minimal and extensive damage levels is to be expected, but leaves more information to be desired. A design strategy that defines two performance criteria at extreme ends of damage levels leaves the opportunity for improvement of current practices. What's more, is that the 2014 edition of the CHBDC considered an optional repairable damage state corresponding to 975-year return period earthquakes for major route bridges which has since been removed in the 2019 edition. Developing MS-AS performance limit states for the three damage levels would make for better performance criteria which would better capture the seismic risk of bridges, but could also lead to more resilient designs.
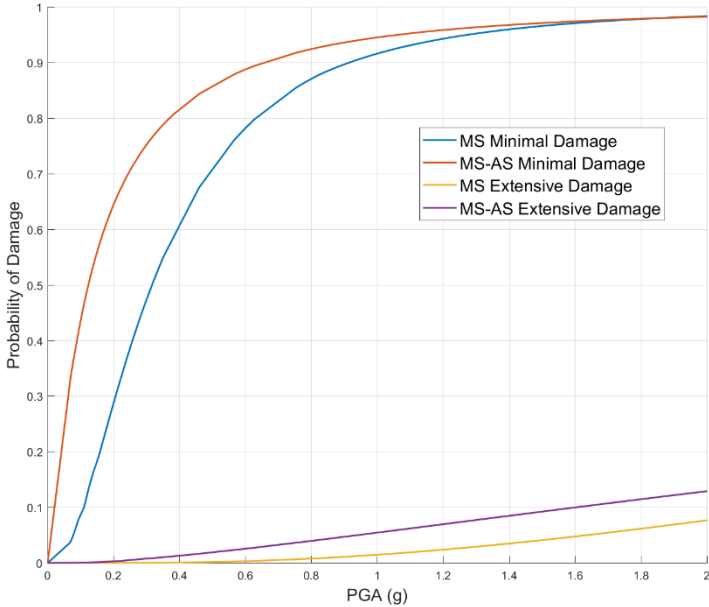


Figure 5.2 Median fragility curves for PBD-compliant bridge piers subjected to mainshock-only and mainshock-aftershock sequences

78
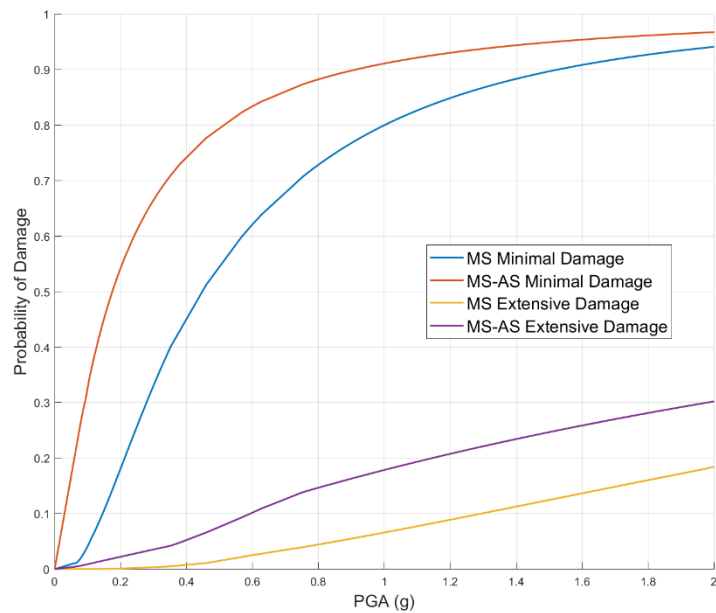
Figure 5.3 Fragility curves for PBD-deficient bridge piers subjected to mainshock-only and mainshock-aftershock sequences

## 5.4 Summary

The fragility of 20 single column RC bridge piers subjected to mainshock and mainshock-aftershock sequences were assessed in order to investigate the effects of the additional aftershocks on the damaged components. Additionally, the columns were divided into two classes in which 10 were designed using current PBD guidelines found in the 2019 edition of the Canadian highway bridge design code, and the remaining 10 with deficient transverse reinforcement such as the detailing found in Canadian bridges constructed before 2000, respectively. To adequately investigate the seismic vulnerability of the bridge piers when exposed to aftershock effects, a suite of 50 ground motions is utilized to determine the seismic capacities of the piers. The resulting seismic performance is used in deriving fragility functions which more easily express the likelihood of capacity exceedance. The results obtained from both sets of fragility curves confirm previous studies which suggest the increased vulnerability of structures during aftershocks. Comparison between the fragility functions of the piers designed according to current PBD guidelines and piers with insufficient transverse reinforcement detailing indicate that the PBD-

deficient piers have larger increases of aftershock damage risk as compared to the PBD-compliant piers. Furthermore, while the PBD-deficient piers have an overall lower risk of exceeding minimal damage levels, their extensive damage vulnerability is significantly increased as compared to the PBD-compliant piers.

# Chapter 6    Conclusions and Future Work

## 6.1    Summary

In order to address the growing interest in developing a generation of bridge infrastructure that is more resilient to seismic hazards, a greater understanding needs to be developed for hazard interactions such as mainshock-aftershock sequences. Current bridge design practices employed in Canada and outlined in the Canadian Highway Bridge Design Code recognize the presence of aftershock effects but do not provide any explicit guidelines to practicing engineers. In order to help bridge this knowledge gap, this thesis focused on analytically examining a wide range of reinforced concrete bridge piers which represent a variety of configurations found in Canadian bridges. A detailed literature review on current MS-AS bridge design and fragility analysis studies as well as machine learning applications in the fields of structural and seismic engineering was performed in order to identify research gaps in adjacent studies. Finite element models were developed and validated for capturing the seismic performance of bridge piers, and a strain-based strength modification scheme was introduced for capturing post earthquake degradation effects in their plastic hinge regions.

This thesis developed a machine learning post-earthquake capacity framework for the prediction of lateral and axial capacities of bridge piers following mainshock and aftershock sequences. This proposed data driven model will allow for the rapid evaluation of a bridge pier's post-earthquake capacities, and can serve as a potential tool for determining rapid bridge repair strategies following mainshock-aftershock events, or for risk mitigation over the service life of such bridges by assisting in the retrofit or structural upgrade decision making process.

Finally, a fragility assessment of the selected bridge piers is performed where the effects of aftershocks are examined. A comparative analysis of the aftershock effects on the fragility of piers designed to current performance-based design standards as well as piers with insufficient transverse reinforcement has been carried out using the existing CHBDC performance criteria.

## 6.2    Research Limitations

The limitations of the research presented in this thesis are as follows:

- The effects of soil interaction were not analyzed, this can be particularly unconservative as soil liquefaction due to aftershocks is a concern for some soil types.

81

- Only single column, circular bridge piers were considered in this research.

- Various longitudinal and transverse reinforcement properties ($d_b$, $f_y$) were not considered.

- Only PGA was considered as the IM for developing fragility models and as the ML model input.

- Generating PSDMs using the cloud method with a limited number of unscaled ground motions can be improved upon by using a scaling approach such as IDA to generate more points.

## 6.3   Conclusions

A growing interest in more sophisticated seismic design methodology has introduced the concept of Performance Based Design to recent editions of the CHBDC, where a design must demonstrate that it has met performance criteria such as damage limits and service levels. Performance based design of bridges has the potential to be applied in many unique hazards or circumstances, but performance criteria must be established beforehand. While the CHBDC does acknowledge a need for consideration of aftershock effects, there is little guidance provided to practicing engineers. Therefore, there is great benefit to be realised in the development of PBD guidelines for mainshock-aftershock seismic sequences for scenarios in which the chance to assess and repair a bridge is not possible following a recent mainshock. To that effect, fiber based nonlinear modelling techniques with a proposed material strength degradation scheme are applied to study a set of bridge piers which are characteristic of a typical major route bridge located in Vancouver, British Columbia. A suite of 50 ground motions is selected using the conditional mean spectra method which consider the site location with a stiff soil class-D. Furthermore, an even distribution of record types such as crustal, inslab, and interface earthquakes are selected to properly capture the seismic hazards present in Vancouver. Nonlinear time history analysis of the unscaled ground motions is performed for the bridge piers considered, with MS and AS records being separated. The resulting seismic performance of the piers is used in developing a machine learning database to train and evaluate a single best model for the prediction of post earthquake residual capacities. Based on the results of the machine learning study, the following conclusions have been developed:

- Median axial and lateral residual capacity of the bridge piers studied decreased from an initial post-mainshock damage state compared to subsequent post-aftershock damage state.

- The proposed machine learning model most suitable for the prediction of residual column capacity was the DecisionTreeRegressor, which obtained a high statistical significance, strong predictive accuracy, and overall low model error.
- Of the studied model input parameters, peak ground acceleration (PGA) was by and large the most influential input parameter, which accounted for the majority of the relative importance in the prediction of post earthquake lateral and axial capacities.
- The proposed machine learning model is to be made available open source for the use as a potential tool for practicing engineers or future research efforts where a rapid prediction in the residual capacity of bridge piers following an earthquake can be generated.

The application of the machine learning framework can be especially useful in scenarios where the prediction of post-earthquake bridge capacity would lead to a more informed decision-making process when evaluating the condition. Following a recent earthquake, provided that peak ground acceleration is recorded, future users are be able to rapidly estimate bridge capacity, along with potential further capacity degradation should aftershocks occur.

Furthermore, this research also considered an analytical fragility assessment for the studied bridge piers where fragility curves were developed to capture aftershock effects. Aftershock effects are evaluated for both piers designed using current PBD guidelines, as well as piers that have inadequate transverse reinforcement. Based on the results of the fragility assessment study, the following conclusions have been derived:

- The developed PSDMs which incorporated aftershock effects demonstrated an increased fragility for all bridge piers examined, for all damage levels considered.
- Bridge piers designed using current PBD guidelines were at an insignificant risk of exceeding extensive damage levels following mainshock-only and mainshock-aftershock excitations.
- Aftershock effects accounted for increases of 35% and greater for both PBD-compliant and PBD-deficient bridge piers' probability of exceeding minimal damage levels .

From the above conclusions it is evident that aftershocks pose an increased risk of damage to bridges; however, the results of the current work seem to indicate that piers designed using the PBD guidelines available in the 2019 edition of the CHBDC produce adequate seismic

performance when subjected to 2475-year return period earthquakes, corresponding to the extensive damage level. On the other hand, the results of the fragility analysis indicate that performance criteria for the minimal damage level in the CHBDC are unconservative and lead to increased vulnerability.

## 6.4   Recommendation for future work

Further research is necessary to develop more comprehensive PBD guidelines for the aftershock consideration of bridges. This can be accomplished using a system-level bridge model which captures the seismic risk of multiple bridge components such as bearings and abutments, and effects such as soil structure interaction and girder unseating.

Performance based plastic design, such as that discussed in Chapter 2 has not yet been applied to bridges, when considering aftershock effects and would generate meaningful information into the seismic demand increase. A further study which considers multiple bridge pier geometries is recommended to better understand aftershock effects.

Improvements to the fragility analysis in this study are able to be accomplished, wherein a sensitivity analysis for determining the optimal IM is introduced, or a conditional model for aftershock performance given a mainshock is employed. Furthermore, performing IDA would generate more data points which would lead to stronger PSDMs.

The opportunity to further enhance the machine learning models developed in this research is available, either through the synthesis of further bridge pier performance data with geometrical and material properties outside of those explored in this research, or by obtaining experimental data. Furthermore, the possibility of developing a hybrid fragility analysis using the data driven machine learning post-earthquake capacities is able to be explored for developing a more robust PSDM.

# References

Abdollahzadeh, G., Mohammadgholipour, A., and Omranian, E. (2019a). "Seismic Evaluation of Steel Moment Frames Under Mainshock–Aftershock Sequence Designed by Elastic Design and PBPD Methods." *Journal of Earthquake Engineering*, 23(10), 1605–1628.

Abdollahzadeh, G., Mohammadgholipour, A., and Omranian, E. (2019b). "Development of the Performance-Based Plastic Design Method by Considering the Effects of Aftershocks." *Journal of Earthquake Engineering*, 1–25.

Alessandri, S., Giannini, R., and Paolacci, F. (2013). "Aftershock risk assessment and the decision to open traffic on bridges: AFTERSHOCK RISK ASSESSMENT AND THE DECISION TO OPEN TRAFFIC ON BRIDGES." *Earthquake Engineering & Structural Dynamics*, 42(15), 2255–2275.

Alipour, A., Shafei, B., and Shinozuka, M. (2013). "Reliability-based calibration of load factors for LRF design of reinforced concrete bridges under multiple extreme events: scour and earthquake." *Journal of Bridge Engineering*, 10.

Alipour, M., Harris, D. K., Barnes, L. E., Ozbulut, O. E., and Carroll, J. (2017). "Load-Capacity Rating of Bridge Populations through Machine Learning: Application of Decision Trees and Random Forests." *Journal of Bridge Engineering*, 22(10), 04017076.

Applied Technology Council. (1996). *Improved Seismic Design Criteria for California Bridges: Resource Document*.

Atkinson, G. M., and Goda, K. (2011). "Effects of Seismicity Models and New Ground-Motion Prediction Equations on Seismic Hazard Assessment for Four Canadian Cities." *Bulletin of the Seismological Society of America*, 101(1), 176–189.

Baker, J. W. (2011). "Conditional Mean Spectrum: Tool for Ground-Motion Selection." *Journal of Structural Engineering*, 137(3), 322–331.

Baker, J. W., and Cornell, C. A. (2006). *Vector-Valued Ground Motion Intensity Measures for Probabilistic Seismic Demand Analysis*.

Bandini, P., Padgett, J., and Paultre, P. (2019). "Seismic fragility analysis of a highway bridge in Quebec via metamodelling." Quebec, Canada.

Banerjee, S., and Chi, C. (2013). "State-dependent fragility curves of bridges based on vibration measurements." *Probabilistic Engineering Mechanics*, 33, 116–125.

Båth, M. (1965). "Lateral inhomogeneities of the upper mantle." *Tectonophysics*, 2(6), 483–514.

Berry, M., and Eberhard, M. O. (2003). "Performance Models for Flexural Damage in Reinforced Concrete Columns." 162.

Bhuiyan, M. A. R., and Alam, M. S. (2012). "Seismic Vulnerability Assessment of a Multi-Span Continuous Highway Bridge Fitted with Shape Memory Alloy Bars and Laminated Rubber Bearings." *Earthquake Spectra*, SAGE Publications Ltd STM, 28(4), 1379–1404.

Billah, A., and Alam, M. (2016). "Performance based seismic design of concrete bridge pier reinforced with Shape Memory Alloy-Part 1: Development of Performance-Based Damage States." *ASCE J. Struct. Eng*, 142(12), 1–11.

Billah, A. H. M. M., and Alam, M. S. (2015). "Seismic Fragility Assessment of Concrete Bridge Pier Reinforced with Superelastic Shape Memory Alloy." *Earthquake Spectra*, SAGE Publications Ltd STM, 31(3), 1515–1541.

Billah, A. H. M. M., and Alam, M. S. (2018). "Probabilistic seismic risk assessment of concrete bridge piers reinforced with different types of shape memory alloys." *Engineering Structures*, 162, 97–108.

Billah, A. H. M. M., Alam, M. S., and Bhuiyan, M. A. R. (2013). "Fragility Analysis of Retrofitted Multicolumn Bridge Bent Subjected to Near-Fault and Far-Field Ground Motion." *Journal of Bridge Engineering*, 18(10), 992–1004.

Breiman, L. (2001). "Random Forests." *Machine Learning*, (45), 5–32.

California Department of Transportation. (1999). *Caltrans Seismic Design Criteria*. California Department of Transportation, Sacramento, CA.

Chai, Y. H., Priestley, M. J. N., and Seible, F. (1991). "Seismic Retrofit of Circular Bridge Columns for Enhanced Flexural Performance." *Structural Journal*, 88(5), 572–584.

Chang, G. A., and Mander, J. B. (1994). "Seismic Energy Based Fatigue Damage Analysis of Bridge Columns: Part 1 - Evaluation of Seismic Capacity." 244.

Chiu, C.-K., Sung, H.-F., Chi, K.-N., and Hsiao, F.-P. (2019). "Experimental Quantification on the Residual Seismic Capacity of Damaged RC Column Members." *International Journal of Concrete Structures and Materials*, 13(1), 17.

Choi, E., DesRoches, R., and Nielson, B. (2004). "Seismic fragility of typical bridges in moderate seismic zones." *Engineering Structures*, 26(2), 187–199.

Cornell, C. A., Jalayer, F., Hamburger, R. O., and Foutch, D. A. (2002). "Probabilistic Basis for 2000 SAC Federal Emergency Management Agency Steel Moment Frame Guidelines." *Journal of Structural Engineering*, 128(4), 526–533.

Di Ludovico, M., Polese, M., Gaetani d'Aragona, M., Prota, A., and Manfredi, G. (2013). "A proposal for plastic hinges modification factors for damaged RC columns." *Engineering Structures*, 51, 99–112.

Dong, Y., and Frangopol, D. M. (2015). "Risk and resilience assessment of bridges under mainshock and aftershocks incorporating uncertainties." *Engineering Structures*, 83, 198–208.

Dutta, A., and Mander, J. B. (1999). "Seismic fragility analysis of highway bridges." Tokyo, Japan, 311–325.

Fakharifar, M., Chen, G., Dalvand, A., and Shamsabadi, A. (2015a). "Collapse Vulnerability and Fragility Analysis of Substandard RC Bridges Rehabilitated with Different Repair Jackets Under Post-mainshock Cascading Events." *International Journal of Concrete Structures and Materials*, 9(3), 345–367.

Fakharifar, M., Chen, G., Sneed, L., and Dalvand, A. (2015b). "Seismic performance of post-mainshock FRP/steel repaired RC bridge columns subjected to aftershocks." *Composites Part B: Engineering*, 72, 183–198.

Feng, Y., Kowalsky, M. J., and Nau, J. M. (2015). "Finite-Element Method to Predict Reinforcing Bar Buckling in RC Structures." *Journal of Structural Engineering*, 141(5), 04014147.

Figueiredo, E., Moldovan, I., Santos, A., Campos, P., and Costa, J. C. W. A. (2019). "Finite Element–Based Machine-Learning Approach to Detect Damage in Bridges under Operational and Environmental Variations." *Journal of Bridge Engineering*, 24(7), 04019061.

Filippou, F. C., Popov, E. P., and Bertero, V. V. (1983). "Effects of bond deterioration on hysteretic behavior of reinforced concrete joints." Earthquake Engineering Research Center, University of California Berkeley.

Franchin, P., and Pinto, P. E. (2009). "Allowing Traffic Over Mainshock-Damaged Bridges." *Journal of Earthquake Engineering*, 13(5), 585–599.

Gardoni, P., Mosalam, K. M., and Kiureghian, A. D. (2003). "PROBABILISTIC SEISMIC DEMAND MODELS AND FRAGILITY ESTIMATES FOR RC BRIDGES." *Journal of Earthquake Engineering*, 7(sup001), 79–106.

Ghosh, J., Padgett, J. E., and Dueñas-Osorio, L. (2013). "Surrogate modeling and failure surface visualization for efficient seismic vulnerability assessment of highway bridges." *Probabilistic Engineering Mechanics*, 34, 189–199.

Ghosh, J., Padgett, J. E., and Sánchez-Silva, M. (2015). "Seismic Damage Accumulation in Highway Bridges in Earthquake-Prone Regions." *Earthquake Spectra*, 31(1), 115–135.

Glorot, X., Bordes, A., and Bengio, Y. (2011). "Deep Sparse Rectifier Neural Networks." Fort Lauderdale, FL, USA, 315–323.

Goda, K. (2015). "Record selection for aftershock incremental dynamic analysis: RECORD SELECTION FOR AFTERSHOCK INCREMENTAL DYNAMIC ANALYSIS." *Earthquake Engineering & Structural Dynamics*, 44(7), 1157–1162.

Goda, K., and Atkinson, G. M. (2011). "Seismic performance of wood-frame houses in south-western British Columbia." *Earthquake Engineering & Structural Dynamics*, 40(8), 903–924.

Goda, K., and Salami, M. R. (2014). "Inelastic seismic demand estimation of wood-frame houses subjected to mainshock-aftershock sequences." *Bulletin of Earthquake Engineering*, 12(2), 855–874.

Goodnight, J. C., Feng, Y., Kowalsky, M. J., and Nau, J. M. (2015). *The effects of load history and design variables on performance limit states of circular bridge columns*.

Goodnight, J. C., Kowalsky, M. J., and Nau, J. M. (2016). "Strain Limit States for Circular RC Bridge Columns." *Earthquake Spectra*, 32(3), 1627–1652.

Haroun, M. A., Mosallam, A. S., Feng, M. Q., and Elsanadedy, H. M. (2003). "Experimental Investigation of Seismic Repair and Retrofit of Bridge Columns by Composite Jackets." *Journal of Reinforced Plastics and Composites*, SAGE Publications Ltd STM, 22(14), 1243–1268.

Haykin, S. S., and Haykin, S. S. (2009). *Neural networks and learning machines*. Prentice Hall, New York.

Hazus, M. (2011). "Multi-hazard loss estimation methodology: earthquake model hazus-MH MR5." Washington, D.C.

Hwang, H., Jernigan, J. B., and Lin, Y.-W. (2000). "Evaluation of Seismic Damage to Memphis Bridges and Highway Systems." *Journal of Bridge Engineering*, 5(4), 322–330.

Ibarra, L. F., and Krawinkler, H. (2005). *Global collapse of frame structures under seismic excitations*. Pacific Earthquake Engineering Research Center Berkeley, CA.

Jeon, J.-S., DesRoches, R., and Lee, D. H. (2016). "Post-repair effect of column jackets on aftershock fragilities of damaged RC bridges subjected to successive earthquakes." *Earthquake Engineering & Structural Dynamics*, 45(7), 1149–1168.

Jung, D., and Andrawes, B. (2018). "Seismic Damage Assessment of SMA-Retrofitted Multiple-Frame Bridge Subjected to Strong Main Shock–Aftershock Excitations." *Journal of Bridge Engineering*, 23(1), 04017113.

Keshtegar, B., and Nehdi, M. L. (2020). "Machine learning model for dynamical response of nano-composite pipe conveying fluid under seismic loading." *International Journal of Hydromechatronics*, 3(1), 38.

Kowalsky, M. J. (2000). "Deformation Limit States for Circular Reinforced Concrete Bridge Columns." *Journal of Structural Engineering*, 126(8), 869–878.

Lee, D. H., Kim, D., and Lee, K. (2009). "Analytical approach for the earthquake performance evaluation of repaired/retrofitted RC bridge piers using time-dependent element." *Nonlinear Dynamics*, 56(4), 463–482.

Lehman, D. E., and Moehle, J. P. (2000). "Seismic performance of well-confined concrete bridge columns." *PEER 1998/01*.

Li, Q., and Ellingwood, B. R. (2007). "Performance evaluation and damage assessment of steel frame buildings under main shock–aftershock earthquake sequences." *Earthquake Engineering & Structural Dynamics*, 36(3), 405–427.

Liang, Y., Yan, J. L., Cheng, Z. Q., Chen, P., and Ren, C. (2020). "Time-Varying Seismic Fragility Analysis of Offshore Bridges with Continuous Rigid-Frame Girder under Main Aftershock Sequences." *Journal of Bridge Engineering*, 25(8), 04020055.

Luco, N., Bazzurro, P., and Cornell, C. A. (2004). "Dynamic Versus Static Computation of the Residual Capacity of a Mainshock-Damaged Building to Withstand an Aftershock." Vancouver, BC, Canada, 15.

Lundberg, S., and Lee, S.-I. (2017). "A Unified Approach to Interpreting Model Predictions." *arXiv:1705.07874 [cs, stat]*.

Luo, H., and Paal, S. G. (2018). "Machine Learning–Based Backbone Curve Model of Reinforced Concrete Columns Subjected to Cyclic Loading Reversals." *Journal of Computing in Civil Engineering*, 32(5), 04018042.

Luo, H., and Paal, S. G. (2019). "A locally weighted machine learning model for generalized prediction of drift capacity in seismic vulnerability assessments." *Computer-Aided Civil and Infrastructure Engineering*, 34(11), 935–950.

Ma, Y., and Gong, J.-X. (2018). "Probability Identification of Seismic Failure Modes of Reinforced Concrete Columns based on Experimental Observations." *Journal of Earthquake Engineering*, 22(10), 1881–1899.

Mackie, K. R., and Stojadinović, B. (2005). *Fragility basis for California highway overpass bridge seismic decision making*. Pacific Earthquake Engineering Research Center, College of Engineering ….

Mander, J. B., Priestley, M. J. N., and Park, R. (1988). "Theoretical Stress-Strain Model for Confined Concrete." *Journal of Structural Engineering*, 114(8), 1804–1826.

Mangalathu, S., and Burton, H. V. (2019). "Deep learning-based classification of earthquake-impacted buildings using textual damage descriptions." *International Journal of Disaster Risk Reduction*, 36, 101111.

Mangalathu, S., Hwang, S.-H., Choi, E., and Jeon, J.-S. (2019a). "Rapid seismic damage evaluation of bridge portfolios using machine learning techniques." *Engineering Structures*, 201, 109785.

Mangalathu, S., Jang, H., Hwang, S.-H., and Jeon, J.-S. (2020). "Data-driven machine-learning-based seismic failure mode identification of reinforced concrete shear walls." *Engineering Structures*, 208, 110331.

Mangalathu, S., and Jeon, J.-S. (2018). "Classification of failure mode and prediction of shear strength for reinforced concrete beam-column joints using machine learning techniques." *Engineering Structures*, 160, 85–94.

Mangalathu, S., and Jeon, J.-S. (2019). "Machine Learning–Based Failure Mode Recognition of Circular Reinforced Concrete Bridge Columns: Comparative Study." *Journal of Structural Engineering*, 145(10), 04019104.

Mangalathu, S., Jeon, J.-S., and DesRoches, R. (2018). "Critical uncertainty parameters influencing seismic performance of bridges using Lasso regression." *Earthquake Engineering & Structural Dynamics*, 47(3), 784–801.

Mangalathu, S., Shokrabadi, M., and Burton, H. (2019b). *Aftershock Seismic Vulnerability and Time-Dependent Risk Assessment of Bridges*. PEER Report No. 2019/04.

Marsh, M. L., Stringer, S. J., National Cooperative Highway Research Program Synthesis Program, Transportation Research Board, and National Academies of Sciences, Engineering, and Medicine. (2013). *Performance-Based Seismic Bridge Design*. Transportation Research Board, Washington, D.C., 22632.

Mazzoni, S., McKenna, F., Scott, M., and Fenves, G. L. (2006). "OpenSees Command Language Manual."

McCabe, S. L., and Hall, W. J. (1989). "Assessment of Seismic Structural Damage." *Journal of Structural Engineering*, 115(9), 2166–2183.

Menegotto, M., and Pinto, P. E. (1973). "Method of analysis for cyclically loaded RC plane frames including changes in geometry and non-elastic behavior of elements under combined normal force and bending." *Proc. of IABSE symposium on resistance and ultimate deformability of structures acted on by well defined repeated loads*, 15–22.

Moehle, J. (1995). "Northridge earthquake of January 17, 1994: reconnaissance report, volume 1—highway bridges and traffic management." *Earthquake Spectra*, 11(3), 287–372.

Murphy, T. P., Marsh, L., Bennion, S., Buckle, I. G., Luco, N., Anderson, D., Kowalsky, M., and Restrepo, J. (2020). *Proposed AASHTO Guidelines for Performance-Based Seismic Bridge Design*.

National Research Council of Canada. (2014). *Canadian Highway Bridge Design Code S6-14*. National Research Council of Canada.

National Research Council of Canada. (2019). *Canadian Highway Bridge Design Code S6-19*. National Research Council of Canada.

Nielson, B. G. (2005). "Analytical Fragility Curves for Highway Bridges in Moderate Seismic Zones." Georgia Institute of Technology.

Nielson, B. G., and DesRoches, R. (2007a). "Seismic fragility methodology for highway bridges using a component level approach." *Earthquake Engineering & Structural Dynamics*, 36(6), 823–839.

Nielson, B. G., and DesRoches, R. (2007b). "Analytical Seismic Fragility Curves for Typical Bridges in the Central and Southeastern United States." *Earthquake Spectra*, SAGE Publications Ltd STM, 23(3), 615–633.

Ohtaki, T., Benzoni, G., Priestley, M. J. N., and Seible, F. (1997). "SEISMIC PERFORMANCE OF A FULL SCALE BRIDGE COLUMN - AS BUILT AND AS REPAIRED."

Omori, F. (1894). "On the Aftershocks of Earthquakes." *Journal of the College of Science*, Imperial University of Tokyo, (7), 111–120.

Omranian, E., Abdelnaby, A., Abdollahzadeh, G., Rostamian, M., and Hosseinpour, F. (2018a). "Fragility Curve Development for the Seismic Vulnerability Assessment of Retrofitted RC Bridges under Mainshock-Aftershock Seismic Sequences." *Structures Congress 2018*, American Society of Civil Engineers, Fort Worth, Texas, 308–316.

Omranian, E., Abdelnaby, A. E., and Abdollahzadeh, G. (2018b). "Seismic vulnerability assessment of RC skew bridges subjected to mainshock-aftershock sequences." *Soil Dynamics and Earthquake Engineering*, 114, 186–197.

Padgett, J. E., and DesRoches, R. (2009). "Retrofitted Bridge Fragility Analysis for Typical Classes of Multispan Bridges." *Earthquake Spectra*, SAGE Publications Ltd STM, 25(1), 117–141.

Padgett, J. E., Nielson, B. G., and DesRoches, R. (2008). "Selection of optimal intensity measures in probabilistic seismic demand models of highway bridge portfolios." *Earthquake Engineering & Structural Dynamics*, 37(5), 711–725.

Pang, Y., Dang, X., and Yuan, W. (2014). "An Artificial Neural Network Based Method for Seismic Fragility Analysis of Highway Bridges." *Advances in Structural Engineering*, 17(3), 413–428.

Pang, Y., and Wu, L. (2018). "Seismic Fragility Analysis of Multispan Reinforced Concrete Bridges Using Mainshock-Aftershock Sequences." *Mathematical Problems in Engineering*, 2018, 1–12.

Park, Y., and Ang, A. H. -S. (1985). "Mechanistic Seismic Damage Model for Reinforced Concrete." *Journal of Structural Engineering*, 111(4), 722–739.

Paulay, T., and Priestley, M. J. N. (1992). *Seismic design of reinforced concrete and masonry buildings*. Wiley, New York.

Priestley, M. N., Seible, F., and Calvi, G. M. (1996). *Seismic design and retrofit of bridges*. John Wiley & Sons.

Ramanathan, K., Padgett, J. E., and DesRoches, R. (2015). "Temporal evolution of seismic fragility curves for concrete box-girder bridges in California." *Engineering Structures*, 97, 29–46.

Sarle, W. S. (1994). "Neural Networks and Statistical Models." *Nineteenth Annual SAS Users Group International Conference*, Cary, NC, USA, 13.

Scott, M. H. (2011). "Numerical Integration Options for the Force-Based Beam-Column Element in OpenSees." 7.

Scott, M. H., and Fenves, G. L. (2006). "Plastic Hinge Integration Methods for Force-Based Beam–Column Elements." *Journal of Structural Engineering*, 132(2), 244–252.

Shekhar, S., and Ghosh, J. (2020). "A metamodeling based seismic life-cycle cost assessment framework for highway bridge structures." *Reliability Engineering & System Safety*, 195, 106724.

Shin, M., and Kim, B. (2017). "Effects of frequency contents of aftershock ground motions on reinforced concrete (RC) bridge columns." *Soil Dynamics and Earthquake Engineering*, 97, 48–59.

Terzic, V., and Stojadinovic, B. (2010). *Post-Earthquake Traffic Capacity of Modern Bridges in California*. PEER 2010/103, 218.

Tesfamariam, S., and Goda, K. (2015). "Loss estimation for non-ductile reinforced concrete building in Victoria, British Columbia, Canada: effects of mega-thrust Mw9-class subduction earthquakes and aftershocks." *Earthquake Engineering & Structural Dynamics*, 44(13), 2303–2320.

Tesfamariam, S., and Goda, K. (2017). "Energy-Based Seismic Risk Evaluation of Tall Reinforced Concrete Building in Vancouver, BC, Canada, under Mw9 Megathrust Subduction Earthquakes and Aftershocks." *Frontiers in Built Environment*, 3, 29.

Tesfamariam, S., Goda, K., and Mondal, G. (2015). "Seismic Vulnerability of Reinforced Concrete Frame with Unreinforced Masonry Infill Due to Main Shock–Aftershock Earthquake Sequences." *Earthquake Spectra*, SAGE Publications Ltd STM, 31(3), 1427–1449.

Todorov, B., and Billah, A. H. M. M. (2020). "Mainshock-aftershock damage assessment of concrete bridge reinforced with shape memory alloy rebar." Sendai, Japan.

Todorov, B., and Billah, A. H. M. M. (2021). "Seismic fragility and damage assessment of reinforced concrete bridge pier under long-duration, near-fault, and far-field ground motions." *Structures*, 31, 671–685.

Veletzos, M., Panagiutou, M., Restrepo, J., and Sahs, S. (2008). *Visual Inspection & Capacity Assessment of Earthquake Damaged Reinforced Concrete Bridge Elements*. Caltrans Division of Research & Inovation, 392.

Xie, X., Lin, G., Duan, Y., Zhao, J. L., and Wang, R. (2012). "Seismic damage of long span steel tower suspension bridge considering strong aftershocks." *Earthquakes and Structures*, 3.

Xie, Y., and DesRoches, R. (2019). "Sensitivity of seismic demands and fragility estimates of a typical California highway bridge to uncertainties in its soil-structure interaction modeling." *Engineering Structures*, 189, 605–617.

Xie, Y., Ebad Sichani, M., Padgett, J. E., and DesRoches, R. (2020). "The promise of implementing machine learning in earthquake engineering: A state-of-the-art review." *Earthquake Spectra*, 875529302091941.

Yeo, G. L., and Cornell, C. A. (2005). *Stochastic characterization and decision bases under time-dependent aftershock risk in performance-based earthquake engineering*. Pacific Earthquake Engineering Research Center Berkeley, CA.

Youm, K.-S., Lee, H.-E., and Choi, S. (2006). "Seismic performance of repaired RC columns." *Magazine of Concrete Research*, ICE Publishing, 58(5), 267–276.

Zhang, J., and Huo, Y. (2009). "Evaluating effectiveness and optimum design of isolation devices for highway bridges using the fragility function method." *Engineering Structures*, 31(8), 1648–1660.